NOVEL ELECTROLYTES AND SYSTEM DESIGNS FOR THERMO-ELECTROCHEMICAL CELLS

A Dissertation
Presented to
The Academic Faculty

By

Ali Hussain Kazim

In Partial Fulfillment
of the Requirements for the Degree
Doctor of Philosophy in the
George W. Woodruff School of Mechanical Engineering

Georgia Institute of Technology

August 2017

NOVEL ELECTROLYTES AND SYSTEM DESIGNS FOR THERMO-ELECTROCHEMICAL CELLS

Approved by:

Dr. Baratunde A. Cola, Advisor
George W. Woodruff School of Mechanical Engineering
Georgia Institute of Technology

Dr. Sheldon M. Jeter
George W. Woodruff School of Mechanical Engineering
Georgia Institute of Technology

Dr. Peter J. Hesketh
George W. Woodruff School of Mechanical Engineering
Georgia Institute of Technology

Dr. Marta Hatzell
George W. Woodruff School of Mechanical Engineering
Georgia Institute of Technology

Dr. Gleb Yushin
School of Materials Science and Engineering
Georgia Institute of Technology

Date Approved: June 15, 2017

That man can have nothing but what he strives for; that (the fruit of) his striving will soon come in sight: Then will he be rewarded with a reward complete.

Quran, chapter no. 53, verse no. 39-41

To my wife Aqsa

ACKNOWLEDGEMENTS

First and foremost, I want to thank Allah Almighty for surrounding me with amazing people, taking me to different places and giving me the opportunity of coming and studying at Georgia Tech. I want to thank Georgia Tech for being a school buzzing with energy, inspiring one to dream and equipping one with the skills to make those dreams a reality. During my stay here, I have breath in this energy, as I daily came to Tech through the Atlantic drive. Looking up in the direction of Marcus building offered a wide expanse view of the sky and made me imagine the limitless opportunities the world has to offer while looking down on the ground and the short distance of the walk also made me realize my constraints.

Next I want to thank my PhD advisor Dr. Baratunde Cola for being an inspiration towards my research and instilling in me that every blow is an opportunity to move forward. I would like to express my appreciation for Dr. Ray Baughman for showcasing that learning is a lifelong process and that one should always remain curious.

I want to sincerely thank Dr. Sheldon Jeter for sharing his immense knowledge and providing didactic guidance. My special thanks go to Dr. Marta Haztell for broadening my view in tackling problems. I would like to express my appreciation for Dr. Peter Hesketh and Dr. Gleb Yushin for serving on my committee and providing thought provoking discussions.

Next I would like to thank my lab mates in the NEST lab: Dr. Thomas Bougher and Dr. Mathew Smith were always available to provide guidance for my everyday queries regarding work. My humblest gratitude goes out to Dr. Pablo Salazar for providing guidance to get me started in research. I want to thank Daron Spence for always selflessly responding to calls for help and finally Eric Trevo, Zhe Cheng and Erik Anderson for the random chats throughout the day.

A very special shout out goes to people that I have worked with on different projects.

Long Zhang, Na Li, Carter Haines and Anh Tran, I owe them a depth of gratitude for teaching me many things about research. I would also like to thank undergraduates Sai T. Stephens and A. Sina Booeshaghi for bringing tremendous amount of energy to projects.

A journey is only enjoyable if you have friends to accompany and I was fortunate to make many life long friends. A special mention here goes to Thomas Sherer, Hamid Reza Seyf, Srinivas Kumar, Syed Bilal Khalid, Muhammad Ali Antho, Talal Hassan Siddiqui, E.J. Hatfalvi, Trevor Augustin, Bailey Zhao, Hussain Zaheer and lastly Irfan Abid. Thank you Irfan *Bhai*, for making fitness a habit.

I want to take this opportunity to deeply thank my teachers, colleagues and students at my alma mater University of Engineering and Technology, Lahore (UET Lahore). My time at UET Lahore, both as a student and then as a faculty member has contributed to my growth and development in innumerable ways. Lastly, I wish to acknowledge the Fulbright program for their support in realizing the PhD dream.

Moving to the foundation of my life, my parents: Nasreen Naz Sajid and Sajid Hussain. Thank you *Ami* and *Abu* for always believing in me and telling me to be myself. Your devotion towards my upbringing and constant prayers, is something I deeply value. To my brothers, Dr. Awais Hussain Kazim and Ahmed Hussain Kazim, your achievements excite me to do better in my life. Now to the parents of my wife, Dr. Shahnaz Cheema and Dr. Shabbir Ahmed, *Mama* and *Papa*, thank you for entrusting me with your most precious thing: your daughter. Over the years you have become an integral part of my life and the amount of support you have provided me is unparalleled.

Moving to the most special part of my life: my daughter, Fatima Ali, who is the pride of my life and my son, Mustafa Ali, who is the joy of my life. Thank you for making my life truly meaningful. Finally moving to strength of my life, my wife, Dr. Aqsa Shabbir, you are a constant reminder why I am alive. Thank you for filling my life with happiness!

TABLE OF CONTENTS

LIST OF TABLES

LIST OF FIGURES

LIST OF SYMBOLS

A	electrode surface area
C_{dl}	double-layer capacitance
C_o	concentration of oxidized species
C_r	concentration of reduced species
ρ	electrolyte density
E	electrode potential
$E_{1/2}$	half-wave potential
E_{pa}	anodic peak
E_{pc}	cathodic peak
F	Faraday constant
h	heat transfer coefficient
$\bar{h}$	average heat transfer coefficient
I	current
j	current density per unit area
j_{sc}	short circuit current density per unit area
k^o	electrochemical rate constant
k	thermal conductivity of electrolyte
n	number of electrons
Nu	Nusselt number
$\bar{Nu}$	average Nusselt number
η	conversion efficiency
η_r	relative Carnot efficiency
P_{max}	maximum electric power
Q_{conv}	heat transfer due to convection
Q_{in}	applied heat transfer

R	gas constant
R_s	solution resistance
R_{ct}	charge transfer resistance
S_e	Seebeck coefficient
T	Temperature
T_a	Anode temperature
T_C	Cathode temperature
T_H	Temperature of the hot electrode
T^o	standard temperature
υ	kinematic viscosity
V_{oc}	Open circuit voltage
$v(x)$	velocity in the x-direction
W	Warburg impedance
ZT	figure of merit
ΔT	change in temperature
ΔS	change in entropy
$\frac{\partial \phi(x)}{\partial x}$	gradient of electric potential
$\frac{\partial C_i(x)}{\partial x}$	gradient of chemical potential
σ	ohmic conductivity

LIST OF ABBREVIATIONS

BCNTs	boron doped carbon nanotubes
CNTs	carbon nanotubes
CVD	chemical vapor deposition
CV	cyclic voltammetry
CuHCF	copper hexacyanoferrate
CAD	computer aided design
EIS	electrochemical impedance spectroscopy
EAS	electroactive surface area
EMF	electromotive force
EPD	electrophoretic deposition
GO	graphene oxide
MWNT	multi-walled carbon nanotubes
NCNT	nitrogen doped carbon nanotubes
PEDOT	poly(3,4-ethylenedioxythiophene)
PET	polyethylene terephthalate
PSS	poly(styrenesulfonate)
rGO	reduced graphene oxide
TEC	thermo-electrochemical cell
sTEC	thermo-electrochemical cell with stationary electrolyte
SWNT	single-walled nanotubes
fTEC	thermo-electrochemical cell with flowing electrolyte
EMI	1-ethyl-3 methlyimidazolium
TFSI	N,N-bis (trifluoromethane) sulphonamide

SUMMARY

Low-grade waste heat is ubiquitous and a byproduct of all energy conversion mechanisms. Thermo-electrochemical cells (thermocells) directly convert temperature difference to electromotive force with no moving parts. It is an inexpensive technology to harvest waste heat. However, low power conversion efficiency due to ohmic, interfacial charge transfer and mass transfer resistances has limited its use in commercial applications. This work explores improving electrochemical properties of the standard electrolyte and implementation of thermocells in applications providing liquid cooling.

In the initial part of this dissertation, poly (3,4- ethylenedioxythiophene) poly (styrenesulfonate) was used to form a composite having percolated networks of dispersed carbon nanotubes. The composite was dispersed in the standard electrolyte of thermocells aqueous potassium ferri/ferrocyanide and the mixture was characterized using electrochemical impedance spectroscopy. Analysis of the impedance spectra showed a 10 % increase in ohmic conductivity and about a 5-fold decrease in interfacial charge transfer resistance in the composite electrolyte, which is caused by addition of the charge carriers, interfacial polarization and improved contact at the electrode/electrolyte interface. The enhancement of properties in the composite electrolyte increases the power of a thermo-electrochemical cell by about 30 %. In addition, thermal characterization using transient plane source technique showed that the thermal conductivity decreased by about 5 % for the new composite electrolyte, leading to ZT enhancement by about 15 %.

Thermocells low efficiencies, restrict there use as a standalone energy harvesting device. To this end, flow thermo-electrochemical cell (fTEC) has been invented, fabricated and implemented specifically for data centers and it can be extended to wherever liquid cooling heat sinks are employed. The current sole purpose of heat sinks is to provide cooling, fTEC enable supplementing the existing purpose with energy harvesting and temperature monitoring for entire liquid flow line. Initial unoptimized design in term of electrode

material and configuration produced power density of 0.05 W/m^2 and provided heat transfer coefficient of 450 W/m^2 K. Carbon nanotube buckypaper electrodes are used to improve the performance of fTEC. The use of carbon nanotube buckypaper electrode provided a larger surface area and faster kinetics for redox reaction. Optimization of the electrode material and configuration, improved the power density of fTEC to 0.36 W/m^2.

The original contribution of this work are three fold. Firstly, composite of poly (3,4-ethylenedioxythiophene) poly (styrenesulfonate) and carbon nanotube was developed that improved the interfacial charge transfer resistance, ohmic conductivity and thermal conductivity of the benchmark electrolyte used for thermocells. Secondly, thermocell having flowing electrolyte was identified, fabricated and implemented. The fTEC provides cooling, energy harvesting and temperature monitoring for liquid cooling applications. Thirdly, the design of the fTEC is improved by taking advantage of the higher temperature available and using electrodes providing larger surface area and faster charge transfer kinetics.

CHAPTER 1

INTRODUCTION

1.1 Energy crisis

While the utilization of energy is a basic building block of growing world economies, the challenges to provide for the increasing demand are ominous and a shortage of supply may end up being a major road block. The primary concern of the major contributors of energy i.e. fossil fuels is that there is finite supply which necessitates efficient utilization and a look for alternative sources of energy. Current total primary energy supply is dominated by fossil fuels as shown in Figure 1.1. The renewables comprising of hydro, others (geothermal, solar, wind etc.), biofuels and waste, comprise meager 14.1 % of total world's energy supply.

While the reliance on fossil fuels is overwhelming, the estimated reserves are fast diminishing: oil (50.7 years), natural gas (52.8 years) and coal (114 years) [2].

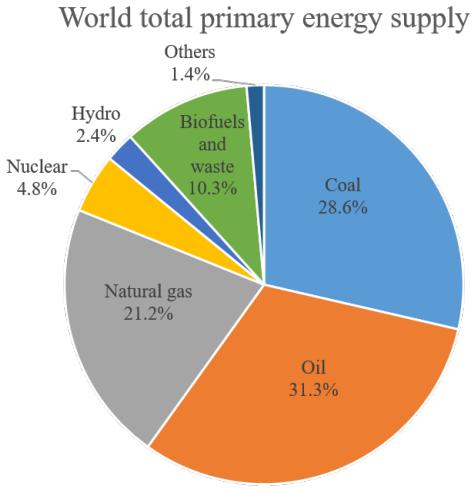

Figure 1.1: World's total primary energy supply mix for 2014. The total supply is 13699 million tonnes of oil equivalent [1].

The other aspect of fossil fuel consumption is the detrimental environmental impact of fossil fuel emissions. Emission of carbon dioxide and methane are largely attributed to cause global warming and climate change. Increased scientific understanding about global warming, has made as many as 95 % of scientists agree that global warming is due to human activities and mainly due to the emission of green house gases methane and carbon dioxide [3, 4, 5, 6]. The current high concentration of carbon dioxide has not been seen previously in thousands of years. The problem is that carbon dioxide released does not decompose and stays in the ecosystem. Half of it is absorbed by the vegetation and oceans, while the other half stays in the atmosphere [7]. Primary proof of global warming are the rising temperatures of land and ocean. NASA's Goddard Institute for Space Studies (GISS) has been maintaining estimate of the global surface temperate change known as GISS surface temperature analysis (GISTEMP)(Figure 1.2) [8, 9, 10]. In the graph, global mean estimates based on land and ocean data temperature is touching 0.86 ^{o}C above pre-industrial level. Locally Weighted Scatterplot Smoothing (Lowess smoothing) is a regression technique that creates a smooth line to help see the relationship between the variable and foresee trends.

At the 21st Conference of the Parties of the United Nations Framework Convention on Climate Change (UNFCCC) in Paris an agreement was made between 195 countries to keep global average temperature below 2 ^{o}C above preindustrial level and to pursue efforts to limit the temperature increase at 1.5 ^{o}C above preindustrial level [11]. This landmark agreement serves to curtail the harmful impact on climate system. However, meeting this goal of keeping global average temperature below 2 ^{o}C requires immediate significant and sustained global action, with probable reliance on net negative emission in the longer term [12]. This is because a delay in starting mitigation measures will lead to a requirement of higher mitigation needed [13], higher costs [14, 15] and the target to remain below 2 ^{o}C may become unfeasible [16, 17]. This is where well targeted technological innovations can play a part in sustaining mitigation efforts for a longer period of time [18]. One such

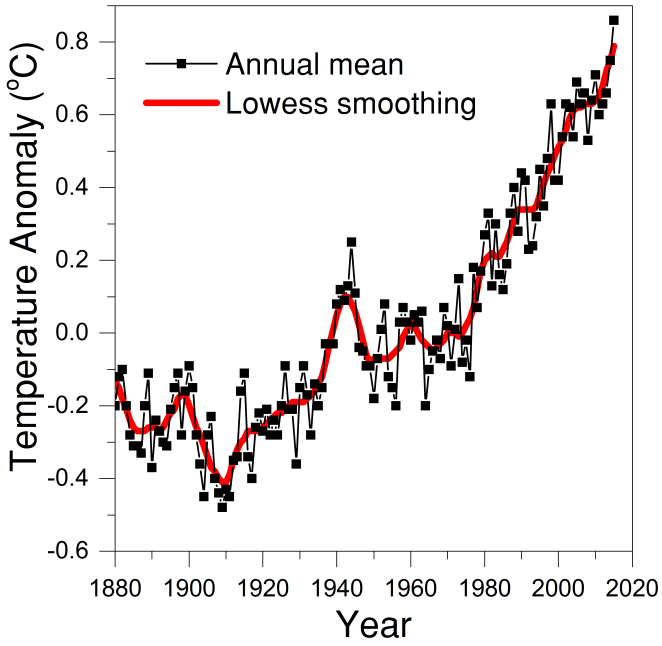

Figure 1.2: Global mean estimate on land and ocean data from 1880 to present. The solid black line is the global annual mean and the solid red line is the 5-year lowess smooth [8, 9, 10].

method is to harvest waste heat. Waste heat is ubiquitous. It is a byproduct from all energy conversion mechanisms from combustion of food in our bodies [19] to combustion fuels in vehicles, industries etc. As waste heat is so prevalent, efforts to convert it in useful energy would not only improve the efficiency of current technologies but will also help in decreasing the reliance on fossil fuel consumption.

1.2 Waste heat recovery

Generating power from waste heat sources depends upon thermodynamic constraints imposed by different temperatures available. Efficiency of the technology largely depends on the temperature of heat source. Waste heat can be classified by the temperature of heat source by dividing temperature range into low-,medium- and high-quality of waste heat source as follows [20]:

High: 650^{o}C [1200 ^{o}F] and higher

Medium: 232^{o}C [450 ^{o}F] to 650^{o}C [1200 ^{o}F]

Low: 232^{o}C [450 ^{o}F] and lower[1].

Generally the power generation from waste heat has been limited to using high and medium temperature heat, via mechanical energy. It typically involves waste heat warming a working fluid which in turn drives the turbine. The name of the working fluid differentiates what the conversion technology is called. In case of Rankine cycle the fluid is water, in case of Organic cycle can be toluene, silicon oil, propane to name a few of many options available and in case of Kalina cycle the fluid is a mixture of ammonia and water. These traditional methods have been well-developed and are being used at the industrial level to convert heat to mechanical work which is then converted to electrical energy. Currently new technologies are being explored to directly convert thermal energy to electrical energy. Theses include thermo photo voltaic, thermionic, thermoelectric and thermo-electrochemical generators.

Thermo photo voltaic (TPV) generators operate in the high temperature range 800-1000 ^{o}C [22]. It consists of a heat source, emitter, radiation filter and photo voltaic (PV) cell. Heat source heats the emitter, which in turn emits radiation. The PV cell converts the radiation to electrical energy. The filter passes the radiation that matches the PV cell, while reflecting remaining back to emitter.

Thermionic generator hot cathode is heated which generates an electron which passes in vacuum to low work function anode [23]. The electron generated passes through the external circuit. This technology is similar to TPV and requires a high temperature of 800 ^{o}C [24].

[1]Other sources [21] have slightly different temperature ranges, High: 1100 to 3000 ^{o}F, Medium: 400 to 1100 ^{o}F, Low: 80 to 400 ^{o}F

1.2.1 Thermoelectrics

Thermoeletrics operate on the principle of Seebeck effect i.e. direct conversion of temperature to voltage. It consists of two doped semi-conducting material, one n-type (containing free electrons) and the other p-type (containing free holes). When a temperature difference is applied, the mobile charge carriers tend to diffuse towards the cold end and the build up of charge at one end produces electrostatic potential. The performance of thermoelectric is characterized by a figure of merit ZT,

$$ZT = \frac{\sigma S^2 T}{\lambda} \tag{1.1}$$

were σ is the ohmic conductivity, S is the Seebeck coefficient, T is the temperature and λ is the thermal conductivity. High ZT value of 2.4, has been reported for near room temperature [25]. Thermoelectrics have found application in deep space mission such as Voyager [26]. Deep space provides the ideal environment to operate thermoelectrics as the ambient temperature being close to 2 K provides the ideal temperature for cold side, while the radioisotope provides heating to the hot side [27, 28].

1.2.2 Thermo-electrochemical cells

Thermo-electrochemical cells (or thermocells) similar to thermoelectrics operate on Seebeck effect. However, unlike the solid state, thermoelectrics have ions present in liquid state as charge carriers inside a thermocells. When a temperature difference is applied at the electrodes, reduction and oxidation takes place at the respective electrodes. The electron lost as a result of oxidation passes through the external circuit. ZT can be used to describe the performance of thermocells, with typical values a two order of magnitude lower than a thermoelectrics. In terms of properties, thermocells have a much higher S, but suffer from very low ohmic conductivities. From the commercialization standpoint, thermocells are very economical, as the materials used for their preparation is readily available.

1.3 Objective and Overview

The dissertation work focuses on addressing the challenges faced by thermocells both at the fundamental and applied level. At the fundamental level, the properties ohmic conductivity, interfacial charge transfer resistance and thermal conductivity have been improved for the benchmark electrolyte use for thermocells. While at the applied level, flow thermoelectrochemical cell (fTEC) has been invented, which supplements an existing functions of applications providing liquid cooling with energy harvesting and temperature monitoring.

This thesis is structured as follows:

In this chapter motivation for developing technologies that harvest waste heat is presented with emphasis on energy crisis and detrimental impact of fossil fuels. Motivation is followed by a description of various waste heat technologies, highlighting there working principles and operating temperature.

In chapter 2, literature review of thermocells is presented. The chapter starts with describing the driving principle the Seebeck coefficient from its origin as an observation first made on solid state devices to it branching out to aqueous liquids to relative more recent application in ionic liquids. This is followed by overview of the two main parts of thermocells the electrodes and the electrolytes. One of the major bottlenecks for the improved the thermocells is there low ohmic conductivity, the governing equation in the bulk electrolyte and at the electrode/electrolyte interface are described. It is followed by studies on modeling of thermocells. The coupling of the aforementioned variables are described in the working of thermocells. The chapter concludes with the application of thermocells and technologies which are variants of thermocells having the same operating principle.

In chapter 3, the effect of mixing carbon nanotubes and poly (3,4-ethylenedioxythiophene) poly(styrenesulfonate) in aqueous potassium ferri/ferrocyanide electrolyte is characterized using electrochemical impedance spectroscopy. Analysis of the impedance spectra shows a 10 % increase in ohmic conductivity and about 5-fold decrease in interfacial charge trans-

fer resistance in the composite electrolyte, which is caused by addition of charge carriers, interfacial polarization and improved contact at the electrode/electrolyte interface. The enhancement of properties in the composite electrolyte increases the power of a thermo-electrochemical cell by about 30 %.

In chapter 4, the mixture of maximum ohmic conductivity on the previous chapter are selected and there corresponding thermal conductivity is measured. It is observed and inverse favorable trend exist between the ohmic conductivity and thermal conductivities, results in ZT enhancement of about 15 %. In addition molecular dynamic simulation (MD) is carried out to investigate change in ohmic conductivity when concentration changes from 0.1 M to 0.4 M. The MD work lays a foundation for exploring other properties of the electrolyte like Seebeck coefficient, thermal conductivity, viscosity etc.

In chapter 5, proof of concept of flow thermo-electrochemical generator is implemented. Flow thermo-electrochemical generator has been tested and validated a modified liquid cooling design system that supplements current cooling architecture with the ability to harvest energy from waste heat sources. An electrolyte capable of undergoing a reversible redox reaction is pumped through a macro-channel flow thermo-electrochemical generator. The heat energy flow is coupled with electricity generation through the thermoelectic effect allowing cooling and power harvesting to occur in parallel. The current design generated 88 μW of power, achieved a heat transfer coefficient of 450 $W/(m^2.K)$. This technology can be employed in any location where liquid cooling is used, from CPU's in data centers to battery packs in electric vehicles. By providing cooling and energy harvesting these applications will benefit from energy conversion and recycling.

In chapter 6, the performance of flow thermo-electrochemical generator is improved by changing electrode material and their location. In the previous chapter it was identified that one can take advantage of maximum heat flux by having electrodes perpendicular to heat flux. As a consequence of better electrode material and position, power density of the flow thermo-electrochemical cell increased by 7.3 times.

In the end, conclusion and perspective for future work is presented in chapter 7.

Table 1.1: Overview of the dissertation

Topic	Methods	Major Results	Chapter
Dispersing carbon nanotube in polymer, disperse carbon nanotube-polymer suspension in aqueous based redox couple	• Electrochemical Impedance Spectroscopy • Cyclic Voltammetry	• New composite carbon nanotube based aqueous electrolyte	3
Electrical and thermal properties of aqueous based electrolyte	• Electrochemical Impedance Spectroscopy • Transient Plane Source technique	• Inverse relationship observed with incremental additions of PEDOT:PSS and MWNT composite	3,4
Simulation of ohmic conductivity	• Molecular Dynamic Simulation	Trend of ohmic conductivity matched experimental results	4
Flowing electrolyte to recycle waste heat to produce electricity	• Open Circuit Potential-time • Amperometric current-time curve	Flow thermo-electrochemical cell has been invented: • Harvest waste heat ($P_{max} = 0.05\ W/m^2$) • Cool heat dissipating applications in particular data centers ($\bar{h}$= 450 W/m^2K)	5
Optimization of electrode configuration and geometry	• Open Circuit Potential-time • Amperometric current-time curve	• Harvest waste heat ($P_{max} = 0.36\ W/m^2$) with same heat transfer coefficient	6

CHAPTER 2
LITERATURE REVIEW

This chapter will describe thermocells literature from the inception of Seebeck coefficient to its current state. The chapter is divided in sections, starting from principle of operation to evolution of understanding of first principles, electrode, electrolytes, modeling of thermocells, working of thermocells, applications and different type of thermocells.

2.1 Seebeck coefficient

Seebeck coefficient represents direct conversion of heat to electricity when a temperature difference is applied to dissimilar materials coupled together. In 1821, Thomas Johann Seebeck first observed this effect in metals which were joined together. It was found that when a temperature difference is applied, the mobile charge carrier at hot-end diffuse to cold-end carrying heat and charge. The build-up of charge carriers leads to a net charge at cold-end, resulting in an electrostatic potential (voltage). In the mid-20^{th} century, research focus shifted from metals to semiconductors and are subject of intense research [29, 30]. From a material perspective, semiconductors have reached their limit and research has moved on to nanostructuring the existing materials to improve performance [29].

Towards the end of 19^{th} century, liquid electrolytes were explored for thermoelectric effect. Applied temperature difference causes a concentration gradient of ions inside the electrolyte, which is known as the Soret effect. For conducting fluids, Soret effect is coupled with Seebeck effect [31]. Transport of heat in aqueous electrolyte is due to water molecules which carry heat from hot to cold side. The thermal conductivity of water governs the heat transport for thermocells having stationary electrolyte. The influence of applied temperature difference on the EMF generated is known as the Seebeck effect, represented by Seebeck coefficient S_e. S_e is derived by considering the entropy difference of product and

reactant at the electrodes [32][33]. For a hypothetical reaction $R \rightleftharpoons O + ne^-$, then the balance of entropy is given as:

$$nF\Big(\frac{\partial E}{\partial T}\Big) = (S_O + \hat{S}_O) - (S_R + \hat{S}_R) - n\bar{\bar{S}}_e \cong S_O - S_R \tag{2.1}$$

Where ΔS is the standard redox reaction entropy, n is the number of electrons involved in the reaction, F is the Faraday constant, $E(T)$ is equilibrium electrode potential, S_0 and S_R are partial molar entropies of species O and R, $\hat{S}_O$ and $\hat{S}_R$ are Eastman entropies, $\bar{\bar{S}}_e$ is the entropy due to transport of electrons in metals leads. Eastman entropy is due to the interaction of an ion and its hydration shell with the solution. Eastman entropy has found to be insignificant for molten salt thermogalvanics [34]. The entropy due to transport of electrons has also been found to be insignificant (normally about 1 %) and hence neglected [35]. Hence the above equation reduces to:

$$S_e = \frac{\partial E(T)}{\partial T} = \frac{\Delta S}{nF} \tag{2.2}$$

Where E(T) is equilibrium electrode potential, ΔS is the standard redox reaction entropy, n is the number of electrons involved in the reaction and F is the Faraday constant [32, 33]. The ΔS is a key property of thermocells and is dependent on many factors due to complex nature of metal ion complex [36, 37]. The structure of typical transition metal redox couple is such that the transition metal is surrounded with molecules or ions called ligands, this is called reorganization in the inner-shell. On outside boundary of ligands is the interaction present due to ligands and solvent, this is called reorganization in the outer-shell. The nature of central metal is important, as reorganization energy at the addition and loss of electron varies from metal to metal [36]. The nature of ligand interaction with solvent plays a role in determining entropy e.g. aquo ligand form stronger hydrogen bond with aqueous solvent as compared to ammine ligand, resulting in larger entropy [36].

The recent progress of improving Seebeck coefficient can be largely attributed to the

introduction of ionic liquids as electrolyte with redox couple instead of aqueous medium. Ionic liquids are molten salts at low-temperature, composed of ions only. Compared to strong electrostatic forces of attraction (called ionic bonds) present in high temperature salts such as sodium chloride, ionic liquid are characterized by weak interaction between delocalized charges on anion and large cations. This contributes to low tendency to crystallize due to non-symmetry in cation and flexibility in anion [38, 39]. The separation distances between large molecular ions weakens and shields the electrostatic forces between ions.

A typical ionic liquid is shown in the schematic Figure 2.1. It is composed of 1-ethyl-3-methylimidazolium (EMI) cation and an N,N-bis(trifluoromethane)sulphonamide (TFSI) anion. The combination provides electrolyte with an ion conductivity comparable to organic electrolyte and high thermal stability with low vapor pressure to temperature up to $300 \sim 400\ ^oC$. The melting point of the EMIM TFSI ionic liquid is -15 ^oC. Delocalized charge not only weakens electrostatic interaction but it also increases the mobility of ions in liquid state. Lack of symmetry both in anion and cation, reduces the possibility of packing into low-efficient crystals and lowers the melting point further. The enormous variety of N- and P-type cations, along with equally large family of organic and inorganic anions, create multitude of options for making ionic liquids, with the ability of tunning their properties.

In liquid state, ionic liquid usually have high ohmic conductivity, making them suitable for being used as electrolyte. Low flammability and very low vapor pressure make them thermally stable and suitable to be used for high temperature application as compared to aqueous electrolyte. Mixture of electrostatic, hydrophobic and hydrogen-bonding types of interaction enable a number of solvency properties; they can dissolve in water or be completely immiscible in water. Equally well, they can be used as solvents for proteins and for inorganic salts.

For devices needing solid form of electrolyte, soft materials versions of ionic liquid are developed such as poly-ionic liquids and gels, also known ionogels. Another emerging

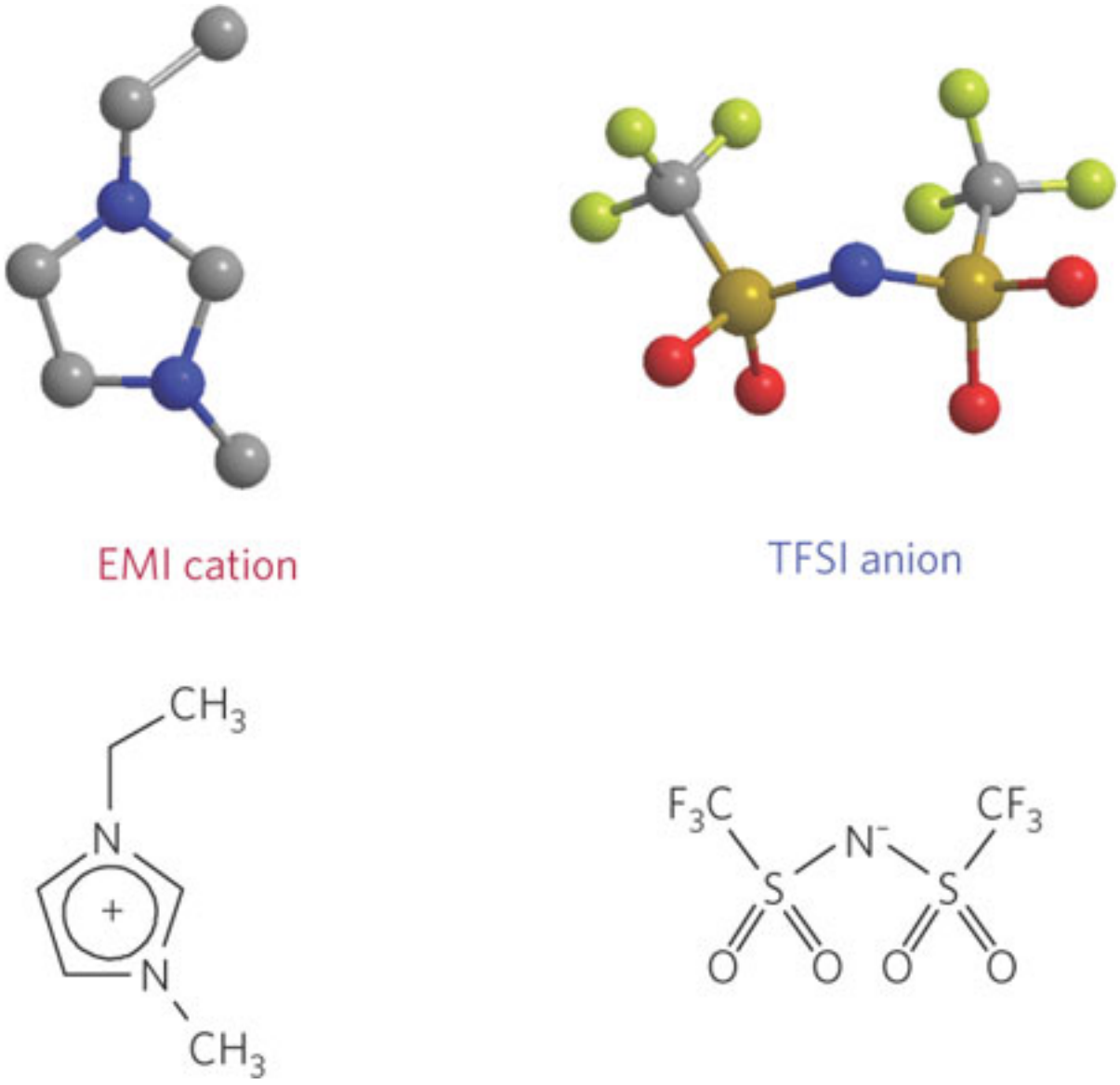

Figure 2.1: Schematic showing the molecular structure of EMI cation and TSFI anion. Reprinted by permission from Macmillan Publishers Ltd: Nature Materials [38], copyright (2009).

alternative to ionogels are organic ionic plastic crystals. For thermocells, the use of liquid state ionic liquids have helped in achieving operating temperatures well above 100 ^oC.

One of the strategies adopted to increase Seebeck coefficient is to introduce an organic solvent in aqueous medium having a redox couple. The addition of organic molecules causes rearrangement in the solvation shell, which increases the entropy change for the redox couple reaction at the electrode. Seebeck coefficient for potassium ferri/ferro cynaide

increased from 1.4 mV/K to 2.9 mV/K when 20 % methanol was added to electrolyte.

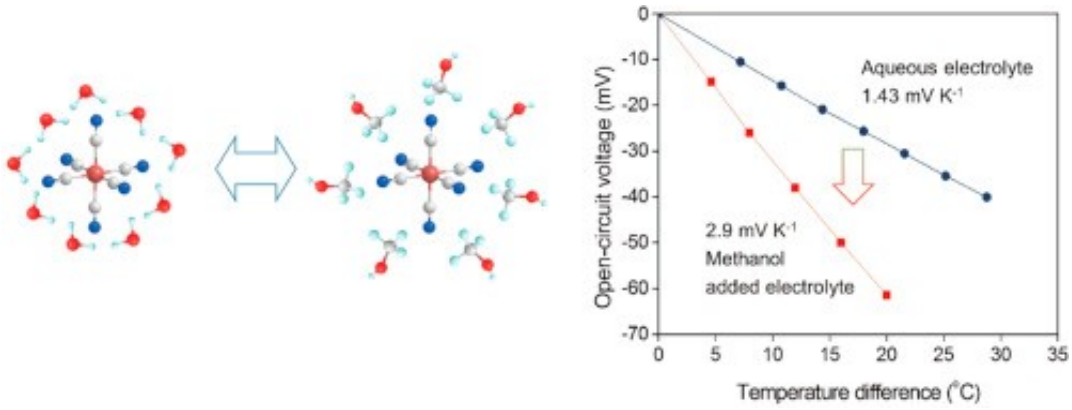

Figure 2.2: Schematic showing change in water molecular arrangement after the introduction of organic solvent and the graph show increase in Seebeck coefficient. Reprinted with permission from [40]. Copyright (2017) Elsevier.

Another method of increasing Seebeck coefficient is to use a α - cyclodextrin supra-molecule to I_3^-/I^- [41]. The supra-molecule captures the triiodide ions on the cold side, which reduces relative concentration of it. As a result, the equilibrium shifts towards oxidation of $3I^-$ to I_3^-. Where as, dissociation of supra-molecule and I_3^- will be promoted on the cold side. As a result of this host-guest interaction Seebeck coefficient is increased from 0.8 mV/K to 2 mV/K. I_3^-/I^- redox couple was also tested in a number of of ionic liquids, such as methoxy- propionitrile, [C_2mpyr][NTf_2], [C_2mim][BF_4],[C_2mim][NTf_2], [C_2mim][$B(CN)_2$], [$P_{4,4,4,6}$][NTf_2], and [$P_{2,2,2,(101)}$][NTf_2] [42]. S_e varied with each ionic liquid, leading to important conclusion that the solvation environment of the redox couple changes reaction entropy.

Very large Seebeck coefficient of 7 mV/K have been reported by Bonetti et al.. [31] The work investigated the use of organic macro ions in non-aqueous solutions. Non-aqueous electrolytes of tetraoctylphosphonium bromide, tetrabutylammonium nitrate and tetradodecylammonium nitrate in ethylene-glycol, 1-dodecanol and 1-octanol were measured for S_e for temperature range of 30 to 45 ^oC. Highest S_e was measured for 0.1 M tetrabutylammonium nitrate in 1-dodecanol. The high S_e value is attributed to structure making effects that tetraalkylammonium ions have on the alcohols.

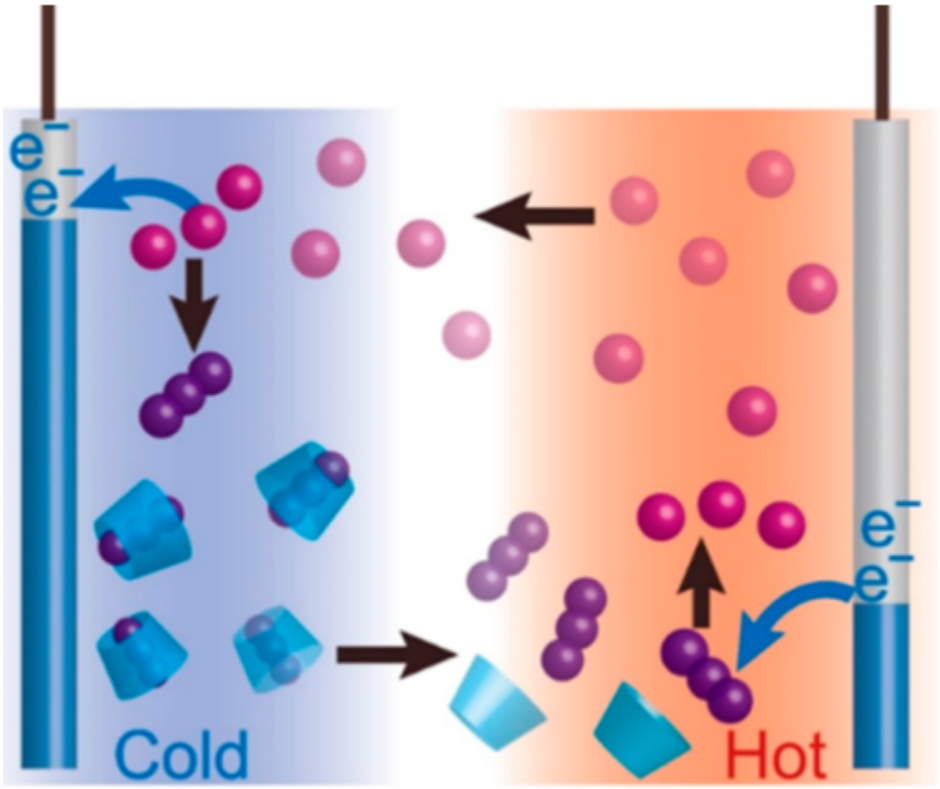

Figure 2.3: Schematic showing thermocell having supra-molecular and I_3^-/I^- redox couple. Reprinted with permission from [41]. Copyright (2016) American Chemical Society.

MWNT have been used to reduce mass transfer resistance and increase thermoelectric power up to 30 % for an ionic liquid [43]. The addition of MWNT causes ion pair dissociation and interfacial polarization [44], both contributing towards reduction in mass transfer resistance.

Inspiration from Lithium ion batteries have lead to Lithium based ionic liquids being used in thermocells, such as lithium bis(trifluoromethylsulfonyl)imide (Li[NTf2]) and tetraglyme have been tested to produce a decent Seebeck coefficient [45]. Similarly, inspiration from ionic liquids used in dye-sensitized solar cells are being tested in thermocells. Thiolate/disulfide redox organic couple in a mixture with 1-ethyl-3-methylimidazolium tetrafluoroborate/acetonitrile to have a conductivity of 3 S/m and Seebeck coefficient of 0.6 mV/K [46].

2.2 Electrodes

Much of the recent advancement in terms of efficiency have been largely due to improvement and development of low-cost electrodes. To obtain a high current, the use of expensive metal such as Platinum was previously required, that is until recently when Hu et al. work of introducing carbon multiwalled nanotube (MWNT) buckypaper electrode reported a high value of 1.4 % for relative Carnot efficiency and also provided an inexpensive substitute [47]. The electrodes provided large surface area and fast reaction kinetics for charge transfer. This innovation not only improved the performance of thermocells but dramatically reduced the cost of making thermocells. This innovation paved the way for two more works of also using carbon nanotube to further improve performance and reported values of 2.63 % [48] and 3.95 % [49] for relative Carnot efficiency. The use of carbon nanotube has helped researchers look beyond cost of thermocells and focus on performance parameters [33, 48, 49, 50, 51, 52, 53], and practical application [54, 55, 56].

They are a number of difference ways, how carbon nanotubes have been employed as electrodes. Electrophoretic deposition (EPD), has been used to deposit MWNT films on stainless steel electrodes. EPD is widely used to deposit CNT-based composites due to ease of manufacturing, possibility of large scale production, low cost, low geometry requirement for substrate etc. [57] It has resulted in power density of 0.82 Wm^{-2} and power conversion efficiency i.e. 50 % higher than Pt electrodes [58]. Typically $Mg(NO_3)_2$ is added to improve adhesion between MWNT films and the substrate [59, 60]. The addition of charge particles can also aid in bringing MWNT to anode and form homogeneous MWNT films [61]. In addition the use Ag particles can increase the thermal and electrical conductivity compared to pristine MWNT electrodes [62, 63]. To include these favorable properties, Qian et al. doped CNTs with Mg^{2+} and Ag through EPD. It resulted increase in power performance from 0.15 to 0.325 W/m^2 [64]. Another method used a single walled nanotube colloidal solution and a highly porous carbon cloth was dipped inside it. Due to high porosity of the

carbon cloth, it swelled with large amount of single walled nanotube [65]. Increasing the number of coats of single walled nanotube to four increased the power output from 0.77 to 0.9 $\mu W cm^{-2}$.

To maximize power a tubing-shaped CNT sheet electrodes have been used [66]. Dry-state spinning process, as shown in Figure 2.4. The performance of CNT sheet electrodes was compared to bare Pt wire. The power performance increased from 8.5 to 15.6 μW. The highly porous sheets provided more reaction sites for the redox couple and hence increase the power.

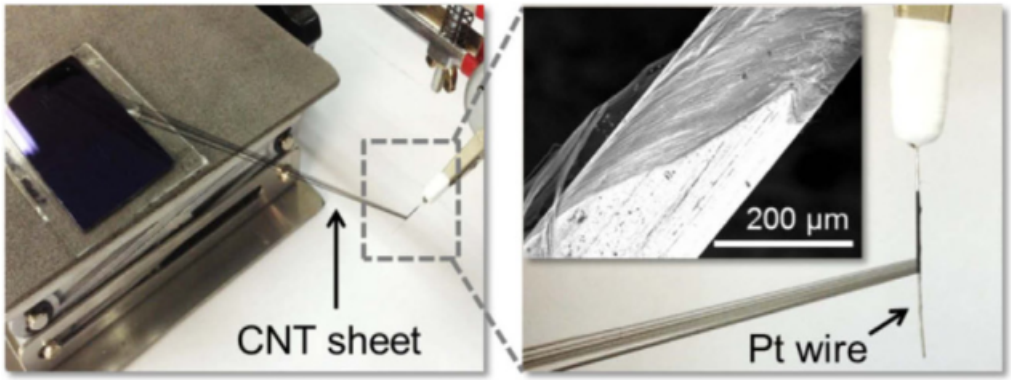

Figure 2.4: Dry-state spinning process to form CNT sheet electrodes. Reprinted with permission from [66]. Copyright (2015) Elsevier.

The present highest relative Carnot efficiency of 2.63 % has been achieved by optimization of electrode composition and thickness of single walled nanotube and reduce graphene oxide (RGO) as electrodes [50]. The optimization is done to balance out porosity and tortuosity, to maximize electrolyte diffusion and enable more access to electroactive surface for electrolyte/electrode interaction. The schematic Figure 2.5 shows stacked configuration of electrodes [48]. A comprehensive study by Kang et al. [51] studied the affects of thermocell performance on various parameters, such as electrode size, cell orientation,electrolyte concentration, electrode spacing and temperature. The work also included the use of SWNT, MWNT, RGO and SWNT/RGO composite as electrodes. SWNT was reported with highest power density of 6.8 W/kg for a temperature difference of 20 ^oC temperature difference

and RGO was reported to have lowest power density of 3.9 W/kg.

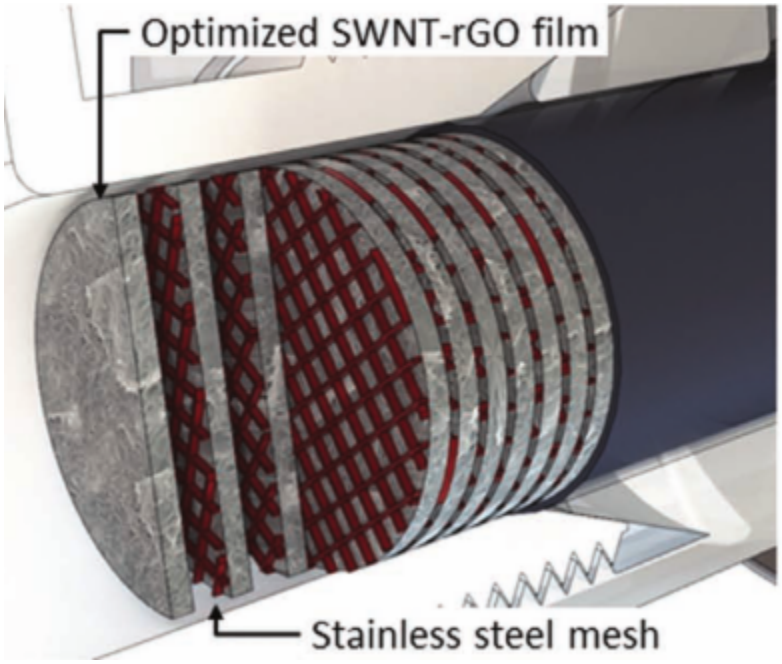

Figure 2.5: Schematic of stacked electrode configuration of SWNT and rGO composite electrode. Reprinted with permission from [50]. Copyright (2013) John Wiley and Sons.

Doping of CNT buckypaper electrodes by boron and nitrogen has also been carried out to increase thermocell power [67]. The doping improved catalytic activity by 3- to 4-fold as compared to pristine CNT buckypaper. Among other alternative to Pt, platinized stainless steel and poly(3,4-ethylenedioxythiophene) deposited on stainless steel have been used to produce approximately the same power as Pt [68].

2.3 Ohmic conductivity

Ohmic conductivity is defined as the reciprocal of the ohmic resistance encountered by ions to diffuse from one electrode to another. The transport of ions, within the fluid medium of thermocell, is due to electrical or chemical potential between the two electrodes or bulk movement of solution with the respective modes are called migration, diffusion and convection. Following is brief description of different modes:

- Migration: Movement of ions due to the influence of electric field (shown by gradient

of electric potential $\frac{\partial \phi(x)}{\partial x}$)

- Diffusion: Movement of ions due to the influence of chemical potential (shown by gradient of chemical potential $\frac{\partial C_i(x)}{\partial x}$)
- Convection: Normally the fluid flow is due to natural and forced convection (shown by $v(x)$). It may be characterized by laminar, turbulent or may have stagnant regions.

This transport of ions is governed by Nernst-Planck equation [69], which shows the cumulative effect of the various modes of charge transfer. The 1-D Nernst-Planck equation for ions transport is given as follows:

$$J_i(x) = -D_i \frac{\partial C_i(x)}{\partial x} - \frac{z_i F}{RT} D_i C_i \frac{\partial \phi(x)}{\partial x} + C_i v(x) \tag{2.3}$$

where $J_i(x)$ is the flux species i at a distance x from electrode surface, D_i is the diffusion coefficient, $\frac{\partial C_i(x)}{\partial x}$ is concentration gradient of x, $\frac{\partial \phi(x)}{\partial x}$ is the potential gradient, z_i is the charge(dimensionless), C_i is the concentration and $v(x)$ is the bulk velocity of solution. The ohmic conductivity for the standard electrolyte 0.2 M and 0.4 M potassium ferri/ferro cyanide is 10.09 and 16.5 S/m respectively [70]. Nano fluids have been utilized to increase the ohmic conductivity. While most studies have been about low ohmic strength solutions in water or ethanol, because solution having high ohmic strength suffer from sedimentation and aggregation. This is due to poor stability of the solute. A recent work show increase in ohmic conductivity for 0.2 M potassium ferro/ferricyanide from 10.3 to 10.9 S/m by introducing water-based alumina nanofluid and sodium dodecyl sulfate [71].

The rate of reaction at the electrode is governed by Butler-Volmer equation [72]:

$$j = nFk^o exp\Big[\frac{E}{R}(\frac{1}{T^o} - \frac{1}{T})\Big]\Big[C_O exp\Big(\frac{-nF(1-\beta)\xi}{RT}\Big) - C_R exp\Big(\frac{nF\beta\xi}{RT}\Big)\Big] \tag{2.4}$$

where j is the current at the respective electrode, n is the number of electron, F is the faraday's constant, k^o is the standard electrode constant, E is the activation energy for

reaction, R is the universal gas constant, T^o is the standard temperature, C_O is the oxidized concentration, C_R is the reduced concentration, β is the charge transfer coefficient and ξ is the overpotential at the electrode.

2.4 Modeling of thermocells

Modeling of thermocells, have enabled to gain insights into the various electrical and thermal transport phenomenons happening inside a thermocell. One of the earlier computer analysis is by Ikeshoji et al., the work was divided in two parts. The first part used Navier-Stokes equation and Onsager equation of fluxes of the two salts [77, 78]. The experimental current response to applied voltage for isothermal and non-isothermal cell were both reproduced numerically. The work highlighted role of development of two boundary layers for non-isothermal cell i.e. thermal and concentration boundary layers. The large increase in current and relatively small increase in heat transfer was attributed to large increase in concentration and less increase in thermal boundary layers, respectively. This relatively different development of boundary layers stem from the large difference of heat and mass transfer diffusivity. In second part, the relation between voltage-current, power output and heat flux was investigated to replicate experimental results.

Sokirko investigated horizontal and vertical configuration of electrodes in thermocells. For horizontal configuration, diffusion-migration and for vertical configuration, diffusion-convection relation were used [79].

2.5 Operation of thermocells

Thermocells consist of two main components the electrolyte and the electrode (Figure 2.6). The electrolyte is sandwiched between two electrodes. When a temperature difference is applied at the electrodes, oxidation and reduction takes place at the respective electrode. Preference to oxidation or reduction depends on temperature at the electrodes. The chemical equilibrium equation for a common redox couple present in potassium ferri/ferrocyanide

$(Fe(CN)_6^{3-}/Fe(CN)_6^{4-})$ is given as follows:

$$Fe(CN)_6^{4-} \rightleftharpoons Fe(CN)_6^{3-} + e^- \tag{2.5}$$

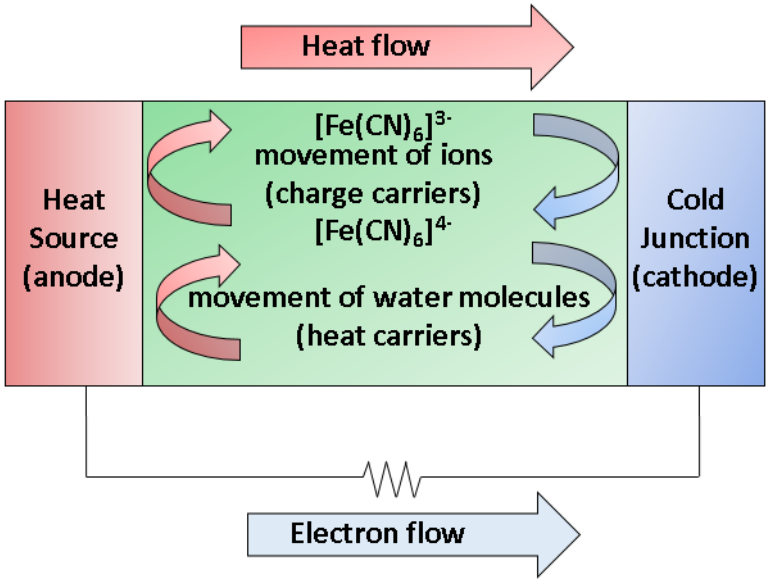

Figure 2.6: Schematic of thermocell showing the the flow of heat and electrons, movement of ions and water molecules for ferri/ferrocyanide electrolyte.

At the higher temperature electrode the equilibrium shifts in forward direction and oxidizes (producing electrons), while at the lower temperature electrode it shifts in the backward direction and reduces (consuming electrons). The higher temperature electrode behaves as an anode and lower temperature electrode behaves as a cathode. The shift in equilibrium is explained by Le Châtelier's principle or "The Equilibrium Law" which states that when any system is subjected to change such as temperature, the systems adjust itself to counterbalance the effect of the applied change. The free energy difference of products and reactants at the electrodes generates the thermo-electrochemical force (also known as an electromotive force, EMF). The resultant ions after being oxidized/reduced at a specific electrode, get transported to opposite electrodes in the thermocell. Meanwhile the electrons generated at the anode, due to the oxidation of ions flow through the external circuit

from anode to cathode and consequently get consumed by the ions reducing at the opposite electrode.

The maximum power output of thermocell [79] is given by Equation 2.6:

$$P_{max} = 0.25 * V_{oc} * I_{sc} \tag{2.6}$$

where V_{oc} is the open circuit voltage and I_{sc} is the short circuit current. The power conversion efficiency is defined as the ratio of maximum power output to the thermal power flowing through the cell. The thermal power $\dot{\mathrm{Q}}$ is defined as the sum of thermal conduction through the cell ($\dot{\mathrm{Q}}_i$) and the rate of heat transfer due to reversible heat of the cell reaction ($\dot{\mathrm{Q}}_r$). $\dot{\mathrm{Q}}_r$ is only significant if there is a net consumption of electrolyte. However, for electrolytes in the present study which are designed for continuous operation, the efficiency formula is given by Equation 2.7:

$$\phi = \frac{P_{max}}{kA(\partial T/\partial x)} \tag{2.7}$$

where k is the thermal conductivity of the electrolyte, A is the cross-sectional area of the electrode. To compare the performance of thermocells operating between various temperatures, a parameter called relative Carnot efficiency was defined as:

$$\phi_r = \frac{\phi}{\Delta T/T_H} \tag{2.8}$$

where ΔT is the temperature difference between hot and cold electrodes and T_H is the hot electrode temperature. Earlier literature on thermocell dealt with developing understanding and methods to study the effect of temperature on voltage generated by various redox pairs [35, 80, 81]. Subsequent efforts shifted to studying the discharge behavior of voltage produced from the temperature [82], as a result ohmic, mass and charge transfer over potentials were identified to limit thermocell performance [34, 69]. These over potentials are

shown as resistances in Figure 2.7.

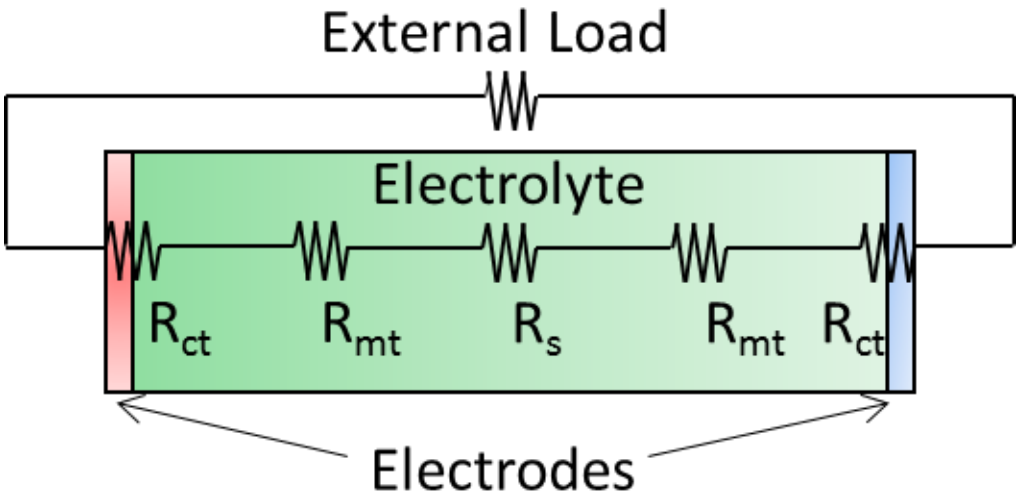

Figure 2.7: Schematic of over potential represented as resistances. Rs is ohmic resistance, Rct is interfacial charge transfer resistance and Rmt is mass transfer resistance.

Various aqueous systems such as Cu^{2+}/Cu, Fe^{2+}/Fe, Pu^{4+}/Pu^{3+} and Np^{4+}/Np^{3+} systems have been studied over time [82, 83, 35, 84]. Ferri/ferro cyanide has been extensively studied due to high Seebeck coefficient and high current exchange density [34, 83, 85]. Apart from these properties which have direct impact on power output, ferri/ferro cyanide is suitable for more reliable operation as it does not poison or corrode the electrode surface [83]. Seebeck coefficient was studied as a function of electrolyte concentration, showed decreasing the concentration, increased value of the Seebeck coefficient [86, 87]. This was in agreement with Debye-Hückel treatment of the electrostatic interactions between ions, which predicts linear variation of Eastman entropy of transport with square root of the ionic strength [88]. However, the slight increase in open circuit voltage offset by a dramatic reduction in the current. To improve thermocell performance, ratio of the flux of charge carriers and the flux of heat flowing between electrodes should be as high as possible [83]. From heat transfer perspective thermal conductivity of the electrolyte is important. Decreasing the thermal conductivity, enables maintenance of high temperature with lesser thermal energy input. Similar to solid state thermoelectrics, increase in ratio of charge

carriers to heat flux is necessary to improve the efficiency of thermocells. The recent focus of research has been on improving the performance of thermocells by making better electrodes and by increasing the operating temperature of thermocells. The introduction of multiwalled carbon nanotubes (MWNTs) [47, 51] and single walled carbon nanotube (SWNTs) combined with reduced graphene oxide (RGO) [48] has greatly reduced the cost of thermocells. Also, power as high as 6.6 W/m^2 has been reported [49] by fabricating carbon nanotube aerogel sheet electrodes. In addition, an earlier limitation of operating temperatures above 100 ^{o}C has also been addressed by use of ionic liquids as the redox electrolyte [89]. Recent developments have addressed the costs and material limitations that makes thermocells economically more feasible and operational to temperatures up to 200 ^{o}C. This thesis focuses on improving electrochemical properties and implementation techniques of the thermocell development process in a practical sense, in order to function as an energy harvester and a cooling device.

2.6 Application of thermocells

With the introduction of carbon nanotube electrodes the cost of thermocells decreased dramatically and the focus of research has moved to application. Thermocells have been shown to recover heat from vehicles and human body.

Gunawan et al. developed thermocell to simulate energy harvesting from automobile [54]. A climate controlled wind tunnel (Figure 2.8) was built to simulate ambient air flow present beneath the car. Aqueous $CuSO_4$ was used as electrolyte with Cu metal as electrodes. The power measured was in tens of mWm^{-2} i.e. about 4 to 5 orders of magnitude lower than solid state thermoelectrics. However, the cost was lower than its solid state counterparts.

Flexible thermocells have been developed to utilize body heat as shown in Figure 2.9 [56]. Thermocell was made of plastic material such as polyethylene terephthalate (PET) and is flexible enough to be easily worn on a human body. Porous CNT electrodes were

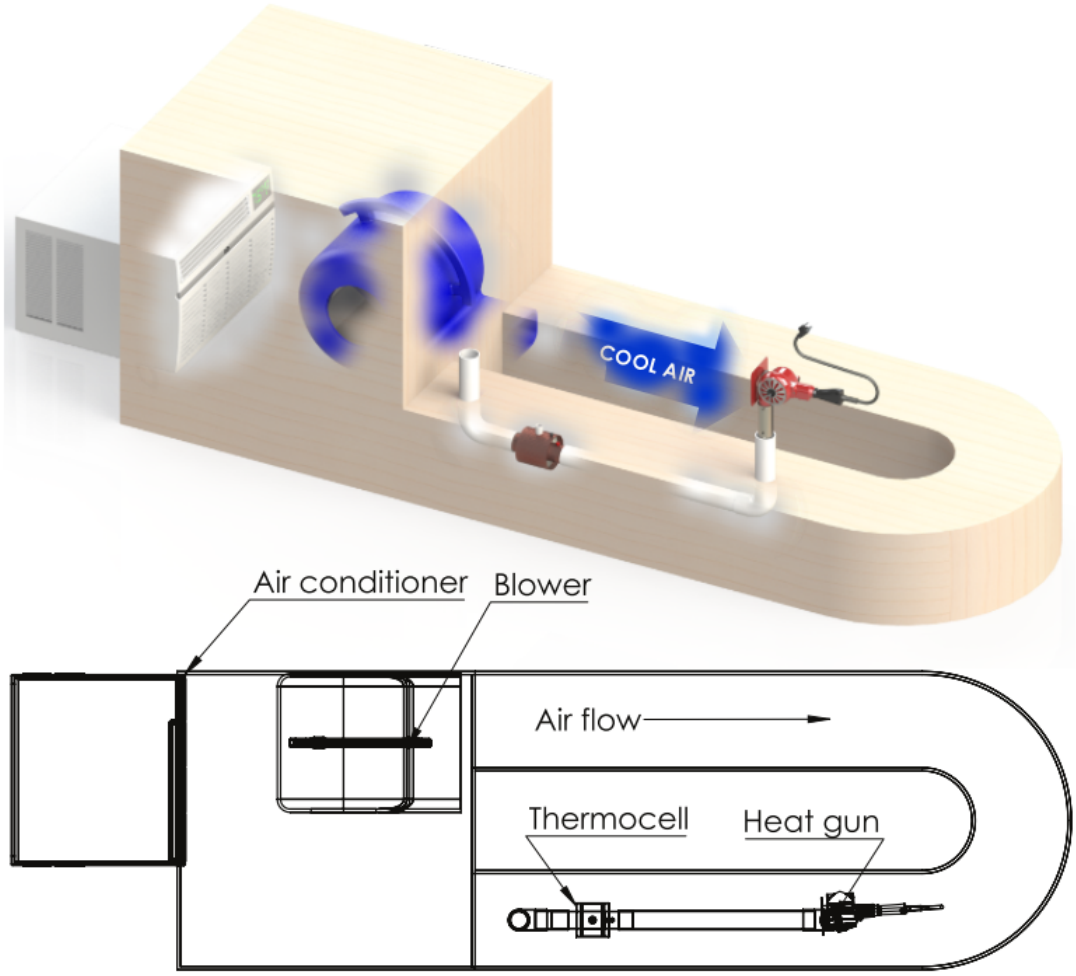

Figure 2.8: Schematic of Climatic control tunnel to simulate thermocell present below a vehicle. Republished with permission from [54]. Copyright (2015) ASME Power Conference.

used in carbon textiles to maximize the performance by lowering the charge transfer resistance at the electrode/electrolyte interface. For cold weather conditions with an ambient temperature of 5 ^oC and body temperature of 36 ^oC, a maximum power density of 0.46 mW/m^2 was achieved. As the instantaneous power extracted was less, a capacitor was used to store charge for practical use.

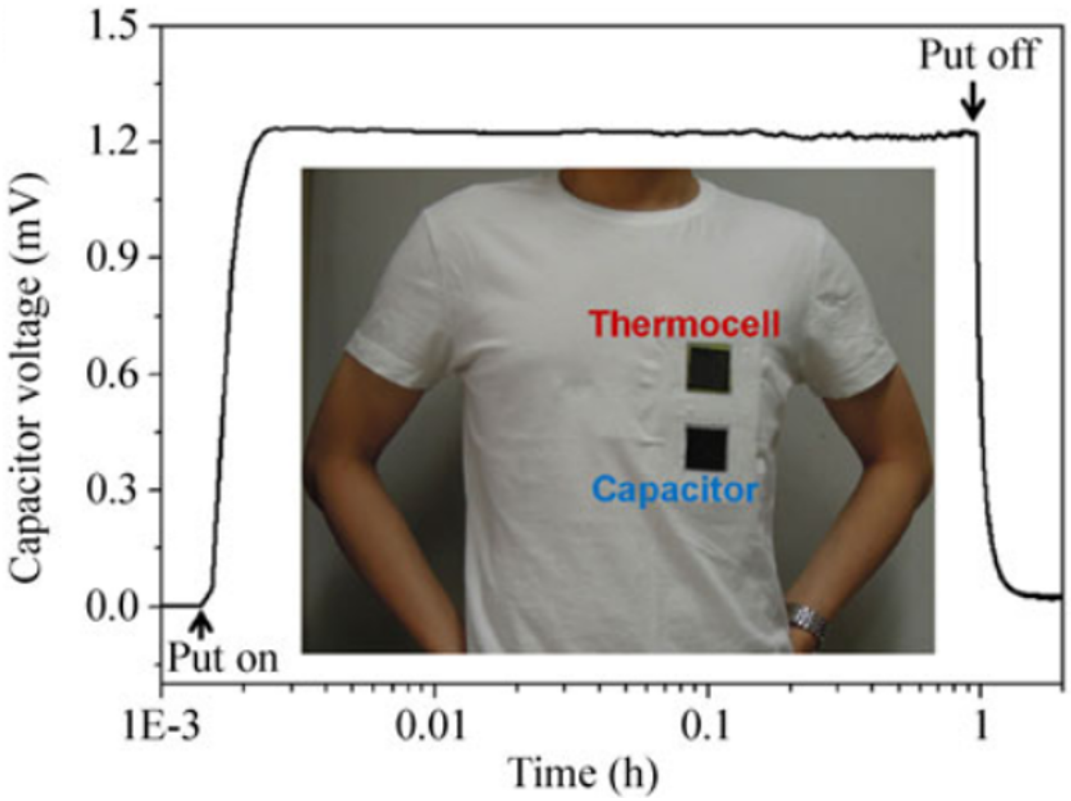

Figure 2.9: Photograph shows T-shirt have thermocell and capacitor. Reprinted with permission from [56]. Copyright (2014) Springer.

2.7 Different types of thermocells

Battery-type thermocell: Seebeck effect has been demonstrated in a cell having Lithium battery architecture (Figure 2.10) with electrodes structured to intercalate charge [73]. The electrode and electrolyte are made of same active material. The Seebeck coefficient of oxide layers was -6.8 $\mu V/K$ for $LiCoO_2$, -29.7 $\mu V/K$ for $Na_{0.52}MnO_2$, -12.7 $\mu V/K$ for $Na_{0.99}CoO_2$ and -22.4 $\mu V/K$ for $Na_{0.51}Mn_{0.5}Fe_{0.502}$.

Capacitor type thermocell: Another type of thermocell is to use the temperature difference to store charge [74]. It is called thermally chargeable capacitor. 1-ethyl-3-methylimidazolium bis(trifluoromethylsulfonyl)-imide in acetonitrile is subjected to temperature difference to its electrodes. It was found that the S_e is -1.7 mV/K for platinum electrodes and -0.3 mV/K for porous carbon electrodes. The capacitance of 5 μF was measured with plat-

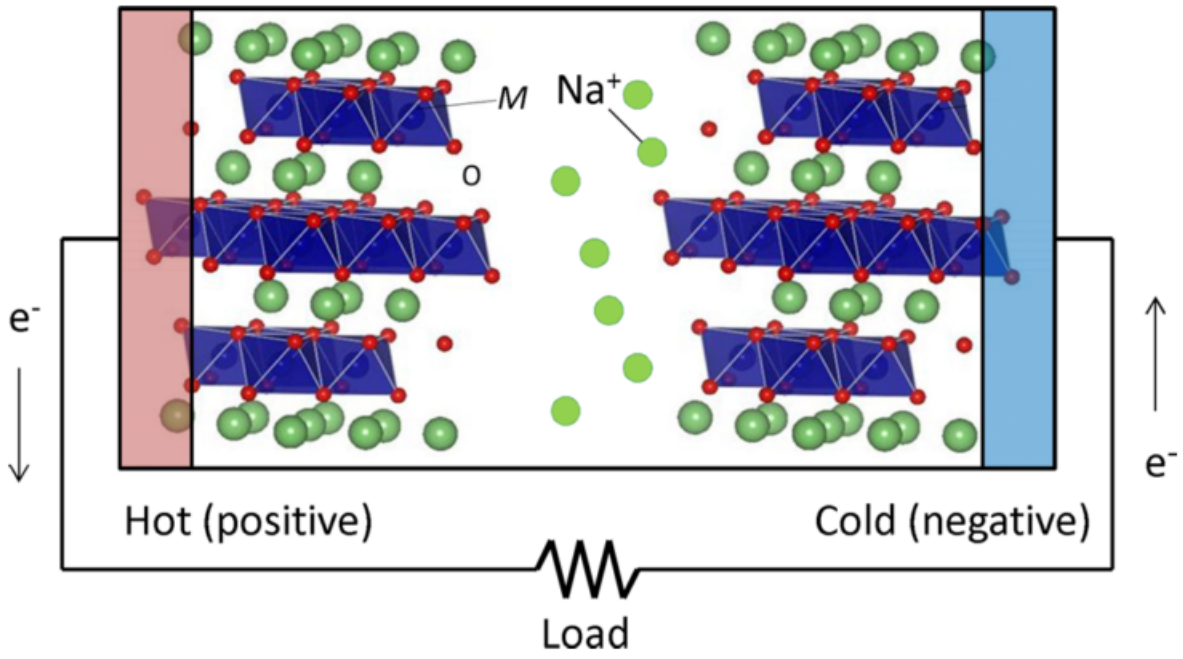

Figure 2.10: Schematic of battery type thermocell, it consists of two paste-type electrodes having the same active material. The active material shown is Na_xMO_2, where M is a transition metal. Reprinted with permission from [73]. Copyright (2015) AIP Publishing.

inum electrodes while for carbon electrodes it was about four order of magnitude higher at 36 mF.

Thermodynamic cycle of battery: An electrochemical system using Seebeck effect in thermodynamic cycle has been built and it is called thermally regenerative electrochemical cycle (Figure 2.11) [75]. It uses solid copper hexacyanoferrate (CuHCF) having a negative S_e as a positive electrode and Cu/Cu^{+2} having a positive S_e as a negative electrode in an aqueous electrolyte. In process 1, the cell is in its initial discharge state and is heated up, the S_e of the two components are such that open circuit voltage decreases. In process 2, the cell being at low voltage is charged with an external battery, and the entropy of the cell increases due to electrochemical reaction. In process 3, the cell is cooled and S_e are such that the open circuit voltage increases. In process 4, the cell is discharged at the low temperature and the entropy of the cell decreases. As charging voltage is less than voltage at the time of discharge, net work is extracted from the cell. This work has shown a good

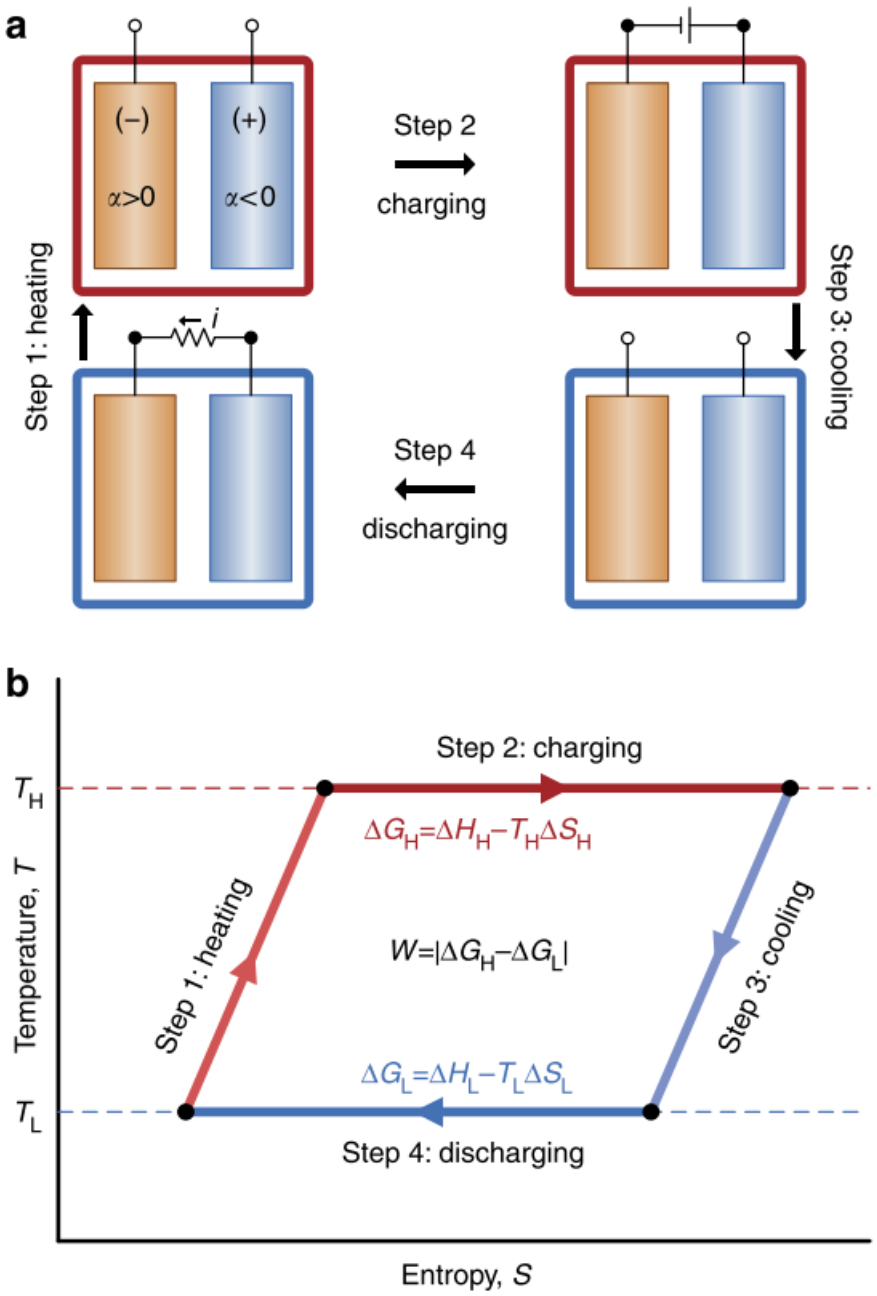

Figure 2.11: Working of thermally regenerative electrochemical cycle. (a)Schematic shows thermodynamic cycle: process 1, heating the cell; process 2, heating at constant high temperature (charging); process 3, cooling the cell; process 4, discharging. (b) Temperature-entropy diagram for the thermodynamic cycle between two constant temperatures T_H and T_L. Reprinted by permission from Macmillan Publishers Ltd: Nature communications [75], copyright (2014).

thermal to electricity conversion efficiency of 5.7 %.

Thermochargeable thermocell: Thermochargeable cell uses a temperature gradient to

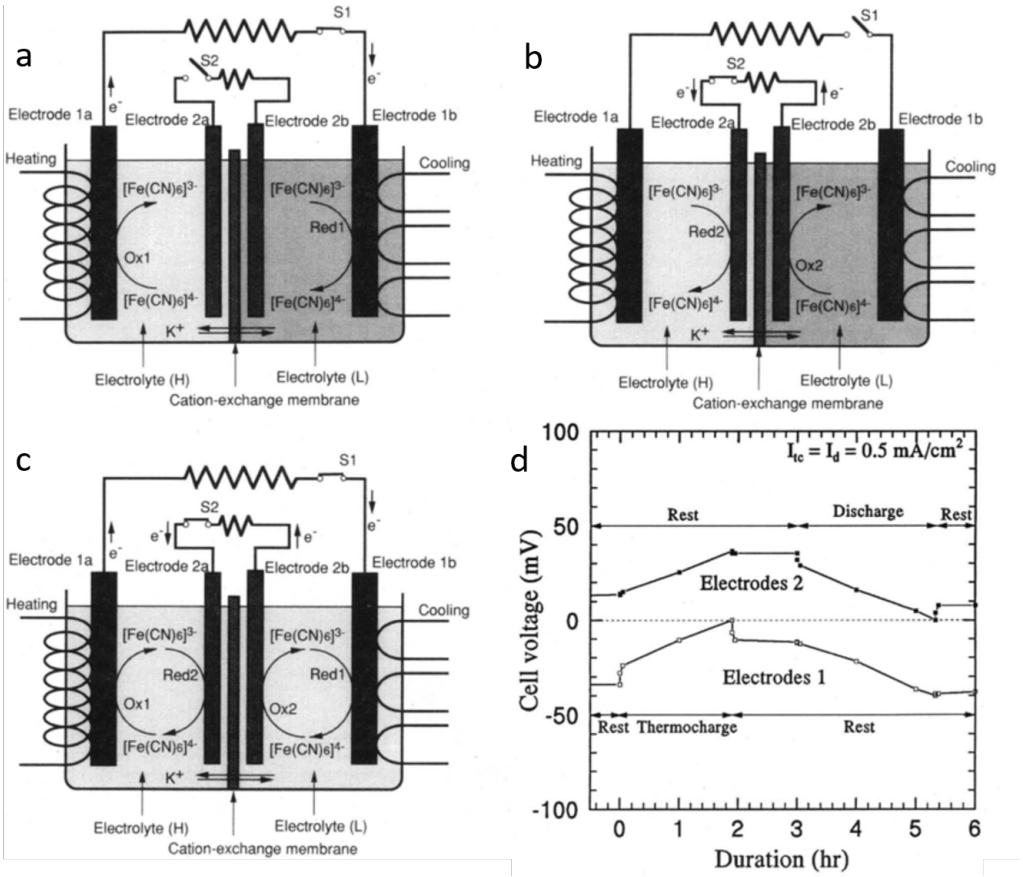

Figure 2.12: Schematic shows thermochargeable thermocell with potassium ferri/ferro cyanide as the electrolyte. (a) Schematic shows thermocharging taking place with the help of temperature gradient applied to electrode 1a and 1b, concentration gradient build up in the two compartments. Also electricity is supplied to external circuit. (b) Once temperature difference is removed, the cell is discharged by supplied electricity to external circuit. (c) Thermocharging and discharging taking place simultaneously.(d) The cell voltage as a function of time, electrodes 1a and 1b are thermocharged at 0.5 mA/m^2 and later electrodes 2a and 2b are discharged at 0.5 mA/m^2, after one hour interval. Reprinted with permission from [76]. Copyright (1996) Journal of the Electrochemical Society.

not only produce electricity but also build up concentration gradients, in the two compartment separated by cation-exchange membrane [76]. Figure 2.12a-c to see show the various configuration of thermochargeable cell. The main electrode 1a and 1b are attached to hot and cold reservoirs. Midway between the electrodes is a cation-exchange membrane which only allows passage of positive potassium counterions (K^+) and restrict movement of $Fe(CN_6)^{4-}$ and $Fe(CN_6)^{3-}$ redox ions. Another pair of electrodes 2a and 2b are placed in the two compartments.

Thermocharging is shown in Figure 2.12a. The switch S1 closed and switch S2 is opened. The applied temperature difference generates electricity, which is also being discharged by keeping S1 closed. As the membrane restricts flow of redox species, concentration gradient build up in the two compartments. Figure 2.12b switch S1 is opened and switch S2 is closed, concentration potential developed in the last stage is now discharged. Figure 2.12c shows simultaneous use of charge and discharge cycle. The cell has good thermocharge and discharge cycle ability. For discharge current of 0.5 mA/cm^2 and thermocharge current of 0.1 mA/cm^2, the ratio of discharge to thermocharge was more that 90 $\%$.

2.8 Summary

The chapter provides an overview of the literature on thermocells from its origin to current state of research. The chapter starts with describing the driving principle of Seebeck coefficient, followed by describing two main parts of thermocell the electrode and electrolyte, the governing equations of ohmic conductivity are described, followed by modeling of thermocells. The aforementioned sections are amalgamated in the working of thermocells. The chapter concludes with the applications of thermocells and its variants which have the same operating principle.

CHAPTER 3

ELECTROCHEMICAL CHARACTERIZATION OF CARBON NANOTUBE AND POLY (3,4-ETHYLENEDIOXYTHIOPHENE)POLY(STYRENESULFONATE) COMPOSITE AQUEOUS ELECTROLYTE FOR THERMO-ELECTROCHEMICAL CELLS

3.1 Introduction

Aqueous potassium ferri/ferrocyanide electrolyte has been the standard electrolyte for thermo-electrochemical cells due to its high seebeck coefficient and high current exchange density. Here, the effect of mixing carbon nanotubes and poly (3,4-ethylenedioxythiophene) poly(styrenesulfonate) in aqueous potassium ferri/ferrocyanide electrolyte is characterized using electrochemical impedance spectroscopy. Analysis of the impedance spectra shows a 10% increase in ohmic conductivity and about 5-fold decrease in interfacial charge transfer resistance in the composite electrolyte, which is caused by addition of charge carriers, interfacial polarization and improved contact at the electrode/electrolyte interface. The enhancement of properties in the composite electrolyte increases the power of a thermo-electrochemical cell by about 30 %.

In our previous work, we showed that addition of MWNTs to ionic liquid electrolyte can reduce mass transfer resistance and increase power output [43]. However, the viscosity of ionic liquids is at least an order of magnitude greater than that of water [95], which decreases the rate of ion diffusion and hence the ohmic conductivity of the electrolyte [43]. The highest ionic conductivity of ionic liquid is much lower than aqueous electrolyte [96], thus conventional 0.4 M ferri/ferrocyanide ($Fe(CN)_6^{3-}$/ $Fe(CN)_6^{4-}$) remains a first choice electrolyte for thermocells. In this paper, we mix 0.4 M $Fe(CN)_6^{3-}$/ $Fe(CN)_6^{4-}$ with MWNTs and poly(3,4-ethylenedioxythiophene):poly(styrenesulfonate) (PEDOT:PSS) to

form a novel composite electrolyte. Nanoparticle addition to liquid electrolyte has been shown to reduce interfacial charge transfer resistance in previous studies [97, 98, 99, 100]. Carbon nanotubes (CNTs) have been previously shown to disperse in stabilizers such as polymers [101, 102, 103] and surfactants [104, 105]. Recently PEDOT:PSS has also been shown to stabilize and disperse CNTs in water. The conjugated polymer wraps around CNTs preventing aggregation and settling [106, 107]. Combining the physicochemical properties of conjugated polymer and long range ballistic electrical conduction of CNTs have already been used in thermoelectrics [108], dye-sensitized solar cells [109, 110] organic thin film transistors [111], organic photovoltaics [111] and organic light emitting diodes [112] to improve their performance and reduce cost [111]. In the aforementioned devices the composite is used either as a film or electrode, but in this work for the first time the composite is dispersed in an aqueous system having a redox couple $Fe(CN)_6^{3-}$/ $Fe(CN)_6^{4-}$.

Increase in ohmic conductivity (decrease in ohmic over potential) of aqueous redox electrolyte is achieved by the introduction of PEDOT:PSS and MWNTs. In addition, up to a 5 times decrease in interfacial charge transfer resistance in this composite electrolyte. Increases in ohmic conductivity and reduction in interfacial charge transfer resistance with the new composite electrolyte produce a significant increase in power output.

3.2 Experimental

3.2.1 Materials and preparation

MWNTs (US4315) manufactured from chemical vapor deposition were purchased from US Research Nanomaterials, Inc. According to product specifications the purity is greater than 95 % (from thermogravimetric analysis and transmission electron microscopy), the outside diameters are 50-80 nm, the lengths are 10-20 μm and the density is 2.1 g/cm^3. PEDOT:PSS (PH1000) highly conductive homogenized dispersion was purchased from Heraeus Clevios. According to product specifications the solid content is 1-1.3 %, viscosity

is 15-50 mPas, the PEDOT:PSS ratio by weight is 1:2.5 at 20 oC and the density is 1 g/cm^3. Potassium hexacyanoferrate (II) trihydrate and Potassium ferricyanide (III) were purchased from Sigma Aldrich having a molecular weight of 422.39 g/mol and 329.26 g/mol, respectively.

Mixtures of PEDOT:PSS and water were made by stirring for 30 min. MWNTs were dispersed at different ratios in PEDOT:PSS dispersions by 30 min of stirring, 30 min of sonication and then 15 min of stirring. Composites of MWNT and PEDOT:PSS prepared in the previous step were dispersed in $Fe(CN)_6^{3-}$/ $Fe(CN)_6^{4-}$ by 30 min of stirring, 30 min of sonication and then 15 min of stirring. The sonication was done using an ultrasonic bath having a frequency of 40 kHz and stirring was done using magnetic stirrer at a speed of 1200 rpm. All steps were performed at ambient temperature.

3.2.2 Electrochemical impedance spectroscopy

Electrochemical impedance spectroscopy (EIS) and modelling was performed using the procedure used in our previous work [43]. Briefly, two platinum electrodes were used in the electrochemical setup. EIS was performed using CH instruments model 660E potentiostat in the spectral range 1 MHz-0.02 Hz, with an AC amplitude of 20 mV and DC signal of 0 mV. The collected data was fitted using the software provided by CH instruments. Randles model was used to compute ohmic resistance, R_s, interfacial charge transfer resistance, R_{ct}, Warburg or diffusion impedance, W, and double-layer capacitance, C_{dl}. The Randles equivalent circuit helps in separating the behaviour in the bulk solution from that at the interface. R_s was used to calculate ohmic conductivity, σ, of the electrolyte by calibrating it with 0.1 M and 1 M standard solution of potassium chloride as shown in our previous work [43, 44].

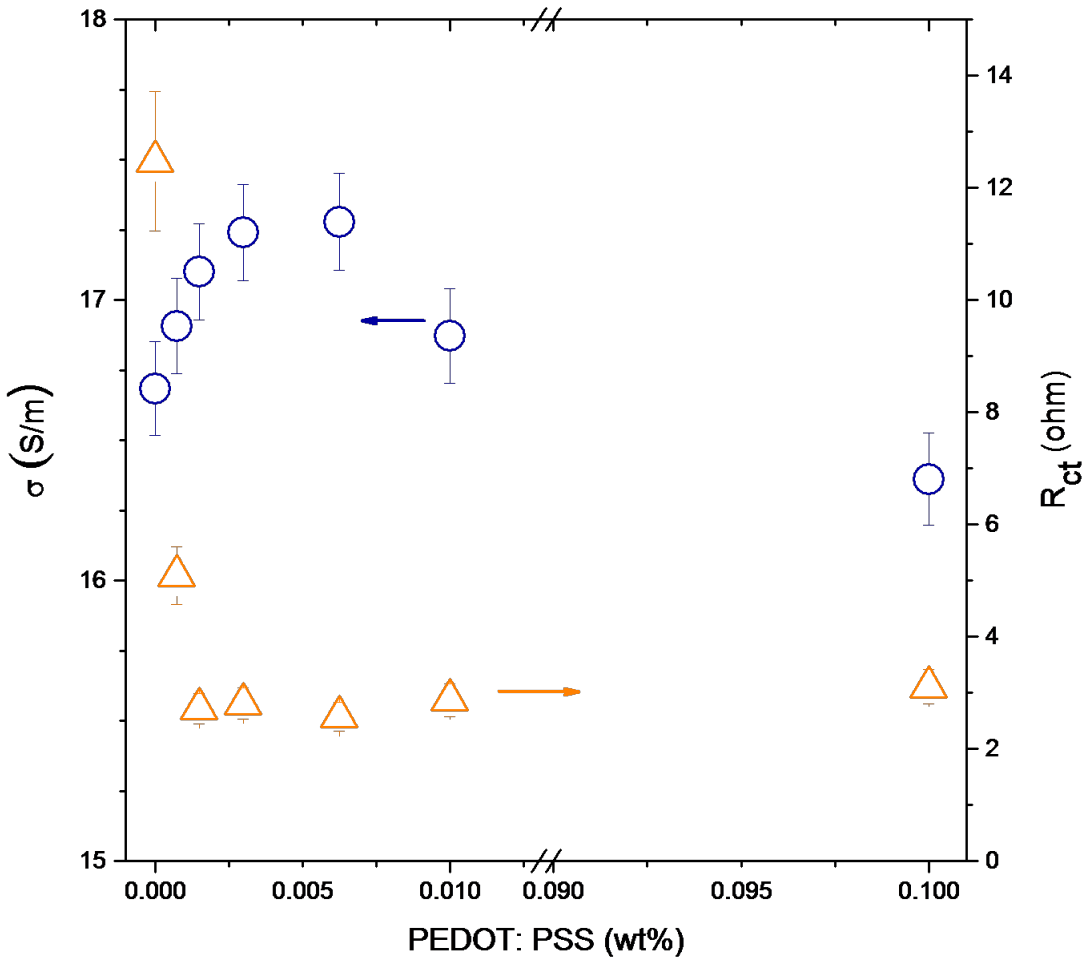

Figure 3.1: Effect of increasing PEDOT:PSS (wt%) on conductivity and interfacial charge transfer resistance of 0.4 M $Fe(CN)_6^{3-}$/ $Fe(CN)_6^{4-}$. σ is the ohmic conductivity of the solution (blue circle), R_{ct} is the interfacial charge transfer resistance (orange triangle).

3.2.3 Cyclic Voltammetry

Cyclic Voltammetry (CV) was performed using three-electrode cell configuration. The working and counter electrode were of Platinum while the reference electrode Ag/AgCl. CV sweeps were performed using CH instrument model 660E potentiostat for the range -0.3 to 0.7 mV using a scan rate 0.1 V/s. For each sample CV sweep was recorded for temperature range 293 to 353 K, having 5 K increment. CV was used to calculate ΔTS, S_e and to observe the shift in half-wave potential ($E_{1/2}$) with temperature using the method described previously [113, 72].

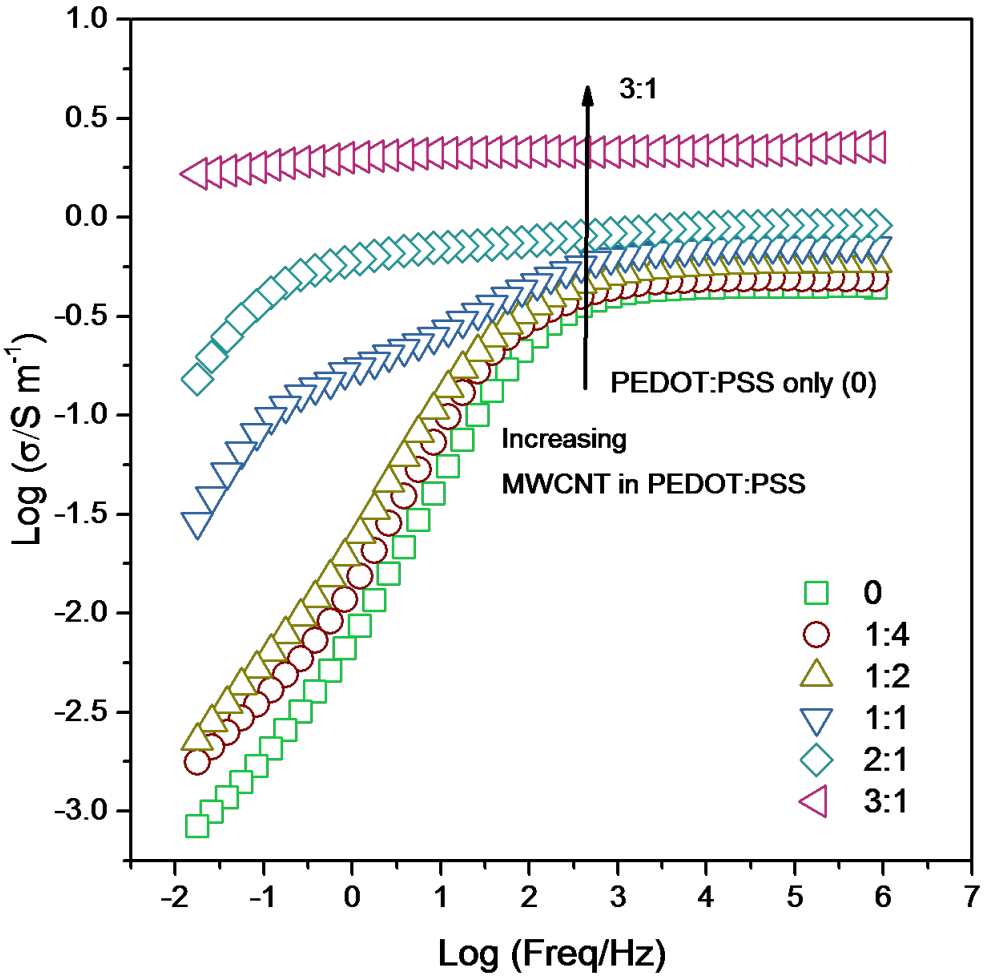

Figure 3.2: Frequency dependence of impedance at increasing concentration ratio of MWNT, 0 (green) only PEDOT:PSS, MWNT:(PEDOT:PSS) varying from 1:4 (wine) to 3:1 (pink).

Calculating Seebeck coefficient: Cyclic Voltammetry was performed using three-electrode cell configuration as described in main text. All potentials were recorded with reference to Ag/AgCl reference electrode (Figure A.3). Anodic peak (E_{pa}) and cathodic peak (E_{pc}) potentials were obtained using the software provided by CH instrument. Half-wave potential ($E_{1/2}$) is determined as

$$E_{1/2} = \frac{E_{pa} + E_{pc}}{2} \tag{3.1}$$

Half-wave potential was measured versus temperature and plotted as shown in Fig-

ure 3.4. The slope of the graph gives the Seebeck coefficient and can be shows as

$$S_e = \frac{(E_{1/2})_{T_1} - (E_{1/2})_{T_2}}{T_1 - T_2} \tag{3.2}$$

where $(E_{1/2})_{T_1}$ and $(E_{1/2})_{T_2}$ are half-wave potential measured at temperature T_1 and T_2 respectively.

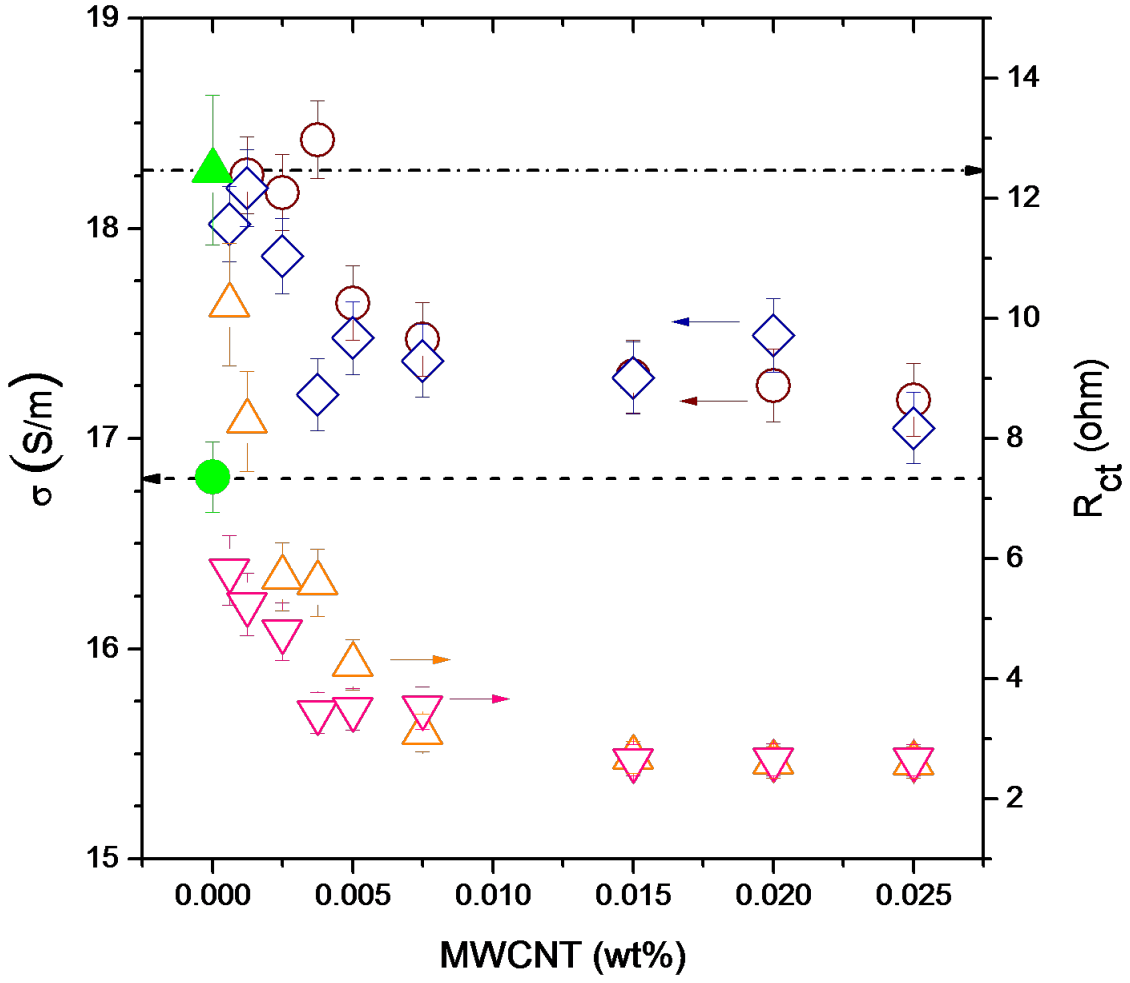

Figure 3.3: Effect of MWNT, PEDOT:PSS composite on 0.4 M $Fe(CN)_6^{3-}$/ $Fe(CN)_6^{4-}$. MWNT:(PEDOT:PSS) 1:4 in 0.4 M $Fe(CN)_6^{3-}$/ $Fe(CN)_6^{4-}$ σ (blue diamond) and R_{ct} (pink down triangles), MWNT: (PEDOT:PSS) 3:1 in 0.4 M $Fe(CN)_6^{3-}$/ $Fe(CN)_6^{4-}$ σ (brown circles) and R_{ct} (yellow triangles). Upper dash dot line is the initial value of R_{ct} correspond to green solid triangle, lower dash line is the initial value of correspond to green solid circle. Both green solid triangle and green solid circle correspond to 0 wt% MWNT in the composite.

3.2.4 Thermocell measurements

A T-shaped cell was used to perform thermocell testing for temperature differences (ΔT) 20, 40, 60, 80 and 100 K between the heating and cooling blocks. Graphite electrodes having a cross-sectional area of 0.08 cm^2 were used as the two electrodes. The heating block is heated by two Omega 7750 W/m^2 silicones rubber heaters. The cooling block is maintained at ambient temperature by the environment. The performance of 0.4 M $Fe(CN)_6^{3-}$/ $Fe(CN)_6^{4-}$ electrolyte was compared with the same electrolyte with different concentrations of PEDOT:PSS and PEDOT:PSS/MWNT composites. The thermocell testing was done with a potentiostat by recording open circuit voltage and short circuit current. The measurements were repeated after 12 hour intervals to check for stability.

3.3 Results and discussion

3.3.1 Electrochemical impedance spectroscopy

In order to introduce MWNTs and PEDOT:PSS to the aqueous redox electrolyte, a systematic procedure was followed. First, the PEDOT:PSS dispersion was added to water and an increase in ohmic conductivity was measured (Table A.1). The increase is ohmic conductivity is seen because PEDOT:PSS is a conductive polymer having positive and negative ions. Increasing the amount of PEDOT:PSS increases the number of ions in distilled water and hence reduces the ohmic resistance Rs.

The next step was to add PEDOT:PSS to aqueous 0.4 M $Fe(CN)_6^{3-}$/ $Fe(CN)_6^{4-}$ (Figure 3.1). This increases the ohmic conductivity, which is attributed to the addition of the ions present in PEDOT:PSS. However, higher concentration of 0.1 wt% PEDOT:PSS suppresses the ohmic conductivity, probably because the effect of increase in number ions is offset by increase in viscosity of the mixture [43, 98, 44]. In addition, interfacial charge transfer resistance is decreased significantly (Figure 3.1). This shows that increase in conductive polymer not only increases the bulk transport of redox couple but also increases

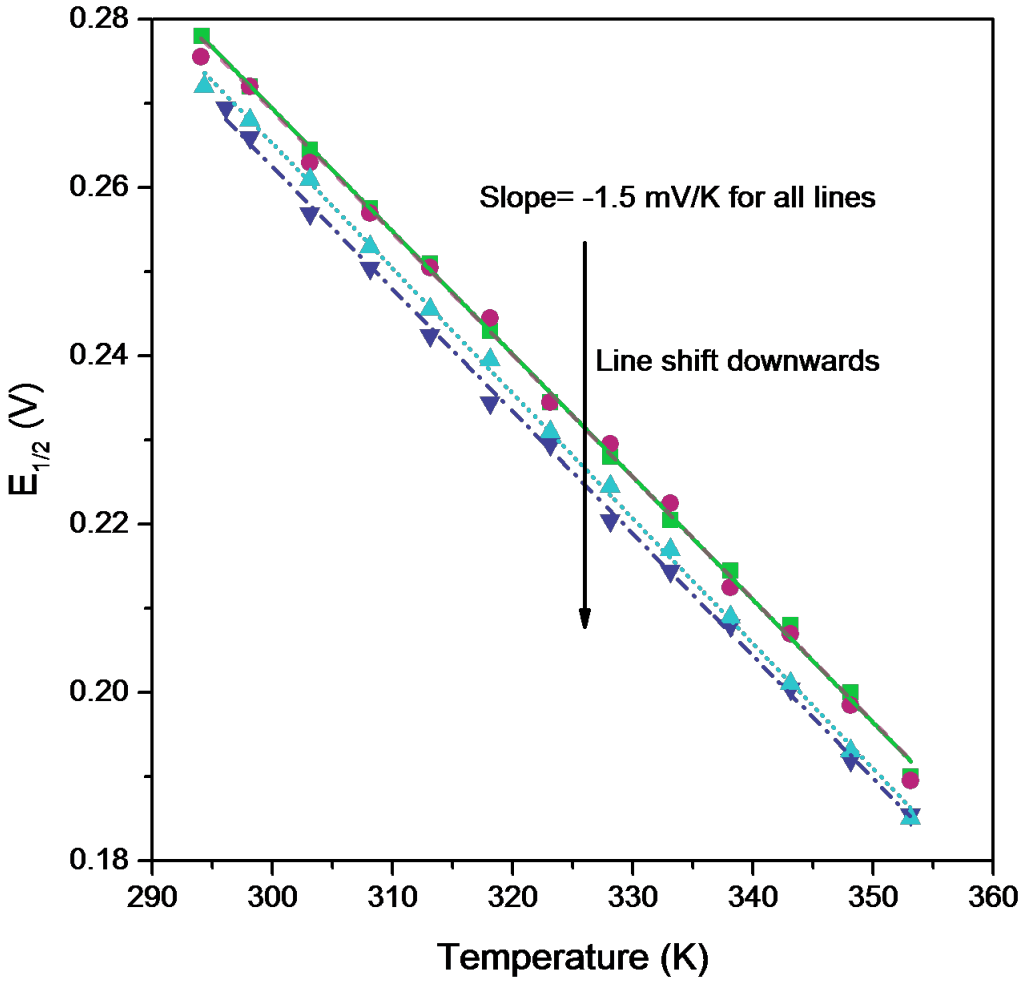

Figure 3.4: Half-wave potential of 0.4 M $Fe(CN)_6^{3-}$/ $Fe(CN)_6^{4-}$ (green square), 0.4 M $Fe(CN)_6^{3-}$/ $Fe(CN)_6^{4-}$ + 0.00625 wt% PEDOT:PSS (pink circle), 0.4 M $Fe(CN)_6^{3-}$/ $Fe(CN)_6^{4-}$ + 0.06 wt% PEDOT:PSS + 0.015 wt% MWNT (blue triangle up), 0.4 M $Fe(CN)_6^{3-}$/ $Fe(CN)_6^{4-}$ + 0.005 wt% PEDOT:PSS + 0.015 wt% MWNT (purple triangle down) as a function of temperature of isothermal cell.

the rate of charge transfer at the electrode. This implies that increasing wt% of conductive polymer improves contact between the electrode and electrolyte.

The effect of MWNTs on the PEDOT:PSS dispersion is shown in Figure 3.2. A gradual increase in conductivity is observed over the entire frequency range for each increment of MWNT concentration. For small concentration of MWNT the spectrum shifted slightly maintaining its shape, however at higher concentrations of MWNTs the change in spectrum was more significant, especially at lower frequency. It has been shown that polymer

helps disrupt the CNT hydrophobic interaction with water and also disrupts the CNT-CNT interaction, which prevents aggregation [114]. This behavior helps in dispersing CNTs in polymer, forming a composite, which later can be dispersed in electrolyte. Conjugated polymers have been known to display good binding with CNTs; in the absence of chemical functionalization the polymer CNT interaction is solely by van der Waals forces [115, 116, 117]. The MWNTs were added to a high 3:1 ratio MWNT:(PEDOT:PSS). The increase in conductivity shows the creation of percolated networks and interfacial polarization [43] that facilitate charge transfer. At a higher MWNT concentration the spectra matches that of a resistor (i.e., frequency independent).

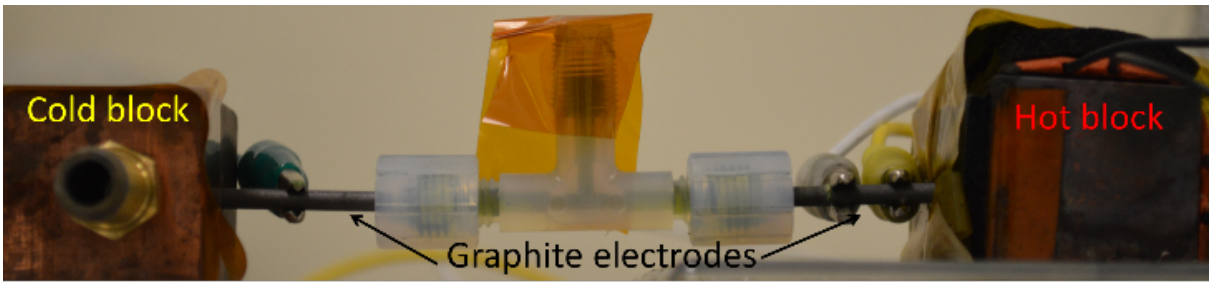

Figure 3.5: Photograph of t-shape thermocell experimental setup to generate power.

Finally, the electrolyte composite of MWNTs and PEDOT:PSS was added to 0.2 M $Fe(CN)_6^{3-}$/ $Fe(CN)_6^{4-}$ (Table A.2 and Table A.3) and 0.4 M $Fe(CN)_6^{3-}$/ $Fe(CN)_6^{4-}$ (Figure 3.3 and Figure A.2). Ohmic conductivity of 0.4 M $Fe(CN)_6^{3-}$/ $Fe(CN)_6^{4-}$ (Figure 3.3) is about 1.7 times greater than that of 0.2 M $Fe(CN)_6^{3-}$/ $Fe(CN)_6^{4-}$(Table A.2 and Table A.3). For both the lean (4 times less than PEDOT:PSS) and rich (3 times more than PEDOT:PSS) mixtures of MWNT similar trends of R_{ct} and σ were observed. A slight increase in ohmic conductivity was observed, while the decrease in interfacial charge transfer resistance was much more significant for both mixtures. Lean mixture of MWNT had a maximum increase of 8 % in ohmic conductivity for 0.00125 wt% of MWNT (PEDOT:PSS 0.005 wt%). Also, for the same ratio, about a 5 times decrease in interfacial charge transfer resistance was observed for 0.015 wt% of MWNT. As for the rich MWNT mixture about 10% increase in ohmic conductivity was observed for 0.00375 wt% of MWNT and about a 5 times de-

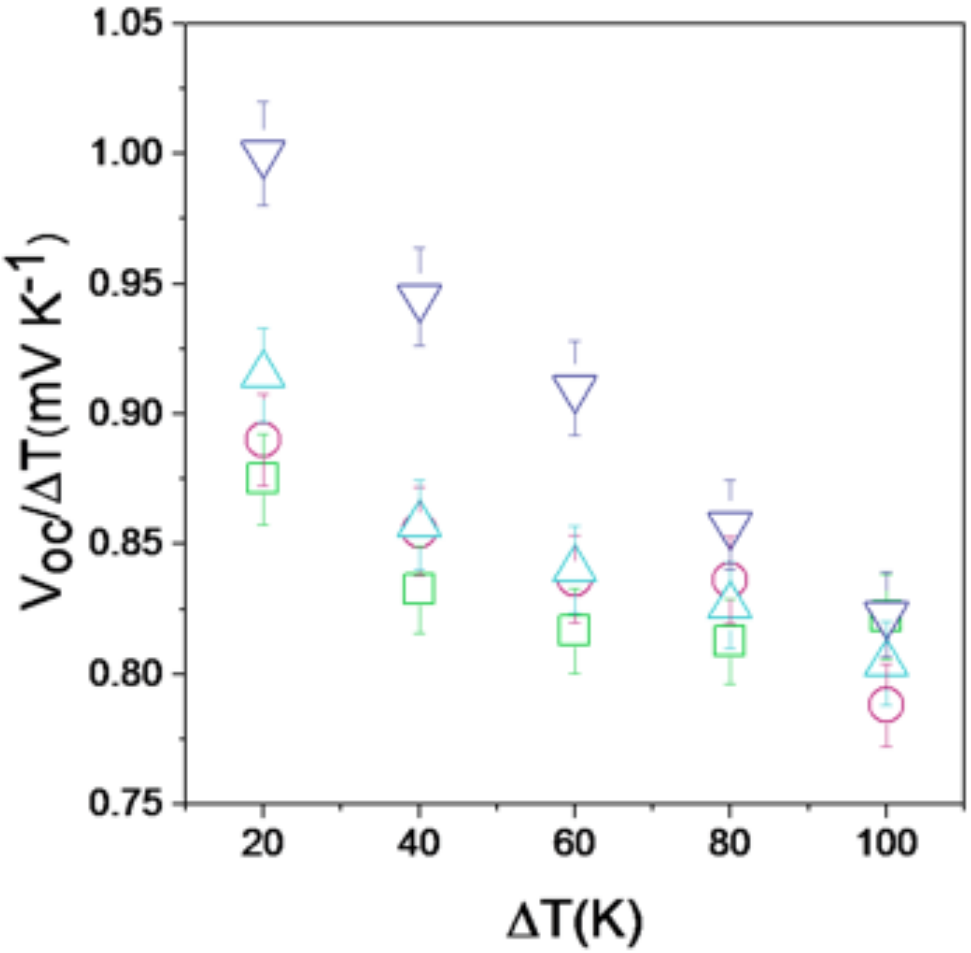

Figure 3.6: T-shaped thermocell performance using 0.4 M $Fe(CN)_6^{3-}$/ $Fe(CN)_6^{4-}$ (green squares), 0.4 M $Fe(CN)_6^{3-}$/ $Fe(CN)_6^{4-}$ + 0.00625 wt% PEDOT:PSS (pink circles), 0.4 M $Fe(CN)_6^{3-}$/ $Fe(CN)_6^{4-}$ + 0.06 wt% PEDOT:PSS + 0.015 wt% MWNT (blue triangles up), 0.4 M $Fe(CN)_6^{3-}$/ $Fe(CN)_6^{4-}$ + 0.005 wt% PEDOT:PSS + 0.015 wt% MWNT (purple triangles down) as a function of different temperature difference (Δ T). ΔT is the temperature difference between hot and cold block. $V_{oc}/\Delta T$ is the ratio of the open circuit voltage and temperature difference.

crease in interfacial charge transfer resistance for 0.025 wt% of MWNT. The increase in ohmic conductivity can be attributed to the addition of ions present in PEDOT:PSS and the interfacial polarization due to dispersed MWNT [43]. For the aqueous electrolyte the wt % of MWNT was as low as 0.025 wt% of total solution to avoid percolation.

MWNTs dispersed in PEDOT:PSS added to an electrolyte increase the interfacial area where dipoles can orient and hence increasing the ohmic conductivity [44]. Once the tem-

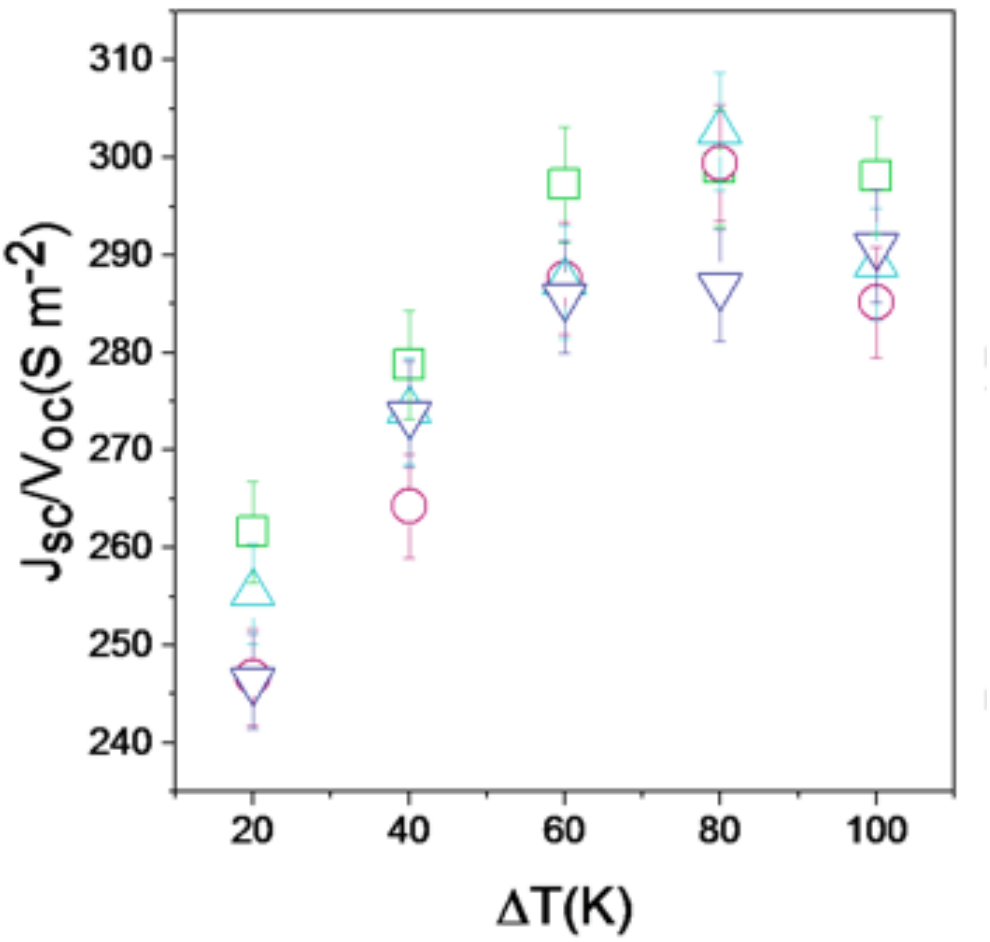

Figure 3.7: T-shaped thermocell performance using 0.4 M $Fe(CN)_6^{3-}$/ $Fe(CN)_6^{4-}$ (green squares), 0.4 M $Fe(CN)_6^{3-}$/ $Fe(CN)_6^{4-}$ + 0.00625 wt% PEDOT:PSS (pink circles), 0.4 M $Fe(CN)_6^{3-}$/ $Fe(CN)_6^{4-}$ + 0.06 wt% PEDOT:PSS + 0.015 wt% MWNT (blue triangles up), 0.4 M $Fe(CN)_6^{3-}$/ $Fe(CN)_6^{4-}$ + 0.005 wt% PEDOT:PSS + 0.015 wt% MWNT (purple triangles down) as a function of different temperature difference (Δ T). ΔT is the temperature difference between hot and cold block. J_{sc}/V_{oc} is the ratio of short current density and open circuit voltage.

perature difference is applied at the electrodes, a potential difference is generated at the electrodes causing ions to migrate and charges on MWNTs to reorient. Reorientation of charges on the MWNT helps in the migration of ions to charged surfaces (interfacial polarization) resulting in increase in ohmic conductivity. The decrease in interfacial charge transfer resistance implies that nanoparticle addition improves contact between the electrode and the electrolyte.

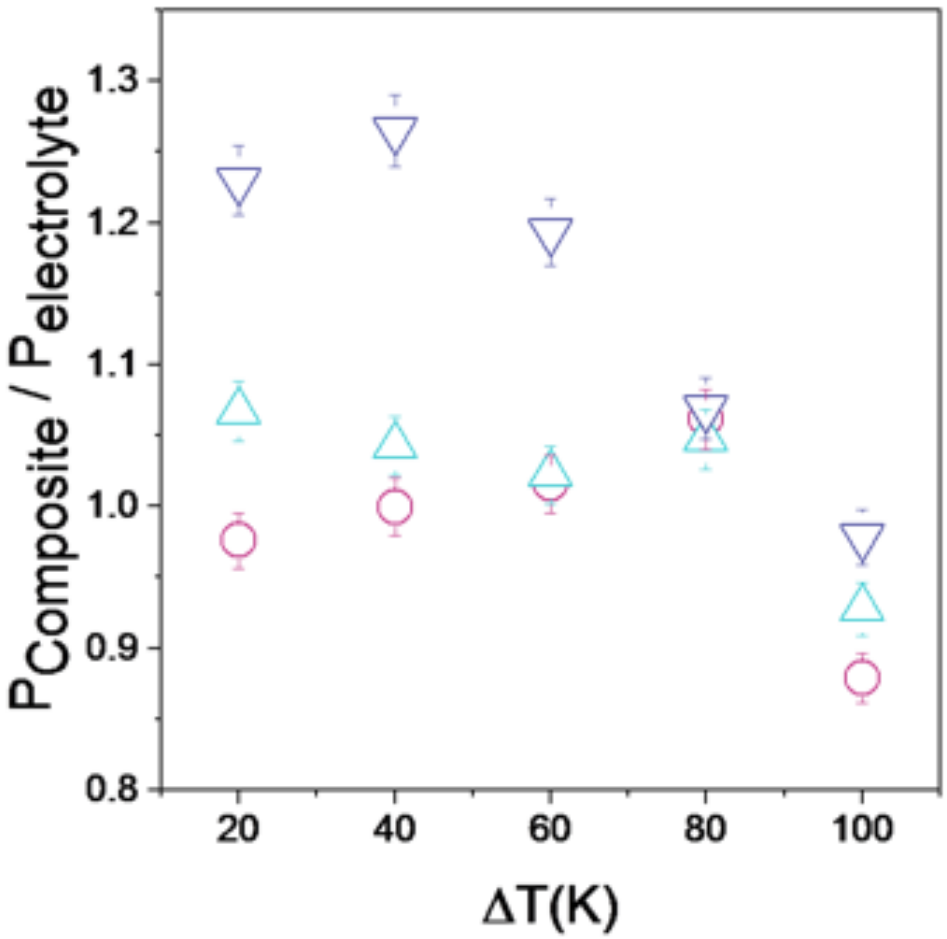

Figure 3.8: T-shaped thermocell performance using 0.4 M $Fe(CN)_6^{3-}$/ $Fe(CN)_6^{4-}$ (green squares), 0.4 M $Fe(CN)_6^{3-}$/ $Fe(CN)_6^{4-}$ + 0.00625 wt% PEDOT:PSS (pink circles), 0.4 M $Fe(CN)_6^{3-}$/ $Fe(CN)_6^{4-}$ + 0.06 wt% PEDOT:PSS + 0.015 wt% MWNT (blue triangles up), 0.4 M $Fe(CN)_6^{3-}$/ $Fe(CN)_6^{4-}$ + 0.005 wt% PEDOT:PSS + 0.015 wt% MWNT (purple triangles down) as a function of different temperature difference (Δ T). ΔT is the temperature difference between hot and cold block. $P_{composite}$ /$P_{electrolyte}$ is the ratio of the maximum power measured with and without the composite.

3.3.2 Cyclic Voltammetry

Temperature dependent cyclic voltammetry was performed on 0.4 M $Fe(CN)_6^{3-}$/ $Fe(CN)_6^{4-}$ (Figure 3.4 and Figure A.3a) and compositions determined in the previous section corresponding to 0.00625 wt% of PEDOT:PSS (Figure 3.1 and Figure A.3b) and Lean, rich mixture corresponding to 0.015 wt% of MWNT (Figure 3.3, Figure A.3c and Figure A.3d). The slope, which corresponds to Se is -1.5 mV/K for all electrolyte types and the corresponding

ΔS is -144.7 J K^{-1} mol^{-1}, which is consistent with literature [37, 67]. Importantly, the downward shift $E_{1/2}$ suggest increase preference of the redox couple towards formation of $Fe(CN)_6^{3-}$ i.e. (the equilibrium move to right in the following equation) in sample having carbon nanotube and polymer composite [113, 118].

$$Fe(CN)_6^{4-} \rightleftharpoons Fe(CN)_6^{3-} + e^- \tag{3.3}$$

This effect is same as having a higher average temperature in the cell because as the temperature is increased $E_{1/2}$ decreases.

3.3.3 T-cell thermocell testing

The performance of thermocells having aqueous composite electrolyte was tested in T-cell thermocell configuration (Figure 3.6, Figure 3.7 and Figure 3.8). The electrolyte composition was based on the enhancement in ohmic conductivity and reduction in interfacial charge transfer resistance after the introduction of polymer and MWNT composite. The temperature difference used in the calculation is the difference in temperatures of the heating and cooling blocks and not the temperature difference at the electrodes. To prevent leakage from cell, the thermocouple could not be placed at the electrodes. The temperature difference of the blocks recorded is higher than what is present at the electrodes due to thermal resistance losses. The higher temperature difference measured at the heating and cooling blocks results in a V_{oc}/ ΔT less than 1.5 mV/K (Figure 3.6), which is the Seebeck coefficient recorded in the previous section. A power performance comparison for electrolyte having a lean (more PEDOT:PSS), rich (less PEDOT:PSS) and no MWNT mixture (only PEDOT:PSS) is compared with that of electrolyte with only 0.4 M $Fe(CN)_6^{3-}$/ $Fe(CN)_6^{4-}$ (Figure 3.8). Each of the particle additions increased the V_{oc}/ΔT compared to pristine electrolyte. (PEDOT:PSS):MWNT 1:3 produced the greatest increase in V_{oc}/ ΔT. This can be attributed to decrease in interfacial charge transfer resistance of the composite,

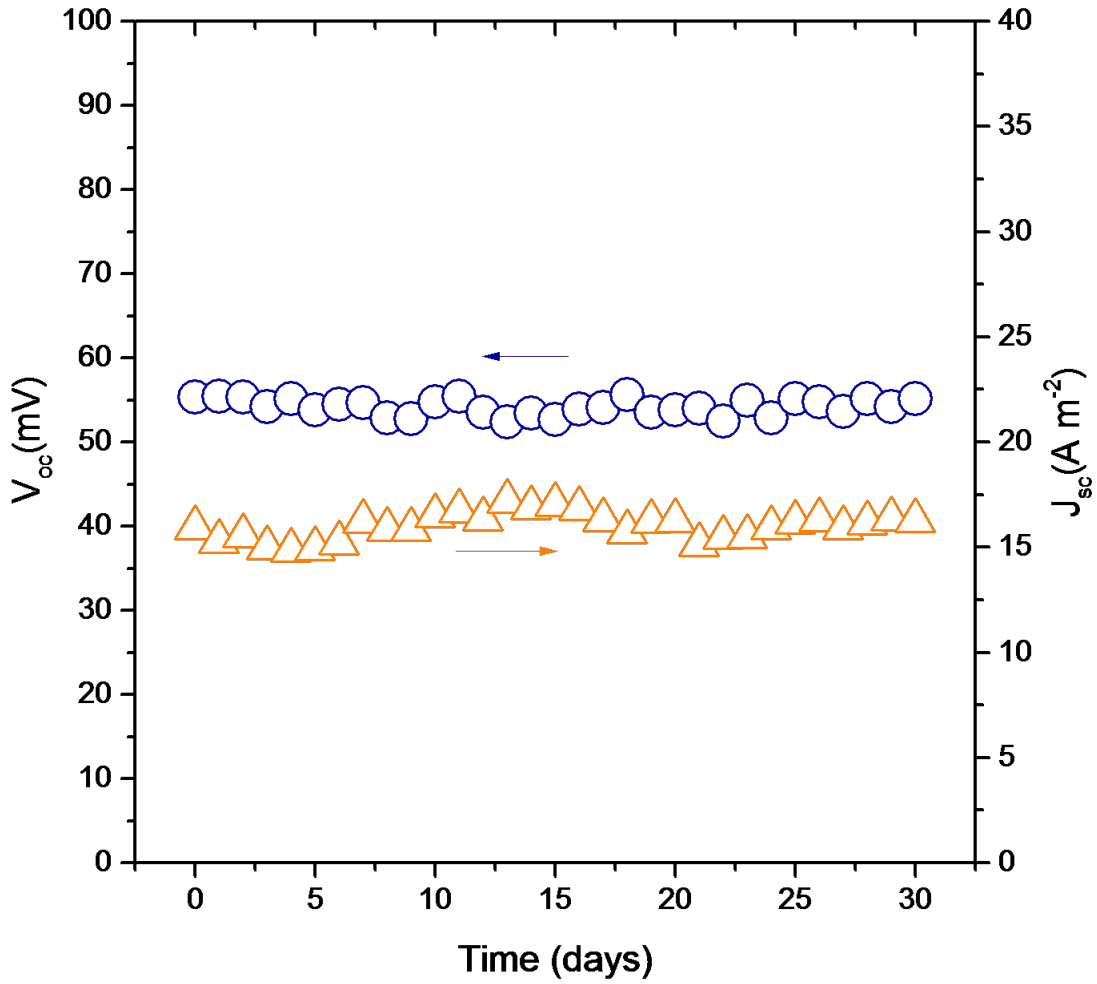

Figure 3.9: Performance of t-shape thermocell with polymer and carbon nanotube composite electrolyte versus time for ΔT approximately 60 K. Electrolyte composition 0.4 M $Fe(CN)_6^{3-}$/ $Fe(CN)_6^{4-}$ + 0.005 wt% PEDOT:PSS + 0.015 wt% MWNT. V_{oc} is the open circuit voltage (blue circle), J_{sc} is the short circuit current per unit cross-sectional area (orange triangle) .

which helps in increasing the V_{oc} [99]. The cell conductance J_{sc}/V_{oc} has a positive slope because the Jsc increase with each increment of ΔT is not matched by a corresponding proportionate increase in V_{oc}. Comparing the lean and rich mixture, the wt% of MWNT was fixed at 0.015 wt% with PEDOT:PSS amount 0.06 wt% and 0.005 wt% respectively. The lower wt% of PEDOT:PSS improves the performance, while increasing the wt% of PEDOT:PSS increases viscosity which counteracts the positive effect of increase in PEDOT:PSS ions as the interfacial charge transfer resistance and ohmic conductivity is same

for both mixtures at 0.015 wt% of MWNT (Figure 3.3). However, for both composites having MWNTs, the power measured is more than without the MWNTs. The overall increase in power output is about 1.30 times greater than without the composite for a ΔT of 40 K for MWNT rich composite. The highest power achieved with composite was 0.5 W/m^2 for a ΔT of 100 K. The overall enhancement in performance is a combination of reduction in interfacial charge transfer resistance, increase in ohmic conductivity and increase in interfacial polarization. To test the stability of the enhancement, V_{oc} and J_{sc} for t-shape thermocell having rich mixture MWNT were measured over a 30 day period (Figure 3.9). The stable performance suggest that polymer and carbon nanotube composite electrolyte can be used for long term operation.

3.4 Conclusions

In this chapter, improvements in the electrochemical properties of the standard 0.4 M $Fe(CN)_6^{3-}$/ $Fe(CN)_6^{4-}$ aqueous electrolyte have been achieved by introducing polymer and carbon nanotube composite, which increases the ohmic conductivity and reduces the interfacial charge transfer resistance. The improvement in performance is observed by a systematic study of the effect of introducing first polymer only in the electrolyte and then introducing polymer: CNT lean (4:1) and rich (1:3) composites. In the absence of chemical functionalization the interaction between CNTs and polymer is through van der Waals forces, this interaction prevents CNT-CNT agglomeration and helps disperse CNTs in the polymer. Lean and rich composite dispersed in electrolyte were tested in t-shape thermocell, with rich CNT composite having the maximum power enhancement. The enhancement is attributed addition in number of ions present in PEDOT:PSS, interfacial polarization and improve contact at the electrode/electrolyte interface.

CHAPTER 4

INCREASE IN FIGURE OF MERIT ZT AND MOLECULAR DYNAMICS SIMULATION OF ELECTRICAL CONDUCTIVITY FOR POTASSIUM FERRI/FERROCYANIDE

The author would like to thank Anh Tran for help with Molecular Dynamic Simulation.

4.1 Introduction

Thermo-electrochemical cells (or thermocells) having potassium ferri/ ferrocyanide as electrolyte is an inexpensive method to recover low grade waste heat. It is observed that the addition of multiwall carbon nanotubes and poly (3,4- ethylenedioxythiophene) poly(styrenesulfonate) in aqueous potassium ferri/ ferrocyanide increase the figure of merit ZT by about 15 %. The increase in ZT is attributed to reduction in thermal conductivity and increase in ohmic conductivity of the new composite electrolyte. Moreover, it has been observed an inverse favorable relationship exists between the two properties for each addition to the electrolyte. In addition, we have carried out molecular dynamics simulation for potassium ferri/ ferrocyanide for the change ohmic conductivity as the concentration of it increases from 0.1M to 0.4M.

Thermocells consist of two main components the electrolyte and the electrode. The electrolyte is sandwiched between two electrodes. When a temperature difference is applied at the electrodes, oxidation and reduction takes place at the respective electrode. Preference to oxidation or reduction depends on temperature at the electrodes. The chemical equilibrium equation for a common redox couple potassium ferri/ferrocyanide ($Fe(CN)_6^{3-}$/ $Fe(CN)_6^{4-}$) is given as

$$Fe(CN)_6^{4-} \rightleftharpoons Fe(CN)_6^{3-} + e^-. \tag{4.1}$$

For potassium ferri/ferrocyanide, at the higher temperature electrode the equilibrium shifts in forward direction and oxidizes (loss of electrons), while at the lower temperature electrode it shifts in the backward direction and reduces (gain of electrons). The higher temperature electrode behaves as an anode and lower temperature electrode behaves as a cathode. The shift in equilibrium is explained by Le Châtelier's principle or "The Equilibrium Law" which states that when any system is subjected to change such as temperature, the systems adjust itself to counterbalance the effect of the applied change. The free energy difference of products and reactants at the electrodes generates the thermo-electrochemical force (also known as an electromotive force, EMF). The resultant ions after being oxidized/reduced at a specific electrode, get transported to opposite electrodes in the thermocell. Meanwhile the electrons generated at the anode, due to the oxidation of ions flow through the external circuit from anode to cathode and consequently get consumed by the ions, reducing them at the opposite electrode. The transport of ions, within the fluid medium of thermocell, is due to electrical or chemical potential between the two electrodes or bulk movement of solution with the respective modes are called migration, diffusion and convection. The transport of ions is one of the main performance limiting steps and is described by property known as ohmic resistance (or its reciprocal ohmic conductivity). Thermal aspects is also very important and is defined by the thermal conductivity of the electrolyte. The coupling of these properties is described by the dimensionless figure of merit ZT,

$$ZT = \frac{\sigma S^2 T}{\lambda} \tag{4.2}$$

where σ is the ohmic conductivity, S is the Seebeck coefficient, T is the temperature and λ is the thermal conductivity. Much of the recent work has focused on improving the Seebeck coefficient by using ionic liquids [31, 89, 124] and using macromolecules [40, 41]. Electrical conductivity has largely remained low. While for the electrode, the use of carbon nanotubes have resulted in increase power output and reduce the cost of thermocells by replacing more traditional Platinum electrodes [47, 50, 66]. The increase in power output

by using carbon nanotube electrodes is attributed to more electroactive surface area and low charge transfer resistance.

Investigations by experiments are often assisted by modeling and simulation tools, because of its predictive modeling capacity. In the context of materials science, these computational tools spans a wide spectrum from continuum to quantum level. At atomic level, density functional theory (DFT) and molecular dynamics (MD) are among the most celebrated tools to capture the chemical reaction, as well as qualitatively calculate the bulk properties of the substance. In MD simulation, the atomic motions are described by the interatomic potential, which in turn can be obtained via density functional theory calculations. At every timestep, pairwise interatomic forces are computed based on the interatomic potentials and the distance of two atoms. These pairwise forces are combined to yield a total force acting on each atom, thus the corresponding velocities are computed. The atomic positions are then updated using a numerical integrator, e.g. Verlet or leapfrog, before the interatomic forces are computed again based on the updated atomic positions. The process repeats over again until the timestep counter is satisfied. MD simulation has been proven successful to measure bulk properties because of its natural periodic boundary condition. To assist the experimental data of ferri/ferrocyanide solutions, the ohmic conductivity calculations are performed using MD simulations. The simulation results are found to be in good agreement with experimental data.Further computational studies will include interfacial behaviors and interactions of PEDOT:PSS, multiwall carbon nanotubes, and ferri/ferrocyanide with a charged platinum surface.

To that end, MD simulations is performed in this study firstly to support the experimental results, and secondly to validate the ferri/ferrocyanide force-field [127] for future studies. Given the multi-scale complexity and challenges of the electrolyte, it is necessary to investigate the electrical properties of the ionic liquid potassium ferri/ferrocyanide and water before MWNT, PEDOT:PSS, and the charged platinum interface are added. The simulated results are found to capture the main trend of increasing electrical conductivity with

respect to increase in concentration, but substantially underestimate the experimental data, more severely at lower concentration.

In this chapter, we observe that the addition of multiwall carbon nanotubes (MWNT) and poly (3,4- ethylenedioxythiophene)poly(styrenesulfonate) (PEDOT:PSS) composite to aqueous $Fe(CN)_6^{3-}$ /$Fe(CN)_6^{4-}$ increases its ZT by about 15 $\%$. This is achieved by decrease in thermal conductivity and increase in ohmic conductivity in the new composite electrolyte. The inverse change in the two properties is desirable for improved ZT and higher efficiency of thermocells. Given the importance of ohmic conductivity of $Fe(CN)_6^{3-}$ /$Fe(CN)_6^{4-}$ for thermocells, we have carried out MD study. The simulation will serve as a platform for further development of the electrolyte.

4.2 Experimental

4.2.1 Material and preparation

Potassium hexacyanoferrate (II) trihydrate (commonly known as potassium ferrocyanide) and Potassium hexacyanoferrate (III) (commonly known as potassium ferricyanide) were purchased from Sigma Aldrich having a molecular weight of 422.39 g/mol and 329.26 g/mol, respectively. PEDOT:PSS was purchased was purchased from Heraeus Clevios. According to product specifications the PEDOT:PSS ratio by weight is 1:2.5 at 20 ^oC, the viscosity is 15-50 mPas, the solid content is 1-1.3 $\%$ and the density is 1 g/cm3. MWNT were purchased from US Research Nanomaterials, Inc. having stock number 4315. According to product specifications, the outside diameter is 50-80 nm, the density is 2.1 g/cm^3, lengths is 10-20 μm and purity is greater than 95 $\%$. Mixture of PEDOT:PSS and $Fe(CN)_6^{3-}$/$Fe(CN)_6^{4-}$ cynaide was made by dispersing the polymer using 30 min of stirring, 30 min of sonication and 15 minute of stirring. Composite of PEDOT:PSS and MWNT was made by dispersing the polymer using 30 min of stirring, 30 min of sonication and 15 minute of stirring. The composite of PEDOT:PSS and MWNT was disperse in $Fe(CN)_6^{3-}$/$Fe(CN)_6^{4-}$ by following aforementioned steps.

4.2.2 Thermal conductivity measurement

Thermal conductivity of aqueous electrolyte were measured with a transient plane source technique using TPS 2500 S. The instrument meet the testing standard (ISO/DIS 22007-2.2) having accuracy better than 5 % and reproducibility of 1 %. Before each measurement, the sensor were calibrate using material of known properties. Stainless steel bar and water was used for calibration. Kapton sensor # 7577 was used for measurement and for each sample 10 measurement were made. The measurement sensor was dipped in about 8 ml of testing liquid. The measurement sensor was positioned such that it was completely surrounded with testing liquid.

4.2.3 Ohmic conductivity measurement

Ohmic conductivity was measured using CH instruments model 660E potentiostat. The procedure used is described in our previous work [70, 43]. To describe briefly, two platinum electrodes were used to measure impedance over a wide frequency range 1MHz-0.02 Hz, DC signal of 0 mV and with an AC amplitude of 20 mV. The measured spectra was fitted with Randles model with high frequency intercept on Nyquist plot corresponding to ohmic resistance. The reciprocal of ohmic resistance corresponds to ohmic conductivity. To obtain the exact value of ohmic conductivity, the system was calibrated to sample known electrical conductivities. Potassium chloride of concentration 0.1M and 1.0M was used for calibration. The electrolyte having composite was tested with electrodes 10 mm apart. No short circuit was observed during the experiments.

4.3 Molecular dynamics simulations

4.3.1 Simulation settings

Table 4.1 shows the geometry settings of the MD simulations performed in this study, as well as the number of atoms, molecules, and ions in the simulation cell. The numbers of

ferricyanide $[Fe(CN)_6]^{3-}$ ions and ferrocyanide ions $[Fe(CN)_6]^{4-}$ are the same for all MD simulations, varying from 6 to 33, depending on the concentration of the electrolyte. The number of water molecules is roughly more than 3,000. The initial geometry of the simulation is created using Moltemplate [125]. The dimension of the cubic simulation cell is $a \times a \times a$ for all simulations, where parameter a is tabulated in the second column of Table 4.1. The dimension a of the simulation cell is carefully tuned to approximate the experimental density for incompressible liquid eletrolytes. SPC/E [126]. water potential is used

Table 4.1: Geometry settings and number of atoms, molecules, and ions of MD simulations.

Conc. (M)	a (Å)	H_2O	K^+	$Fe(CN)_6^{4-}$	$Fe(CN)_6^{3-}$	Density (g/cm^3)
0.1M	46.3574	3330	42	6	6	1.0697
0.2M	45.0339	3053	77	11	11	1.1503
0.3M	46.3574	3330	126	18	18	1.2093
0.4M	45.0339	3053	154	33	22	1.2790

to model the interactions of water molecules. The parametrization of ferri/ferrocyanide force-field is adopted from Table 1 in Prampoloini et al. [127], in which the intramolecular potentials are composed of harmonic stretching, bending, and torsional energies. The intramolecular potential is expressed as

$$\begin{aligned} E^{\text{intra}} &= \tfrac{1}{2}\textstyle\sum_{i=1}^{N_s} K_i^s (r_i - r_i^0)^2 \\ &\quad + \tfrac{1}{2}\textstyle\sum_{i=1}^{N_b} K_i^b (\theta_i - \theta_i^0)^2 \\ &\quad + \tfrac{1}{2}\textstyle\sum_{i=1}^{N_d} K_i^d (\phi_i - \phi_i^0)^2, \end{aligned} \tag{4.3}$$

where $r_i^0, \theta_i^0, \phi_i^0$ are the reference bond length, bending angle, and torsional angle, respectively, and K_i's are the corresponding force constants. Partial charges for Fe, C, and N to model electrostatic force using Coulomb's law is transferred from Prampoloini et al. [127] in Table 2. Figure 4.1 presents the geometry of the ferri/ferrocyanide ions in VMD [128]. Table 4.2 and Table 4.3 list the intramolecular force-field parameters and partial charges that are used in this study, respectively. The interatomic potential functions are described

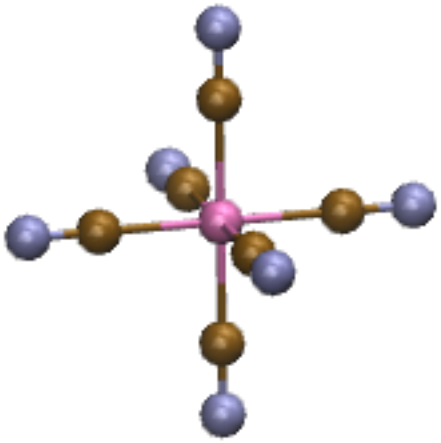

Figure 4.1: Geometry of ferricyanide and ferrocyanide ions. The difference between these ions are the bond lengths and corresponding stretching, bending, and torsional K_i's force constants.Color of atoms shown are Fe (pink), C (green) and N (blue).

by a 12-6 Lennard-Jones (LJ) potential model, and an electrostatic contribution as

$$\begin{aligned} E_{ab}^{\text{inter}} &= \sum_i^{\text{on } a} \sum_j^{\text{on } b} \frac{k_C q_{a_i} q_{b_j}}{r_{a_i} r_{b_j}} \\ &+ \sum_i^{\text{on } a} \sum_j^{\text{on } b} 4\varepsilon_{a_i b_j} \left[\left(\frac{\sigma_{a_i b_j}}{r_{a_i b_j}} \right)^{12} - \left(\frac{\sigma_{a_i b_j}}{r_{a_i b_j}} \right)^{6} \right]. \end{aligned} \tag{4.4}$$

The LJ parameters for Fe^{3+}/Fe^{2+} in $Fe(CN)_6^{3-}$/$Fe(CN)_6^{4-}$ and O in water molecules is taken from Ando [129], whereas the parameters for C and N is excerpted from Martiniano et al. [130]. For K and O, LJ parameters is described in Lee and Rasiah [131]. The remaining potentials are approximated using geometric mixing rule, $\sigma_{ij} = \sqrt{\sigma_i \sigma_j}$ and $\varepsilon_{ij} = \sqrt{\varepsilon_i \varepsilon_j}$. The simulation is performed using LAMMPS packages [132]. Short range force is neglected if the interatomic distance between two atoms exceed the cutoff radius, whereas the long range force is evaluated using PPPM method [133]. The geometry of water molecules is constrained by SHAKE algorithm [134] throughout the simulation. Figure 4.2 presents a snapshot of MD simulation in this study using VMD.

Table 4.2: Bonded intramolecular force-field parameters in ferri/ferrocyanide ions [127].

	$[Fe(CN)_6]^{3-}$		$[Fe(CN)_6]^{4-}$	
bond	K^s (kcal/mol Å^{-2}	r_0) (Å)	K^s (kcal/mol Å^{-2})	r_0 (Å)
Fe-C	155.2344	1.997	82.6244	2.035
C-N	2572.6606	1.176	2379.2091	1.186
angle	K^b (kcal/mol rad^{-2})	θ_0 (deg)	K^b (kcal/mol rad^{-2})	θ_0 (deg)
Fe-C-N	41.3241	180	46.9886	180
C-Fe-C	195.7220	90/180	231.9553	90/180
coplanar dihedral	K^d (kcal/mol rad^{-2})	ϕ_0 (deg)	K^d (kcal/mol rad^{-2})	ϕ_0 (deg)
C-C-C-C	84.7037	0	108.6999	0
N-N-N-N	84.7037	0	108.6999	0

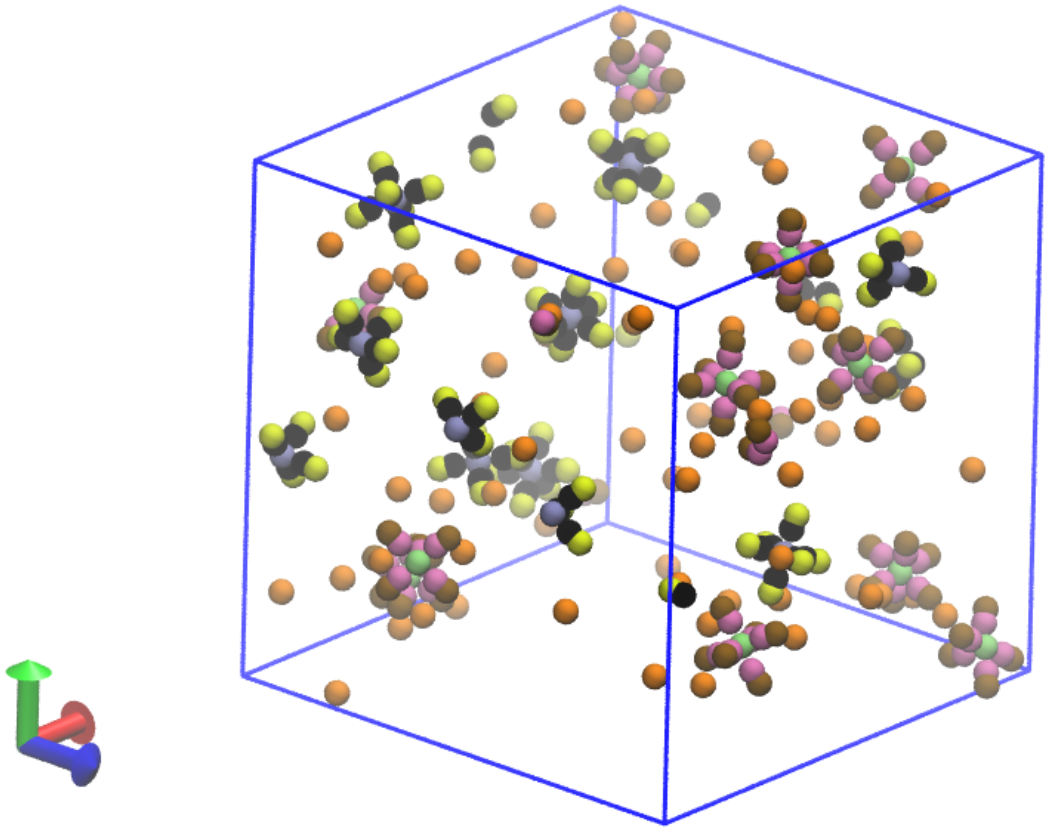

Figure 4.2: Snapshot of MD simulation excluding water molecules. (Color iceblue, black, and yellow atoms correspond to Fe^{3+},C,N in ferricyanide ions. whereas lime, mauve, and ochre atoms correspond to Fe^{2+},C,N in ferrocyanide ions. The scattering orange atoms represents K^+ counterions.)

Table 4.3: Partial charges of atoms in ferro/ferricyanide ions [127].

atom	$[Fe(CN)_6]^{3-}$	$[Fe(CN)_6]^{4-}$
Fe	-0.834	-1.150
C	+0.403	+0.431
N	-0.763	-0.906

4.3.2 Ohmic conductivity

The ohmic conductivity is proportional to the asymptotic slope of total sum of net displacement for all ions within the solution. The equation of thermal conductivity was adopted from Levesque et al. [135] as

$$\sigma = \frac{e^2}{6Vk_BT} \lim_{t\to\infty} \partial_t \left\langle \left| \sum_{\alpha}^{N_\alpha} q_\alpha \Delta_\alpha(t) \right|^2 \right\rangle, \tag{4.5}$$

where k_B is the Boltzmann constant, e is the elementary charge, V is the volume of the simulation cell, $\Delta_\alpha(t) = \sum_{i\in\alpha} \delta r_i(t)$ is the net displacement of all the ions of species α and charge q_α in time t. Before the simulation, an equilibration phase is carried out with NVE ensemble and Langevin thermostat at 300K for 90 ps. The simulation is then run for 1.50ns in NVT ensemble using the timestep of 0.5 fs. In this simulation study, two concentration of ferri/ferrocynaide are performed: 0.2M and 0.4M. For 0.2M solution, the number of ferri/ferrocynaide molecules are both 11, and the number of K^+ counterions are 77. For 0.4M concentration, the number of $Fe(CN)_6^{3-}$ and $Fe(CN)_6^{4-}$ molecules are both 22, and the number of K^+ counterions is 154. The simulation volume is held constant during the simulation to model the incompressible liquid.

Due to the big size of $Fe(CN)_6^{3-}$/$Fe(CN)_6^{4-}$ ions inside the simulation cell, it is expected that Equation 4.5 converges slowly. To cope with the expensive computation, we compute numerically the first derivative of the ensemble average quantity $Q = \left\langle \left| \sum_{\alpha}^{N_\alpha} q_\alpha \Delta_\alpha(t) \right|^2 \right\rangle$. The first numerical derivative is then smoothed out using moving average of the time window of 100ps. Finally, the smoothed average quantity is then fitted to a bounded expo-

nential model $f(t) = a_0 e^{-a_1 t} + a_2$, with constraints $a_1 > 0, a_2 > 0, a_0 + a_2 > 0$, subject to nonlinear least square formulation. As $t \to \infty$, the ohmic conductivity converges asymptotically to a_2. After units conversion, the ohmic conductivity is found to be $\lim_{t\to\infty} \sigma_{0.1\mathrm{M}} = 2.4979\ Sm^{-1}$, $\lim_{t\to\infty} \sigma_{0.2\mathrm{M}} = 8.0080\ Sm^{-1}$, $\lim_{t\to\infty} \sigma_{0.3\mathrm{M}} = 9.5749\ Sm^{-1}$, $\lim_{t\to\infty} \sigma_{0.4\mathrm{M}} = 13.8322\ Sm^{-1}$. The MD simulation results are shown and compared with the experimental results in Figure 4.3.

4.4 Result and Discussion

In the previous chapter, we demonstrated that introduction of MWNT and PEDOT:PSS results in increase in ohmic conductivity and reduction in interfacial charge transfer resistance [70]. The composition of MWNT and PEDOT:PSS having maximum ohmic conductivity from previous chapter were selected to measure there thermal conductivity. For S standard value ranges from -1.4 to -1.6 mV/K, as it primarily depends on the concentration of redox couple. But for $Fe(CN)_6^{3-}$/$Fe(CN)_6^{4-}$ concentrations above 0.1 M, the S remains fairly constant [51]. For the present chapter, a conservative value of S equals to -1.4 mV/K was used for calculation. ZT value was calculated for the maximum operating temperature of 373.15 K. Figure 4.3 shows experimental change in thermal, ohmic conductivities and ZT value for $Fe(CN)_6^{3-}$/$Fe(CN)_6^{4-}$ as function of concentration.

The thermal conductivity decreases with each addition of solute to the solvent, as addition of solute impedes heat transport by the solvent. The maximum decrease in thermal conductivity is observed for the composite having higher ratio of MWNT as compared to PEDOT:PSS. Thermal conductivity decrease by about 5 % for MWNT rich composite. The reduction in thermal conductivity helps to maintain a higher temperature difference between electrode and increases thermocell power [136]. The ohmic conductivity increases with increased concentration of ions present in PEDOT:PSS, as more charge particles are available to provide electrical conductance. The addition of MWNT also increase ohmic conductivity due to interfacial polarization. MWNT are polarized when an electric field

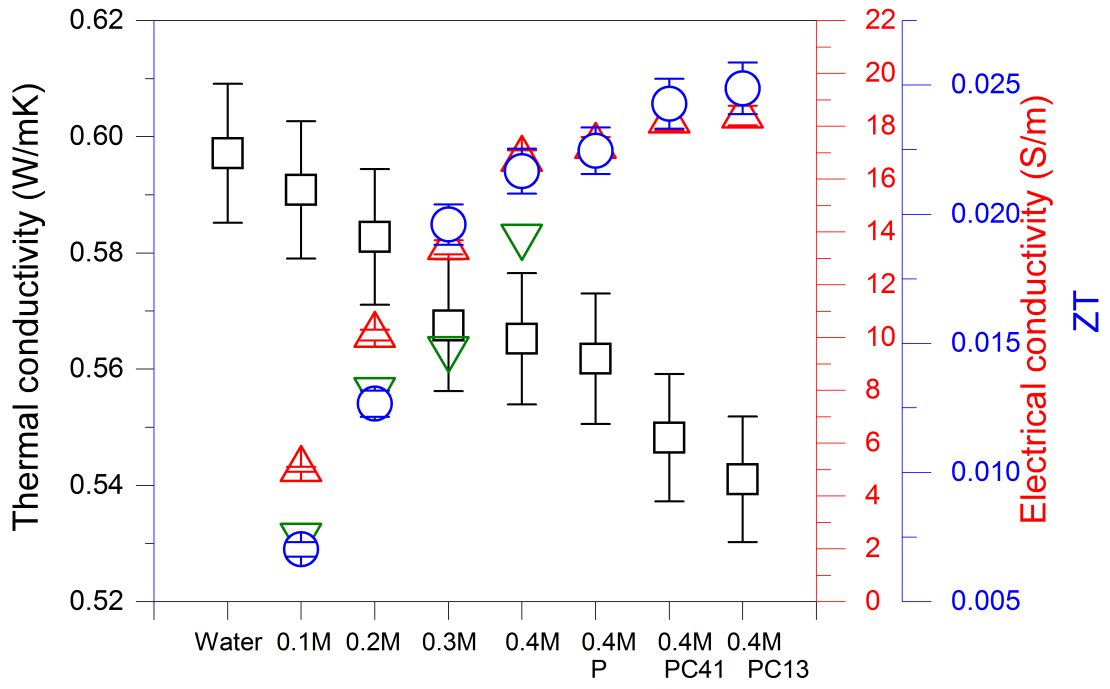

Figure 4.3: Thermal conductivity (black squares), ohmic conductivity (red triangles), MD simulated ohmic conductivity (green triangles down) and ZT (blue circles) for Water, 0.2 M $Fe(CN)_6^{3-}$/ $Fe(CN)_6^{4-}$ (0.2 M),0.4 M $Fe(CN)_6^{3-}$/ $Fe(CN)_6^{4-}$(0.4 M),0.4 M $Fe(CN)_6^{3-}$/ $Fe(CN)_6^{4-}$+PEDOT:PSS 0.0025 wt% (0.4M P),0.4 M $Fe(CN)_6^{3-}$/ $Fe(CN)_6^{4-}$+PEDOT:PSS 0.005 wt% +MWNT 0.00125 wt%(0.4M PC41),0.4 M $Fe(CN)_6^{3-}$/ $Fe(CN)_6^{4-}$+PEDOT:PSS 0.00125 wt% +MWNT 0.00375 wt% (0.4M PC13).

is applied, this can aid in the mass transport of ions. The increase of ohmic conductivity is about 10 % for MWNT rich composite. Hence, a favorable inverse relationship exists between electrical and thermal properties, leading to 15% increase in ZT value for the 0.4 M $Fe(CN)_6^{3-}$/$Fe(CN)_6^{4-}$.

The MD simulation results capture the trend of increasing ohmic conductivity with respect to increasing concentration, but underestimate the experimental data from 17.41% to 50.10% in terms of relative errors, more severely at the 0.1M concentration. There are three important factors that are sensitive to the simulated results. Firstly, the force-field parameters are well-known to be one of the dominant sources of uncertainty in MD simulation. While the force-field parameters are always calibrated to minimize the error within each pair of atoms, the number of pairs scales as $\mathcal{O}(n^2)$, where n is the number of atoms,

and thus the uncertainty is magnified. Secondly, for relatively large ions and molecules, such as ferri/ferrocyanide ions, the finite-size effect requires MD simulations to be ran sufficiently long and the simulation cell to be sufficiently large to mitigate the possible effects on the results. However, MD simulations are known to be limited within time scale (fs to ns) and length scale (nm to μm), particularly when there are covalent and hydrogen bonds with high vibrational frequency within the system, which leads to a decrease in MD time-step. Ideally, the finite-size effect can be mitigated using large-scale MD simulation, but in practice, it is often compromised due to constraints of computational resources. Thirdly, because of the second factor, an analytical model is developed to predict the asymptotic behavior of the quantity of interest when $t \to \infty$, this model also introduces another form of uncertainty in addition to the MD simulation. As such, it is helpful to understand the limitations of MD simulation when comparing with the experimental results. The modeling and simulation complexity of the electrolytes lies in the short time-scale of redox reaction (fs) and the long time-scale (ns) and length-scale (μm) of polymers and MWNT. While each substance has been studied fairly well using either *ab initio*, Born–Oppenheimer, or classical MD simulations, it is challenging to model the mixture due to the computational tractability. In this study, the electrical conductivity of ferri/ferrocyanide and water solution is attempted using MD simulation to investigate the application of ferri/ferro cyanide force-field from Prampolini et al. [127], before other substances are added. The simulation results are validated by comparison with the experimental data. The complex interactions between ferri/ferrocyanide, MWNT, PEDOT:PSS, and the charged platinum surface in the current study remain as an open question for future research.

4.5 Conclusion

It has been shown that the addition of MWNT and PEDOT:PSS, decreases the thermal conductivity and increases the electrical conductivity of aqueous $Fe(CN)_6^{3-}$/$Fe(CN)_6^{4-}$. As a consequence of this favorable reciprocal change in properties, the ZT increases by about 15

%. MD simulations are performed to support the experimental data. The electrical conductivity of the ionic solution of ferri/ferrocyanide as a function of concentration is assessed using LAMMPS package with a slight modification. The bulk electrical conductivity is then quantified using an analytical fitted model from the transient data, subjected to least square error using nonlinear optimization method. The simulated results capture the trend of increasing electrical conductivity with respect to increasing concentration and are found to underestimate experimental data, yet still capture the main trend of increasing electrical conductivity with respect to increase in concentration. Classical MD simulations can offer some important computational insights at the quantum-atomistic level to capture the complicated relationship of thermoelectric transport in the currently developed electrolyte, where the physical limitation of experiments cannot reach.

CHAPTER 5
THERMO-ELECTROCHEMICAL GENERATOR: ENERGY HARVESTING & THERMOREGULATION FOR LIQUID COOLING APPLICATIONS

5.1 Introduction

Managing big data is a thermodynamics problem; decreasing size and increasing performance of electronic devices necessitate the use of liquid cooling to dissipate massive amounts of heat that is generated as a result. In locations such as data centers, CPU cooling is accomplished through the use of air and liquid methods. Currently, the purpose of existing liquid cooling designs is to provide cooling to these high power CPU's. A modified liquid cooling design system that supplements current cooling architecture with the ability to harvest energy from the waste-heat emitted from these heat sources has been tested and validated. An electrolyte capable of undergoing a reversible redox reaction is pumped through a macro-channel flow thermo-electrochemical (thermocell). The heat energy flow is coupled with electrical energy through the thermoelectic effect allowing cooling and power harvesting to occur in parallel. Our current design generated 88 μW of power, achieved a heat transfer coefficient of 450 $W/(m^2.K)$. This technology can be employed in any location where liquid cooling is used, from CPU's in data centers to battery packs in electric vehicles. By providing cooling and energy harvesting these applications will benefit from energy conversion and recycling.

The focus of present work is to harvest waste heat from data centers through using flowing thermo-electrochemical cell. The use of thermo-electrochemical cell can help monitor temperature throughout the cooling system and energy harvested in process can be used to relay this information to monitoring client. The work will enable thermocouple-less and battery-less thermal management monitoring safety system for data centers. The

United States is home to numerous data centers, large and small, boasting up to 12 million servers which consume, at an annual rate of 91 billion kWh [139]. This is enough to power all of the homes in New York City for a two years. It is projected that by 2020, that number could increase to 140 billion kilowatt-hours annually. Keeping these data centers cool is no simple tasks; with power densities of up to 578.7 kW/m^2 and expelled heat of $< 230°$C, the wasted heat that must be removed consumes massive amounts of electricity. In data centers, locations where many computing devices are stored and ran, resulting in high operating temperatures and the need for effective cooling technologies. Nowadays, half of the energy consumed in data centers is used to provide cooling in order to operate current infrastructure in a manner that avoids catastrophic electrical component failure. In an attempt to alleviate the low efficiencies of cooling technologies, liquid cooling has emerged as a viable method [140, 141, 142]. The need for liquid cooling is ever present if we are to keep up with Moore's law. The demand for cooling and energy harvesting technologies is likely to increase, hence, methods to improve thermal management and increase power production will help reduce our carbon. footprint [143][144].

In an effort to maximize the voltage output and to overcome the material constraints, cost-effectiveness, and reliability of current thermoelectric cells, new attempts have been made to produce improved alternatives that focus on higher Seebeck coefficients.

5.1.1 Thermo-electrochemical Cells

One such, novel alternative is an inexpensive liquid-based *thermo-electrochemical cell* (thermocell) that takes advantage of the temperature dependence of electrochemical redox potentials to transfer electrons, Figure 5.1, and produce electric power. This is due to the high Seebeck coefficient of the following reversible redox chemical reaction:

$$Fe(CN)_6^{3-} + e^- \rightleftharpoons Fe(CN)_6^{4-} \tag{5.1}$$

Ferricyanide Fe(III), binded to a CN^- ligand, gets reduced in a half reaction at the first electrode. It is a d^5 system with 5 electrons in the d-orbital. The Fe(III) ion receives an electron into its t_{2g} d-orbital to become ferrocyanide, Fe(II). This is a favorable galvanic cell reaction, because the reaction is spontaneous in the forward direction, i.e. its Gibbs free energy ΔG is negative in the forward direction.

Now we must consider the oxidation half reaction of Fe(II) back to Fe(III), where an electron is liberated from the t_{2g} d-orbital and transferred to the external circuit.

$$\mathrm{Fe}^{3+} + \mathrm{e}^- \rightleftharpoons \mathrm{Fe}^{2+}, E_0 = 0.771 \text{ V} \tag{5.2}$$

This forward reaction is favorable, because the redox potential is positive and as a result the reaction is spontaneous in the forward direction, i.e. its Gibbs free energy ΔG is negative in the forward direction. This is shown as follows:

$$E_f^0 > 0 \tag{5.3}$$

$$\Delta G^o = -nFE_f^0 < 0 \tag{5.4}$$

$$= -74.39 \text{ kJ/mol} \tag{5.5}$$

The backward reaction is not favorable under standard conditions since the backwards reaction has a negative reduction potential, $E_b^0 < 0$. This implies that the reaction is not spontaneous in the backward direction, $\Delta G > 0$. But the reaction we are studying is not under standard conditions. If we were to heat up the oxidation half reaction, by raising the temperature of the fluid, then we would be changing the Gibbs Free energy:

$$\Delta G = \Delta H - T\Delta S. \tag{5.6}$$

In fact we can raise the temperature just enough to thermally regenerate Fe(III) from Fe(II), by making the backwards reaction spontaneous, i.e. making $\Delta G < 0$. This allows us to

continually oxidize and reduce the Fe ions within the fluid, allowing for continual transport and flow of electrons. The Nernst equation assists us in quantifying this effect by which the temperature difference for the half reactions affects the thermocell voltage potential.

$$E - E^{\circ} = (T - T^{\circ})\Delta S^{\circ}_{rx} - \frac{RT}{nF} \ln\left(\frac{C_r}{C_o}\right), \tag{5.7}$$

where the entropy and enthalpy of the reaction are assumed to be constant, and the concentrations of the reducing and oxidizing agent are equal, $C_r = C_o$. From eq. 5.7 we can calculate the open circuit voltage we expect to see for a thermocell under a prescribed temperature difference between two electrodes,

$$V_{oc} = E_c - E_a = \frac{\Delta S^{\circ}_{rx}(T_c - T_a)}{nF}. \tag{5.8}$$

As seen, in order to maximize the voltage output we either increase the temperature difference between the anode and the cathode or select a material with a higher Seebeck coefficient

$$S_e = \frac{\Delta S^{\circ}_{rx}}{nF} \tag{5.9}$$

For our testing we chose a material, in this case an equimolar aqueous solution of ferri/ferrocyanide, with a high Seebeck Coefficient of $\sim$ 1.4-1.6 mV/K [85, 32, 150]. This resulted in a high open circuit voltage. Power generation requires a high voltage and current output. To achieve the latter the use of expensive metals such as Platinum, as an electrode material, was previously required. This was the case until recently, when MWNT electrodes were introduced [47]. MCNTs have been shown to be an inexpensive substitute to other expensive metals for their use as electrodes in thermocells and reported high power conversion efficiencies 1.4 % of the Carnot efficiency.[49, 50, 67] The use of carbon nanotubes has helped researchers look beyond the cost of thermocell development and has focused researchers on performance parameters [33, 43, 48, 51, 52, 53, 70, 151] and prac-

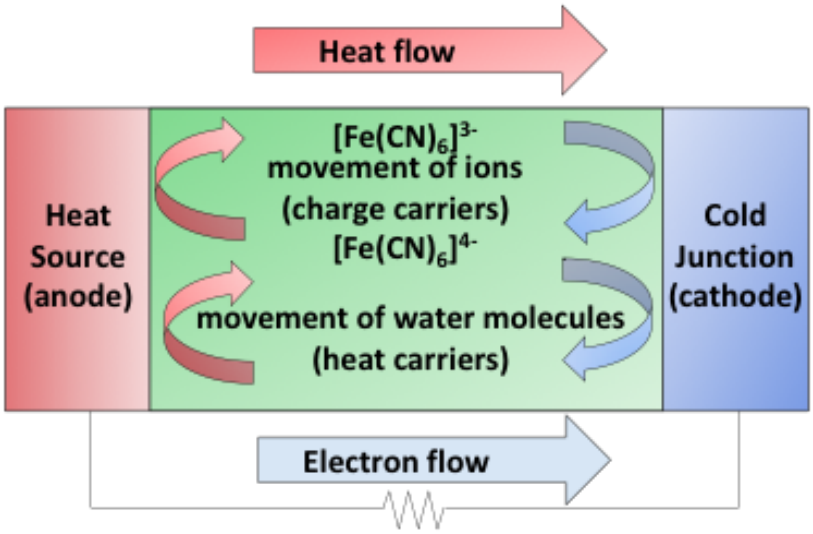

Figure 5.1: A canonical example of oxidations/reduction at hot and cold anode and cathodes for a stationary thermocell.

tical applications [54, 55, 56]. The problem, however, is low current generation due to high mass transfer resistances, minimal electrode surface reaction sites, and no coupling of the flow of the reversible redox couple with convective heat transfer.

Our research focused on reducing these mass transfer resistances by designing and testing a *flow thermocell* where redox ions are driven from one electrode to another, Figure 5.2. This cell combines the power generation capabilities of a stationary thermocell with the forced convection ability of liquid cooling; it was shown to be a viable alternative to cooling high heat flux devices while concurrently generating power.

To understand current output, we must think of electron fluxes at the electrodes (both anode and cathode) where there is a buildup of a current density. These current densities are determined by the kinetics of the chemical reactions at the electrode i, $i \in \{\text{anode}, \text{cathode}\}$ given by the Butler-Volmer equation:

$$j = nFk^o exp\Big[\frac{E}{R}(\frac{1}{T^o} - \frac{1}{T})\Big]\Big[C_O exp\Big(\frac{-nF(1-\beta)\xi}{RT}\Big) - C_R exp\Big(\frac{nF\beta\xi}{RT}\Big)\Big] \tag{5.10}$$

As mentioned previously, mass flow of the electrolyte is beneficial, as it would aid

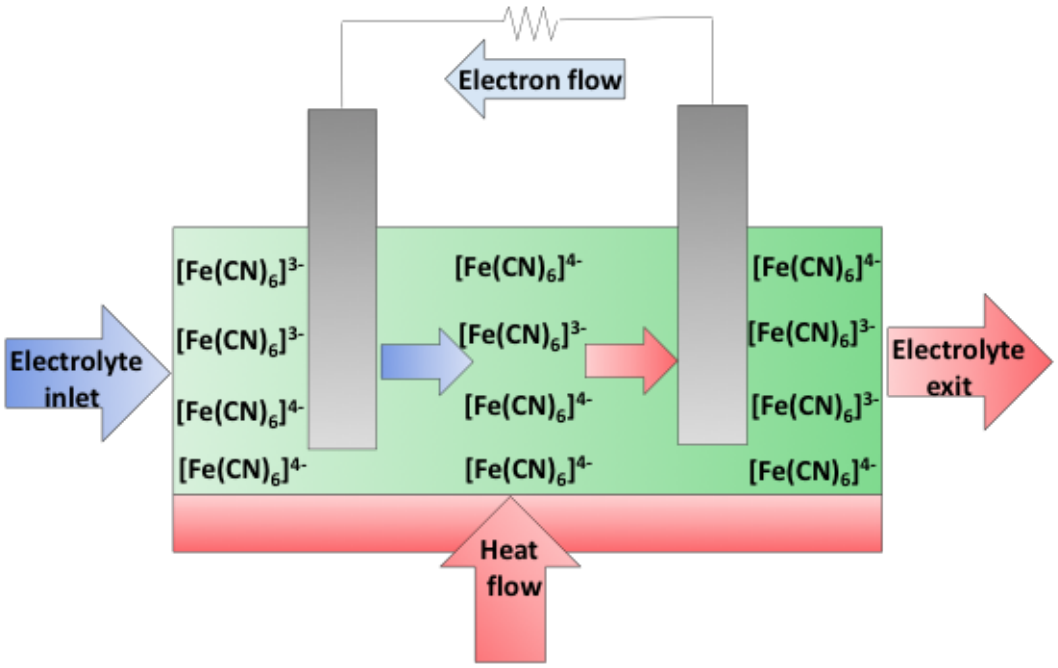

Figure 5.2: A canonical example of oxidations/reduction at hot and cold anode and cathodes for a flowing thermocell.

in movement of ions. For a typical thermocell, ion transport from the anode to the cathode is restricted to diffusion and migration. However, in the *flow thermocell* the convection of the electrolyte will replenish and remove any already oxidized or reduced ion species at the electrode surface. Unidirectional flow would restrict movement of ions backwards and would reduce one of the performance-limiting steps in thermocells, that of ion transport, to and from electrode surfaces.

One of the biggest merits of thermocells is the decoupling of the working fluid's electrical and thermal conductivity, where ions dictate the electrical conductivity and the solvent influences the thermal properties. Despite recent progress, a suitable application that combines the aforementioned merits and that minimizes the limitations of thermocells, has yet to surface. As such we have developed a technique that removes wasted low-grade thermal energy from a system while also utilizing that wasted thermal energy as a driver for producing usable electric energy.

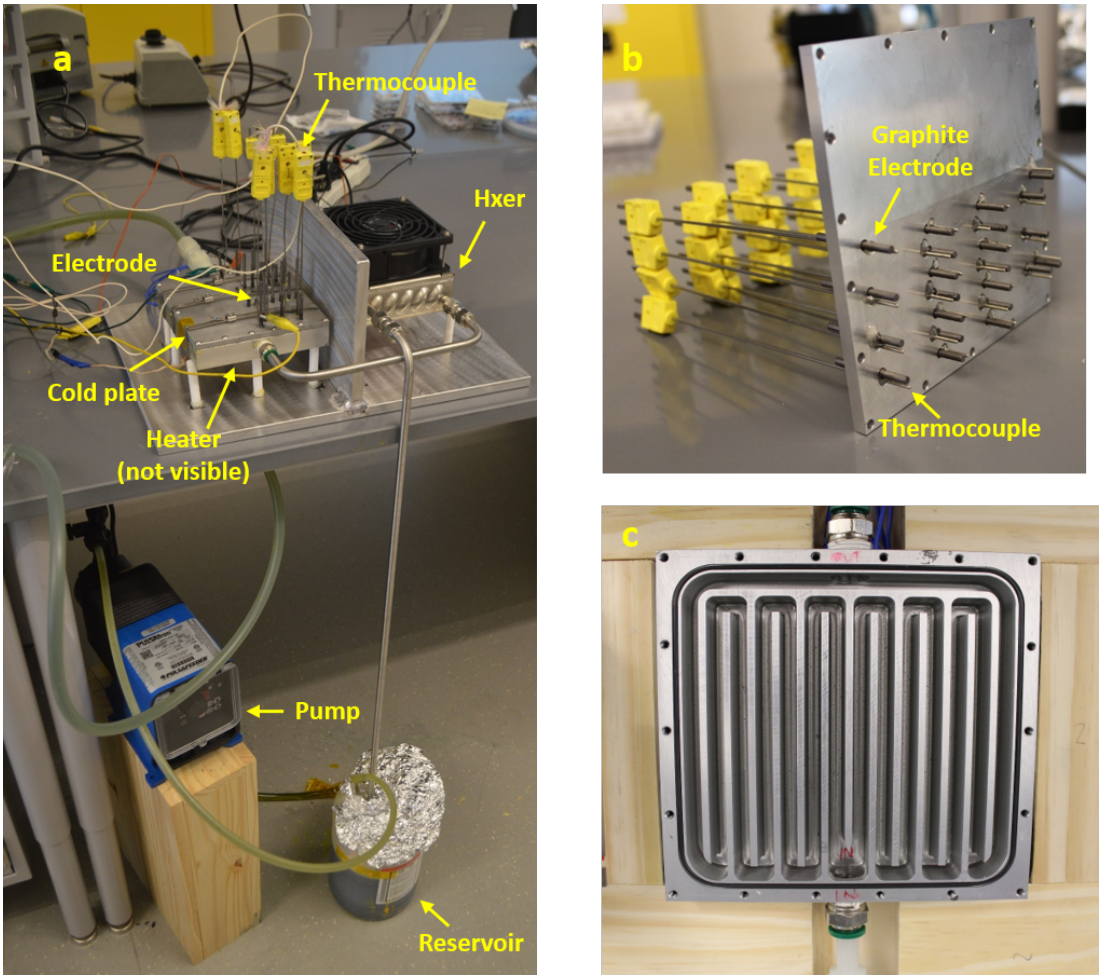

Figure 5.3: Hybrid cold plate (a) complete experimental setup (b) top plate showing electrode and thermocouple position (c) bottom plate showing paths of electrolyte.

5.2 Experimental Design

Physical thermocell was designed and fabricated and numerous experiments were outlined that validated its use as a heat sink and energy harvester. This device was realized by making two design modifications to existing liquid cooling architecture. The first modification that we made was to exchange the working fluid for an aqueous solution of a reversible redox couple whose job is to transfer electrons at electrodes by undergoing a temperature driven chemical reaction. The second modification we made was to insert electrodes into the flow path of the working fluid; they act as locations where the working fluid can chemically interact and transfer electrons. Through these two modifications, we were able to test

voltage, current, and power outputs for a given flow rate and heat flux inward in order to determine the thermocell's ability to convect heat and generate electricity.

5.3 Materials preparation

The solution of potassium ferri/ferro cyanide was made using Potassium ferricyanide (III) and Potassium hexacyanoferrate (II) trihydrate were purchased from Sigma Aldrich having a molecular weight of 329.264 g/mol and 422.39 g/mol, respectively. High volume of about 5000 ml was prepared. Due to high volume the concentration was increased in increments to ensure complete solubility.

Fine extruded graphite rod having diameter 0.125" was purchase from Graphtek LLC. According to product specifications the particle size is 0.02032 cm, density is 1.76 g/cm^3, thermal conductivity is 65 $W/(m.K)$, felxure strength is 34.5 MPa and compressive strength 66.2 MPa. Heat shrink tubing of dia. was used to isolate graphite electrode from the cold plate to prevent short circuit.

The main parameters of interest in the system are the temperature of the fluid at the electrodes, and the voltage/current output at the electrodes for a given electrode position. To collect electrolyte temperature, in-line K-type thermocouples were utilized at the electrode locations. Open circuit voltage and short-circuit current was recorded for 5 minutes using CH instruments model 660E potentiostat. Average value of the measurement over this time interval was taken for further study.Electric resistance heater were used to maintain the bottom plate temperature constant. When temperature drops below the setting temperature, heater is turned ON. When the set temperature is attained heaters turned OFF, however of the bottom plate keeps rising few degrees above setting temperatures. This cycle of maintaining a temperature at a set temperature typically took around 2.5 minutes. The voltage as expected changed proportional to set temperature cycle. So in order to capture the complete temperature (voltage) cycle V_{oc} and I_{sc} were measured for 5 minutes. The measurements were repeated at least three times.

5.4 Results

Reversible redox couple was pumped through a macro-channel heat exchanger that was held at a constant temperature boundary condition. The higher the temperature gradient that developed in flow direction, between electrodes, the more reduction and oxidation of the working fluid will take place, resulting in a higher voltage output.

This thermal/electrochemical coupling arises by the forced convection the fluid; it functions: (i) to remove heat from the system by convective heat transfer and (ii) to assist in the migration of charge from electrode to electrode. Flow-rate effect on the thermal and electrodynamics of the system was considered. It was found that a lower flow rate will produce a larger path-wise temperature gradient, resulting in a higher electrical output between two path-wise electrodes. Consequently the heat transferred from the system will be decreased due to a lower convective heat transfer coefficient. A higher flow rate, however, will increase the amount of heat transferred from the system, but will decrease the temperature gradient between electrodes, thus decreasing the electrical output. In this section we discuss results of our simulations and experiments and perform a comparison of the two.

5.4.1 Simulations

In order to corroborate our experimental results, we performed multi-physics simulations with COMSOL. The thermal and electrodynamic components of the simulation utilized parameters that were consistent with our experimental set up: an aqueous solution of potassium ferri/ferrocyanide with given channel dimensions [151]. It is important to note that the working fluid is primarily water and that the addition of the ferri/ferrocyanide salts, at 0.4M concentration, do not result in a perceivable change to the boiling point of the fluid. Given that our Seebeck coefficient is $S = 1.4$ [mv/K], and that the maximum temperature of our fluid (prior to entering a phase change to gas) is $T_{max} = 373$ K with the fluid at room temperature being $T_{in} = 293$ K, then the maximum realizable voltage output has to be be-

low $V_{max} = 0.11$ V to avoid boiling. To show this, we plotted the temperature and velocity distribution of the fluid is shown in Figure 5.4b. The boundary condition for simulation are same as what were used in experiment:

- Average inlet velocity of 28.16 GPD
- No slip condition at the top and bottom surface of the channel
- Temperature at the bottom surface of the flow channel is 150 ^{o}C.
- The top surface is assumed to be adiabatic.
- The inlet temperature of the fluid is 20 ^{o}C.
- No ion flux through the top and bottom surfaces.
- Electrical insulation boundary condition applied to the top and bottom surfaces.

COMSOL Multiphysics model was developed using heat and mass transfer, Butler-volmer, Nernst-planck and Navier stokes equations. The results for the COMSOL simulation for bottom plate at constant temperature boundary condition are shown in Figure 5.4.

The temperature profile of the electrolyte is shown in Figure 5.4a. Temperature profile shows that convective fluid is effective in maintaining a high temperature difference. The velocity profile is shown in Figure 5.4b, shows that the maximum velocity is near the center line and that no-slip boundary condition is at the surface of top and bottom plate. The power performance is given by Figure 5.4c and Figure 5.4d. As expected a linear relationship exists between voltage and current. The maximum power corresponds to half open circuit voltage, this is where the internal resistance of thermocell equals the external resistance. As the voltage and resistances are equal, the corresponding current is equal as well and the maximum power is given by equation Equation 5.11.

Our simulations provided telling results as to the efficacy of the thermocell. The temperature and velocity distribution of the working fluid, given a constant temperature

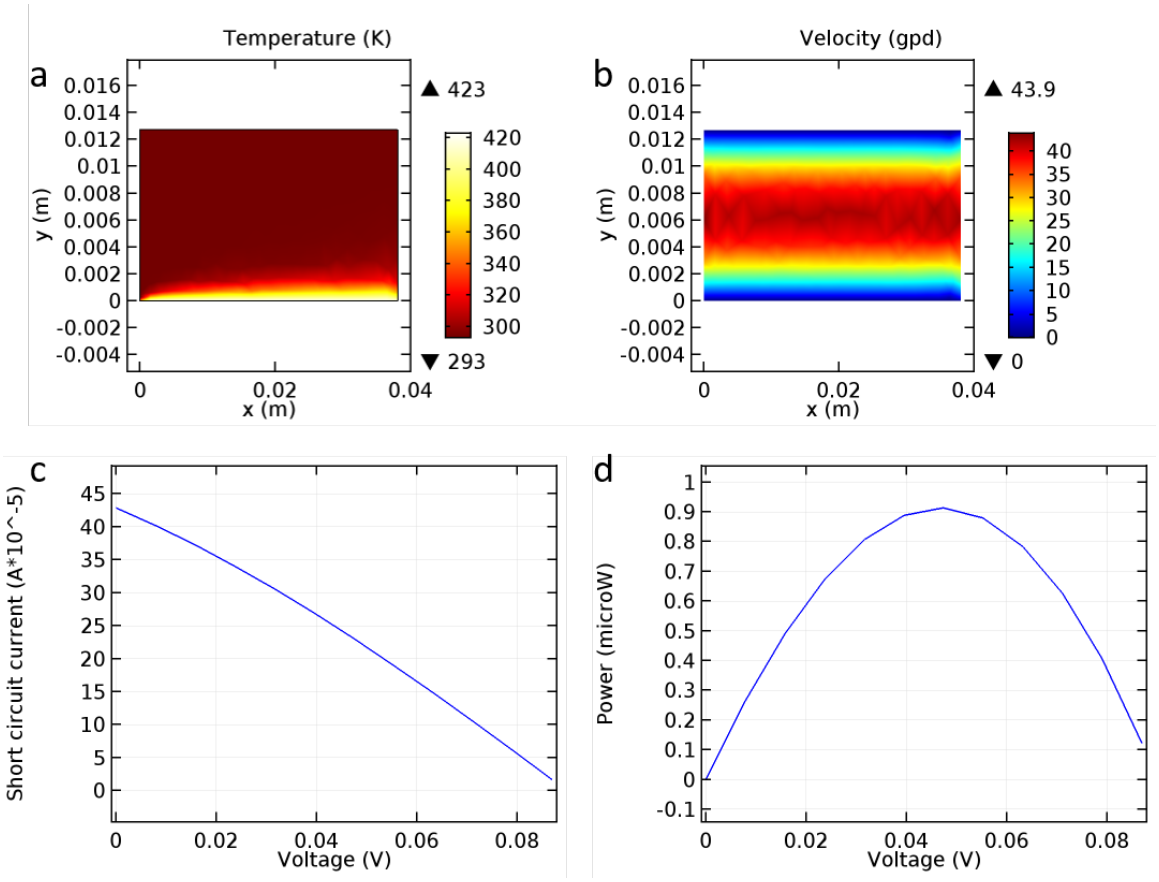

Figure 5.4: COMSOL modeling for average flow rate of 28.16 gpd and distance between the electrodes of 1.5" (a) Surface plot of temperature distribution (b) Surface plot of velocity distribution (c) Current vs voltage (d) Power vs voltage.

boundary condition, is shown in Figure 5.4a and Figure 5.4b. The results of the simulation show a peak in short circuit current when the potential reduces to zero, shown in Figure 5.4c. The simulations also show that the power output produces a peak, as shown in Figure 5.4d at around $0.9\mu W$. The maximum realizable power output numerically achieved for our experimental flow rates, was 2μW, close to our simulation results Figure 5.4d.

5.4.2 Experimental

Our thermocell (Figure 5.3) was developed with equally spaced (1.5" apart) graphite electrodes inserted into the flow path of the working fluid. With this spacing a total pair of 44 electrodes are available as a place where oxidation and reduction could occur. The power

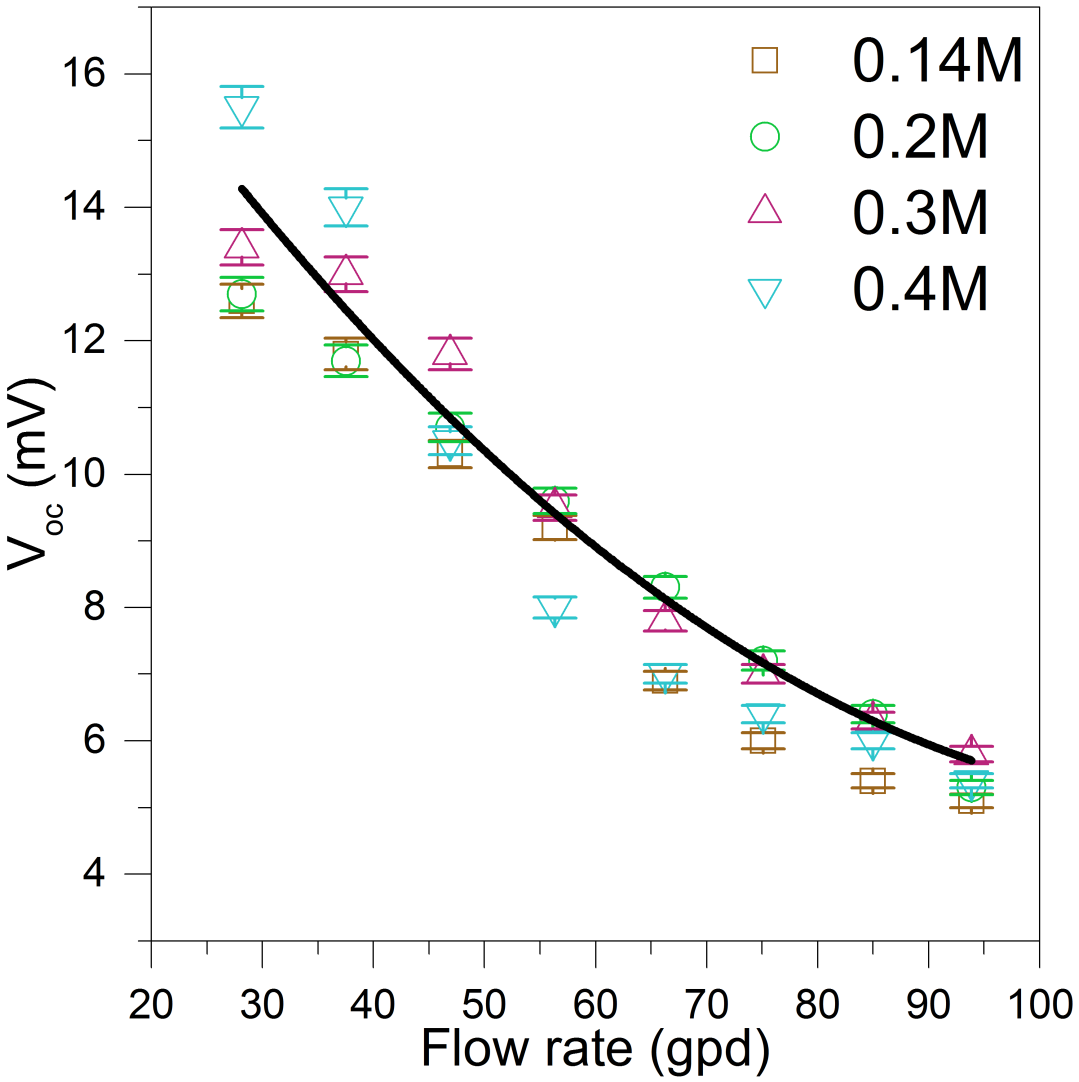

Figure 5.5: Hybrid cold plate performance for 0.14 M (brown), 0.2M (green), 0.3 M (pink) and 0.4M (blue) potassium ferri/ferro cyanide between first-second graphite electrode that are 1.5 inch (nearest) apart as function flow rate. V_{oc} is the open circuit voltage.

performance between two adjacent electrodes Figure 5.5,Figure 5.6,Figure 5.7. The V_{oc} (Figure 5.5) is independent of the concentrations of the electrolyte, for high concentrations near the saturation limit, identified in earlier literature [51][87][67]. However, the increase in concentration has proportional effect on the measured current (Figure 5.6). The increase in current is due to larger number of redox ions available for reaction at the electrodes, as well as increase in electrical conductivity of the electrolyte. The increase in electrical conductivity reduces mass transfer resistance of ions. The maximum power P_{max} was

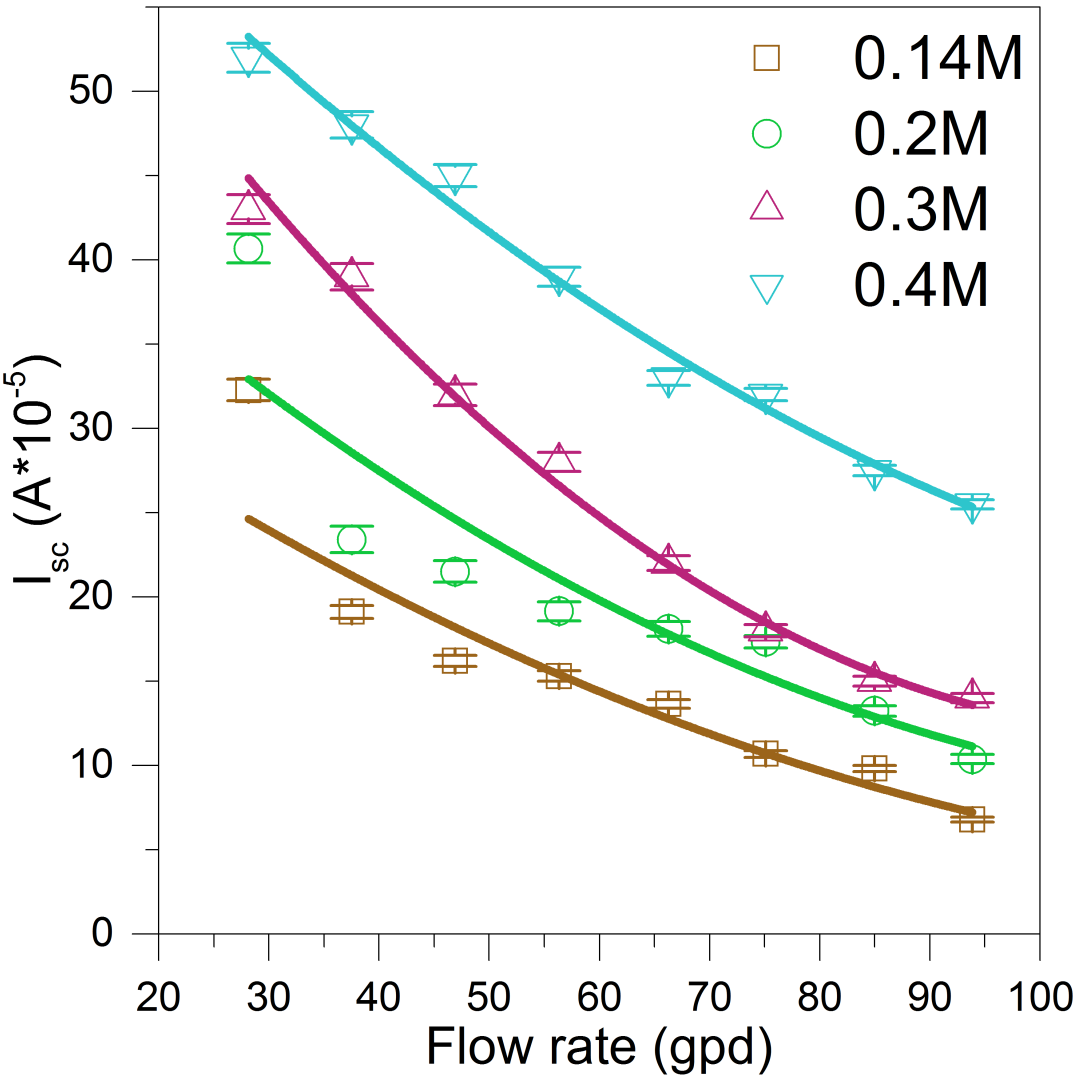

Figure 5.6: Hybrid cold plate performance for 0.14 M (brown), 0.2M (green), 0.3 M (pink) and 0.4M (blue) potassium ferri/ferro cyanide between first-second graphite electrode that are 1.5 inch (nearest) apart as function flow rate. I_{sc} is the open circuit voltage.

calculated using [34]:

$$P_{max} = 0.25 * V_{oc} * I_{sc} \tag{5.11}$$

Our results show that open circuit voltage (Figure 5.5) increases with a decrease in flow rate because a slower flow rate raises the temperature gradient between the two electrodes. The higher temperature difference due to a low flow rate increases the open circuit voltage available at the electrodes. As mentioned previously the V_{oc} is independent

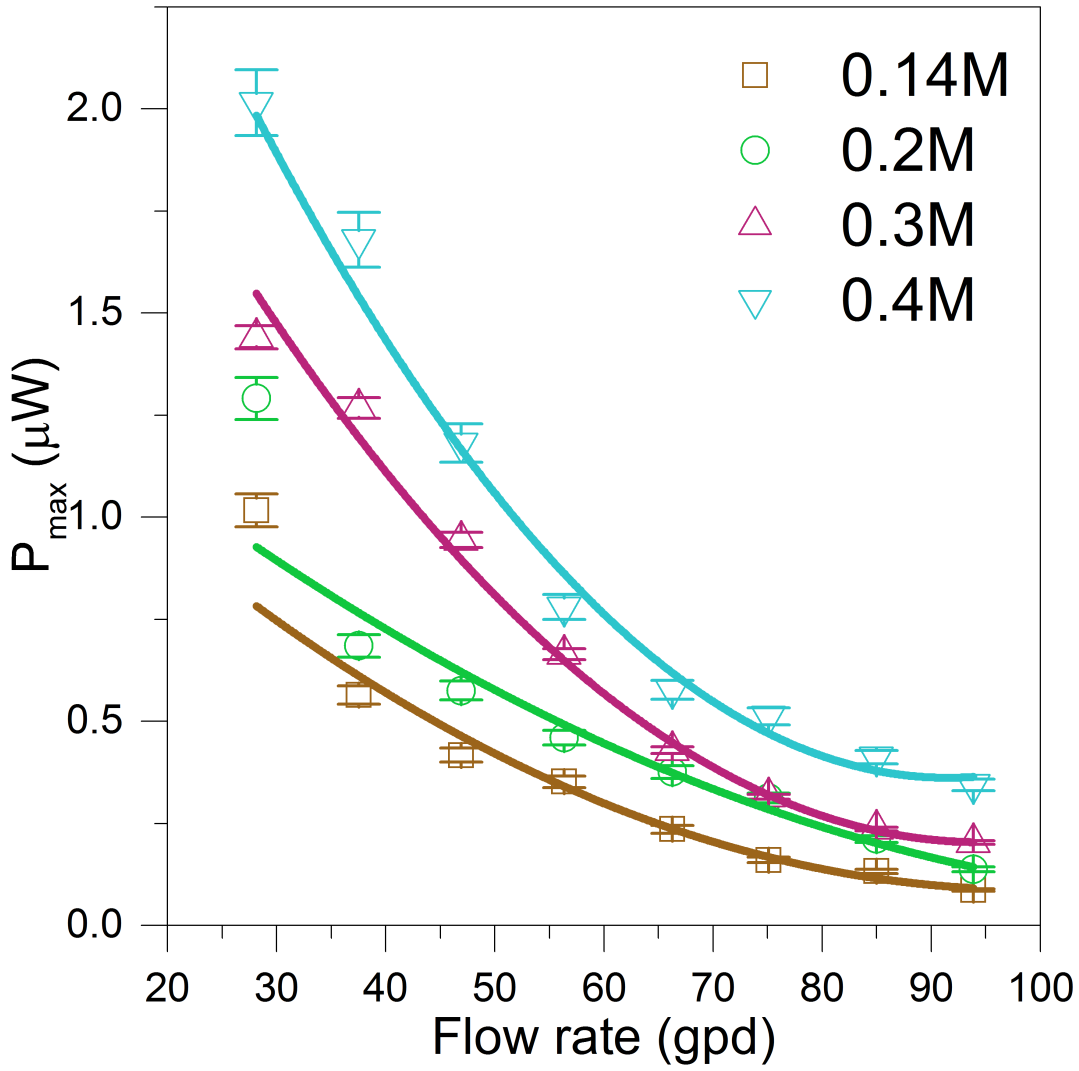

Figure 5.7: Hybrid cold plate performance for 0.14 M (brown), 0.2M (green), 0.3 M (pink) and 0.4M (blue) potassium ferri/ferro cyanide between first-second graphite electrode that are 1.5 inch (nearest) apart as function flow rate. P_{max} is the open circuit voltage.

of concentration of the electrolyte, this is apparent from the fairly close scatter and the various concentrations are represented by a single trend line. The higher temperature of the down-line electrode also increases the conductivity of ions and consequently the current output. Overall a maximum power output of 2 μW was recorded for a flow rate 28.16 GPD and redox species concentration of 0.4 M. For the current arrangement of 44 paires of electrodes we achieved a maximum experimental output of 88 μW.

After measuring the power performance of adjacent electrodes, performance of the

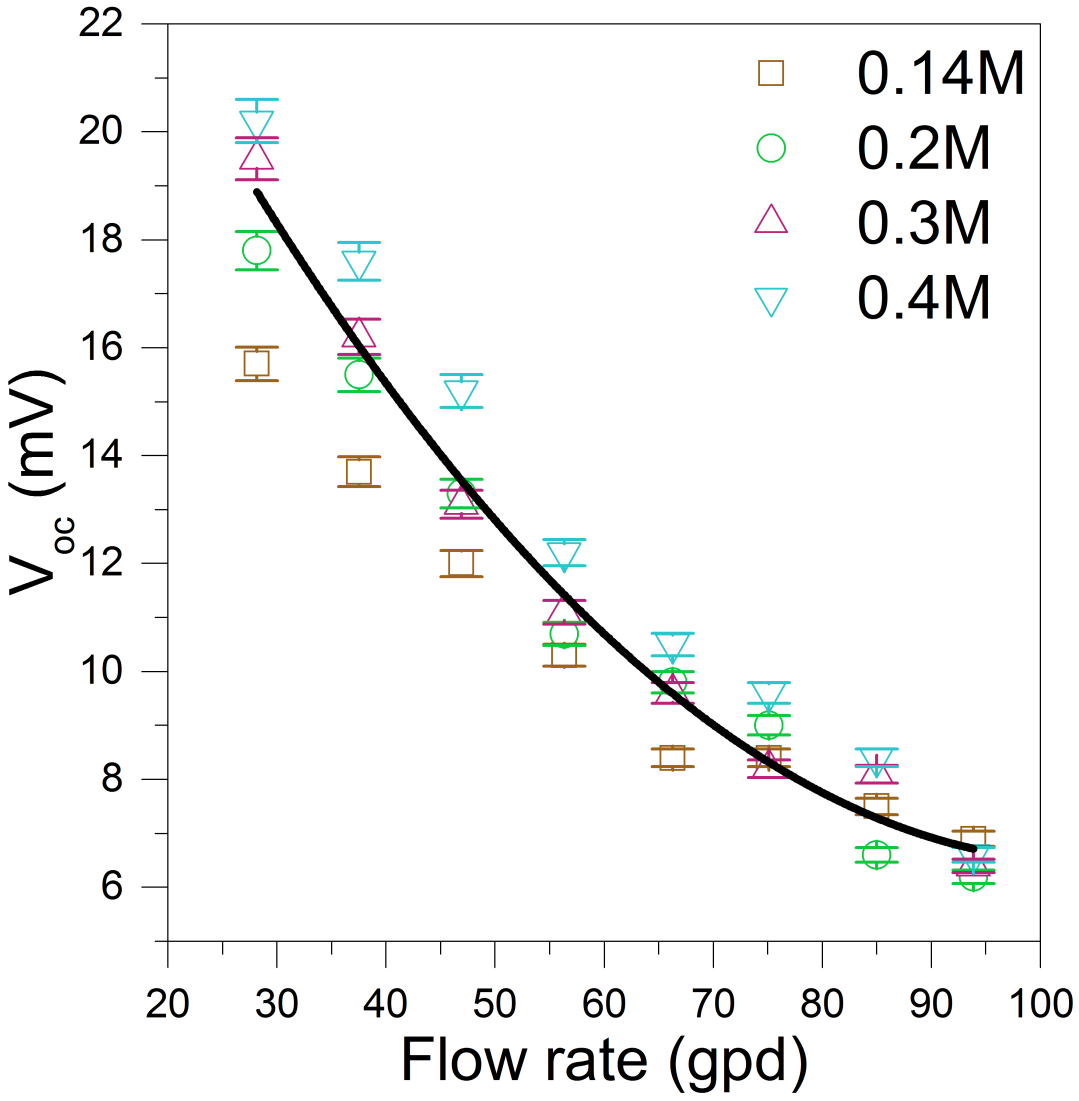

Figure 5.8: Hybrid cold plate performance for 0.14 M (brown), 0.2M (green), 0.3 M (pink) and 0.4M (blue) potassium ferri/ferro cyanide between first-last graphite electrode that are 33.7 inch (furthest) as function flow rate. V_{oc} is the open circuit voltage.

electrodes furthest apart (33.7") was recorded (Figure 5.8,Figure 5.9,Figure 5.10). For a convectional stationary thermocell the power drops as the electrodes are taken further apart because the ohmic (ion mass transfer) resistance increases. For a stationary TEC, if the electrodes are kept at constant temperature and are moved further apart from each other the V_{oc} will remain same as temperature difference is constant but the current will drop as the internal ohmic resistance of thermocell increases. However, the V_{oc}, I_{sc} and P_{max} were observed to be higher than in the case of near-pair electrodes. This was due to higher

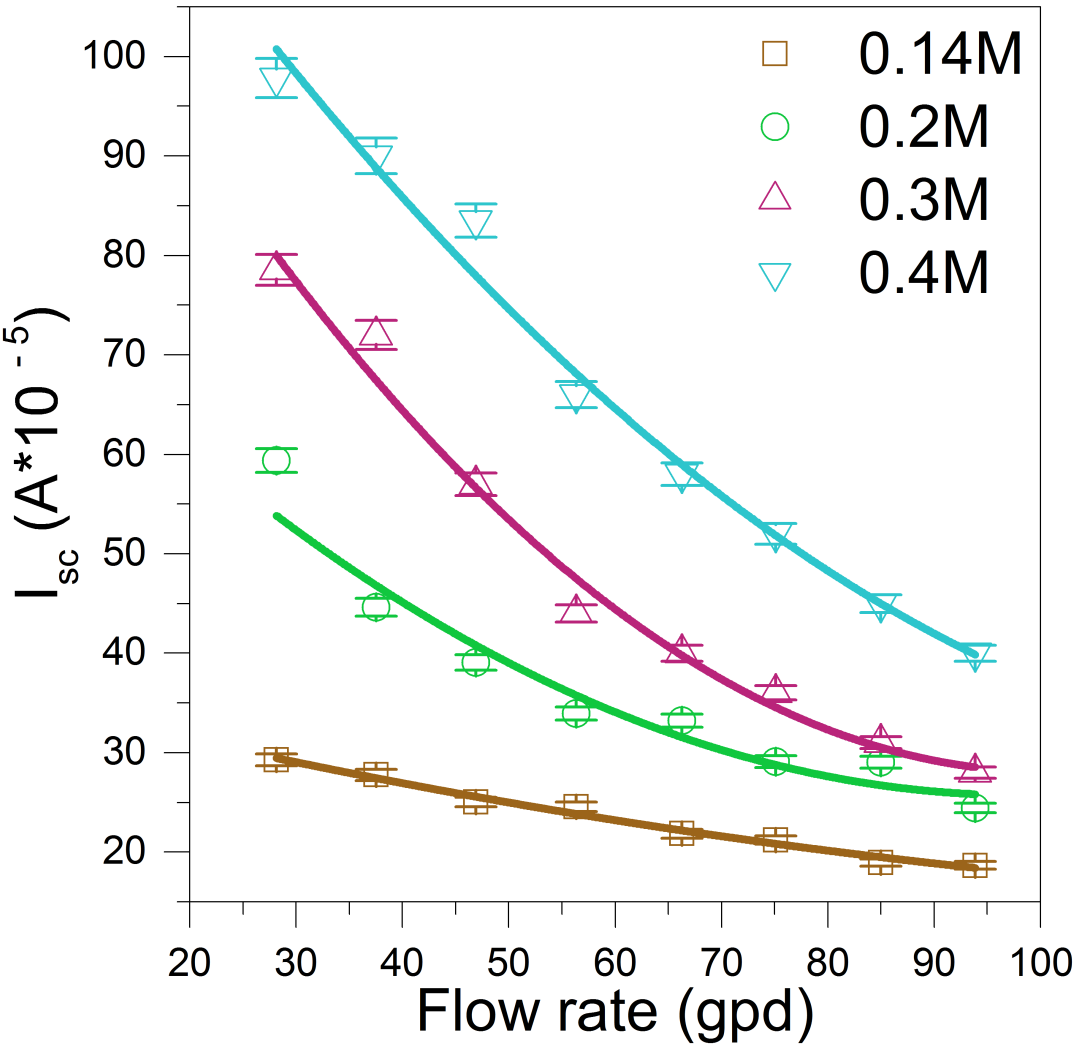

Figure 5.9: Hybrid cold plate performance for 0.14 M (brown), 0.2M (green), 0.3 M (pink) and 0.4M (blue) potassium ferri/ferro cyanide between first-last graphite electrode that are 33.7 inch (furthest) as function flow rate. I_{sc} is the short circuit current.

temperature difference present for the electrodes which are further apart. The higher temperature difference was able to overcome the increase in ohmic resistance that was a result of an increase in electrode separation spacing [32] [83]. The trend for V_{oc}, I_{sc} and P_{max} is having a power law relationship with respect to flow rate, the power law trend is more apparent with P_{max} as it is a product of two variables open circuit voltage and short circuit current.

In addition to converting waste-heat, the flow thermocell will also provide convective

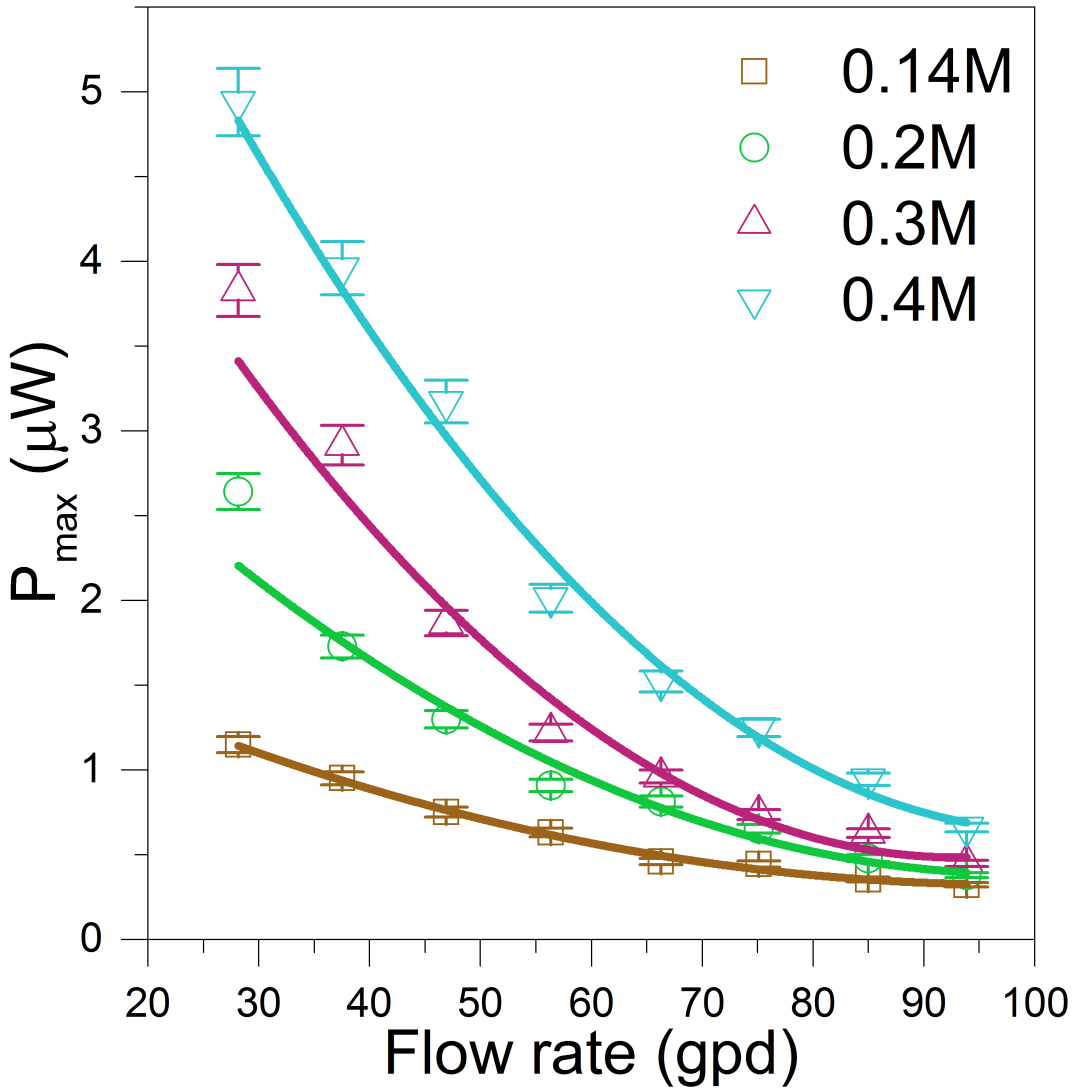

Figure 5.10: Hybrid cold plate performance for 0.14 M (brown), 0.2M (green), 0.3 M (pink) and 0.4M (blue) potassium ferri/ferro cyanide between first-last graphite electrode that are 33.7 inch (furthest) as function flow rate. P_{max} is the maximum power.

cooling. The convective heat transfer coefficient is a major bottleneck in achieving low thermal resistance for cooling. Cooling performance is assessed by calculating the average heat transfer coefficient (Figure 5.11) at the entrance and along the entire thermocell. The average heat transfer is calculated using equation:

$$\bar{h} = \frac{Q_{conv}}{A * \Delta T_{lm}} \tag{5.12}$$

where Q_{conv} is the amount of energy convected from the bottom surface, A is the area of the heated surface and ΔT_{lm} is the log mean temperature difference. The average heat transfer coefficient is about 7 fold higher at the entrance than for the entire plate, this is because the thermal boundary layer thickness is zero at the entrance. As the thermal boundary layer develops the average heat transfer coefficient decreases. Along the rest of the thermocell an average heat transfer coefficient of 450 $W/(m^2.K)$ (Figure 5.11b) was achieved. This value is about an order of magnitude larger than free air convection and two-fold higher than forced air convection [152].

The geometry of the cold plate channel is 6.35 mm by 19.05 mm (0.25" by 0.75"). The heat transfer coefficient varies inversely with channel width [153]. Future use of a microchannel heat exchanger that has a channel width less than 1 mm should be considered to enhance the heat transfer coefficient and resultant cooling capability [154]. Jet impingement can also be used to increase the heat transfer coefficient. For our current setup the highest Reynold number was about 340 (laminar, Re $<$ 2300) corresponding to flow rate 93.87 GPD. Turbulent flow will also increase the heat transfer coefficient.

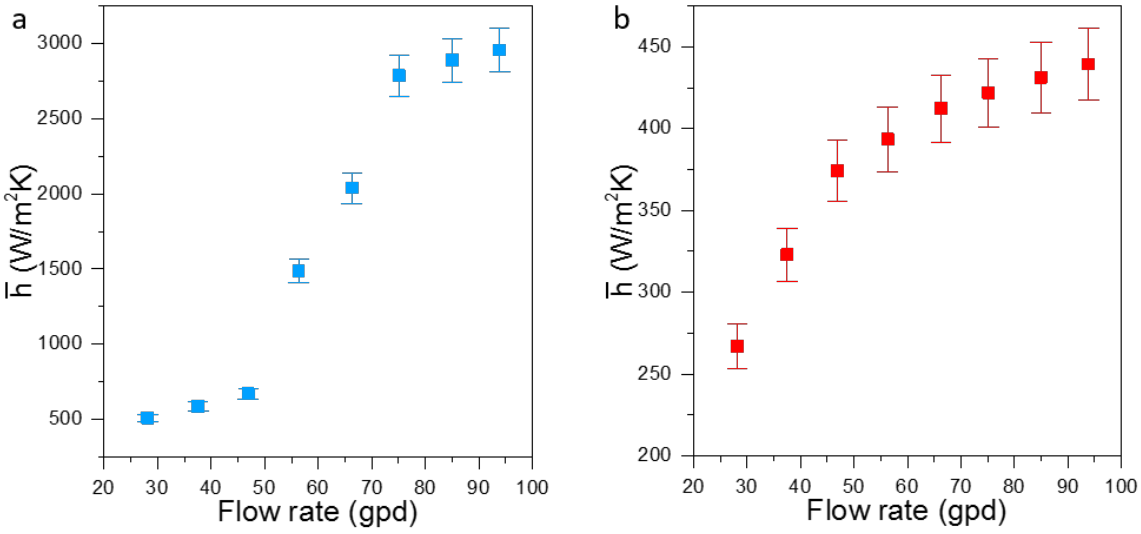

Figure 5.11: Average heat transfer coefficient as function of flow rate (a) at entrance between first and the second electrode 1.5 inch apart (b) between the first and the last electrode 33.7 inch apart.

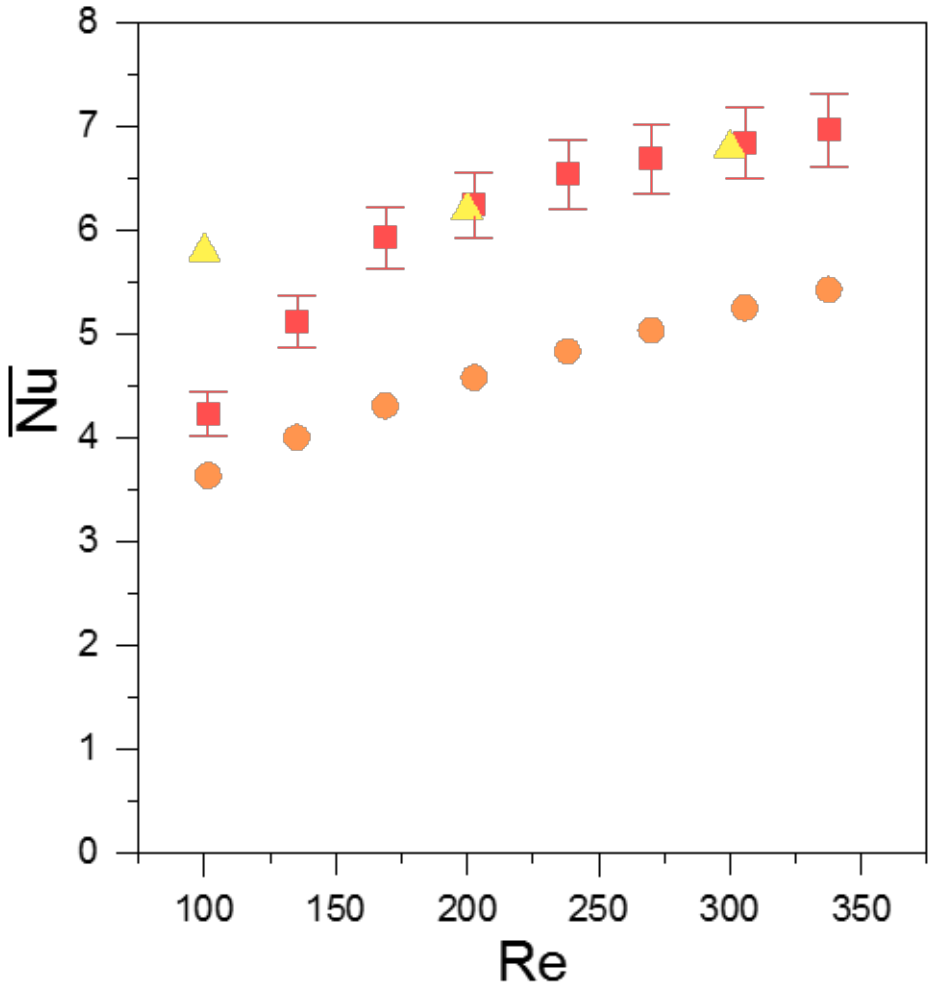

Figure 5.12: Average Nusselt number calculated for the entire cold plate experimental (red square), rectangular channel literature data (yellow triangle) and circular channel literature data (orange circles).

The flow is simultaneously developing the hydrodynamic and thermal boundary layers. This is suitable for maximum heat transfer. To compare the data with existing empirical models, the non-dimensional Nusselt and Reynold number were calculated for our setup (Figure 5.12). The non-dimensional data compared well with the limited literature available for simultaneously developing flow for rectangular [155] and circular channels [152][156].

To compare the heat convection capability of our thermocell with that of other liquid

cooling architectures, we calculated the thermal resistance using (Eq.5.13):

$$R = \frac{\Delta T}{Q_{in}} \tag{5.13}$$

where ΔT is the temperature difference between the inlet and outlet of the fluid and Q_{in} is heat in.

5.5 Discussion

A balancing acts arises between the amount of energy harvested and amount of heat that is convected away, as they have inverse relation to flow rate. This was shown by the observed inverse relationship between the flow rate and power output where (Figure 5.7,Figure 5.10) the heat transfer coefficient decreases with decreased flow rate (Figure 5.11).

In our current design of the flow thermocell all of the electrodes are inline and inserted into the top plate. The electrodes interact with the flowing fluid and are influenced by the temperature of the fluid. They increase in temperature primarily due to the convective heat transfer of heat from the boundary condition to the flowing fluid. The inline temperature gradient that results is perpendicular to the maximum temperature difference available (i.e. between the top and bottom plate). To take advantage of the maximum temperature gradient available in the perpendicular direction, electrodes need to be located on the top and bottom of the thermocell. This will also help address the inverse relationship between the energy harvested and the heat transfer coefficient, as in this case the increasing flow rate will help increase heat transfer and will also help in maintaining the high temperature difference between the top and bottom electrodes.

To investigate the proposed configuration, COMSOL simulation was carried out. The geometry and all other boundary conditions were kept constant. The only modification was the position of electrodes which were changed to being located perpendicular to the

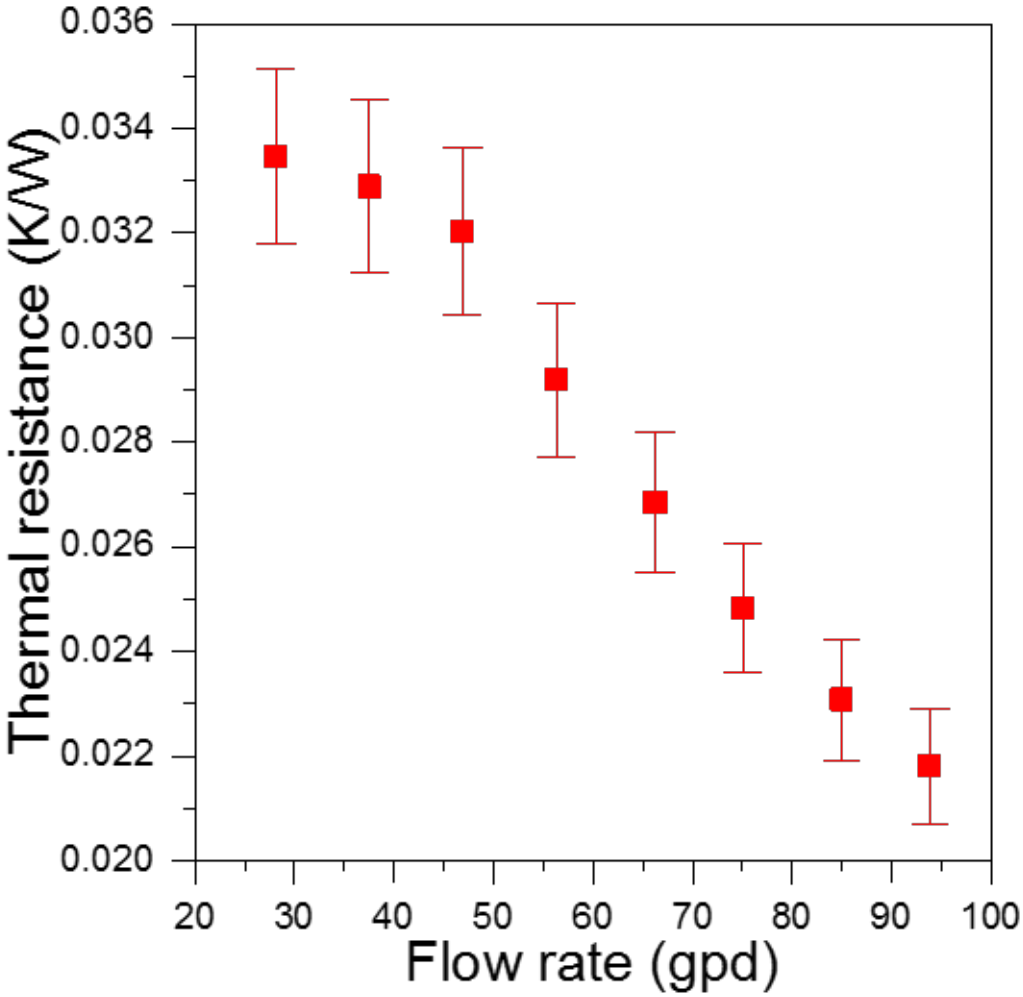

Figure 5.13: Thermal resistance of cold plate as a function of flow rate.

direction of the heat flux. Our simulations demonstrated a maximum power output that increased by 7.4 times (details can be found in the next Chapter). Given 44 pair of electrodes, a combined power of 651 μW will be available. This power can be useful in powering low-powered devices such as temperature sensors and monitors.

Presently, low-cost low-power temperature sensors are used in key locations to monitor temperature and forward the information via relay nodes to operators [157][158]. By employing the thermoelectric effect, our thermocell we can monitor temperature without the need of these sensors since the voltage output will be proportional to the temperature of the device temperature. As a result, real-time monitoring of temperature throughout places

such as data centers at any instance will be possible. Knowledge of the complete temperature profile of data centers will greatly reduce chances of hot spot occurrence and device damage [157]. By employing a flow thermocell cell sensors and monitors can operate without batteries. This application can be extended to wherever liquid cooling is employed. One such example is in battery packs of electric vehicles. Liquid cooling provides greater safety, performance, and longevity of battery life compared to traditional cooling methods [159, 160]. The novel thermocell design can by complementing existing safety features in batteries while also providing temperature profiles (Figure B.1).

5.6 Conclusion

The fTEC has been shown to cool high heat flux devices and harvest electrical energy from the waste-heat, in parallel. Its' development can be extended to all application employing liquid cooling. The current design is yet to be optimized both in terms of electrode material and electrode position. In its current state we can harvest 88 μW of power which can be useful for powering low-powered devices such as wireless sensors used in sending information such as temperature profiles to a central monitoring client. fTEC also showed a cooling performance in terms of the heat transfer coefficient of 450 $W/(m^2.K)$ which is an order of magnitude higher than that of free air convection and two-fold higher than that of forced air convection.

CHAPTER 6
OPTIMIZATION OF ELECTRODE MATERIAL AND GEOMETRY FOR FLOW THERMO-ELECTROCHEMICAL CELL

6.1 Introduction

In the last chapter flow thermo-electrochemical cell (fTEC) was invented to harvest waste heat. This chapter will focus on improving the performance of fTEC. This would be achieved by improving the electrode material and their positioning.

Carbon nanotubes (CNTs) first documented evidence dates back to 1950s [161]. However, it was not until Suimo Iijima landmark work "Helical microtubules of graphitic carbon", that CNTs became focus of intense research [162]. The monumental work, explained the formation of CNTs then referred as graphitic carbon needles through arc discharge evaporation method. The CNTs formed had diamater is the range of 4 to 30 nm and length of 1 μm. The carbon nanotubes were grown on the negative electrodes, in an argon-filled chamber with pressure of 100 tor. CNTs are cylinders of graphene, mainly consisting of two main types, single-wall nanotube (SWNT) and multiwall nanotube (MWNT). They may have open or close ends. Diameter of SWNTs is typically between 0.8 to 2 nm while for the MWNT it is between 5 to 20 nm. Length of CNTs ranges from 100 nm to several centimeters. The wide range in the length dimension help bridge the gap between molecular to macroscopic scales.

The immense research interest in CNTs is due to its exceptional electrical, thermal and mechanical properties. CNTs can be metallic or semi conducting depending on there chirality i.e. orientation of graphene lattice with respect to tube axis. MWNTs can carry current upto 10^9 A cm^{-2}. Individual SWNTs can have thermal conductivity as high as 3500 W $m^{-1}K^{-1}$ at room temperature which is more than diamond. For individual CNTs

the elastic module is about 1 TPa and tensile strength is 100 GPa. However, for bulk material such as CNT sheets and yarns, the thermal conductivity and mechanical strength remains low. Efforts are needed to developing understanding as to why the bulk material thermal and mechanical properties are much lower.

CNTs have greatly improved the efficiencies and power densities of thermocells. CNTs have replaced more expensive Platinum electrodes, as a more cost effective and more efficient alternative. More importantly, they have helped researchers look beyond the cost of thermocells and focus on performance parameters.

6.2 Electrode Configuration that Maximizes P_{out}

In the last chapter, flow thermo-electrochemical cell (fTEC) was invented. It was shown that flowing electrolyte can simultaneously provide cooling and be a source of energy harvesting. The electrodes were positioned such that all of them were attached to the top plate i.e. the cold side. It has been identified that in order to harvest maximum energy the electrodes need to be located on hot and cold side. To take advantage of a more favorable positioning of electrodes, the electrodes would be place perpendicular to heat flux, as shown in Figure 6.1. In order to maximize P_{out} we need to maximize the temperature gradient in between anode and cathode surfaces without moving them far apart.

To better understand the benefit of having electrode in different configuration, temperature profile present inside the cold plate was simulated using COMSOL. The temperature profile can be seen in Figure 6.2. Heat flux is applied at the bottom plate to maintain temperature of the bottom side around 393.15 K, labeled as T_h. The top side is exposed to ambient temperature at 20 ^{o}C. Top side temperature (T_c) increases gradually along the length of the channel, indicating that forced convective fluid is effective in removing substantial amount of heat from the cold plate. T_m is the temperature of the fluid along the centerline of fluid flow, the increase of which is considerably higher than that of T_c. With electrodes inserted on the top plate, the mean temperature at the outlet ($T_{m,o}$) determine the

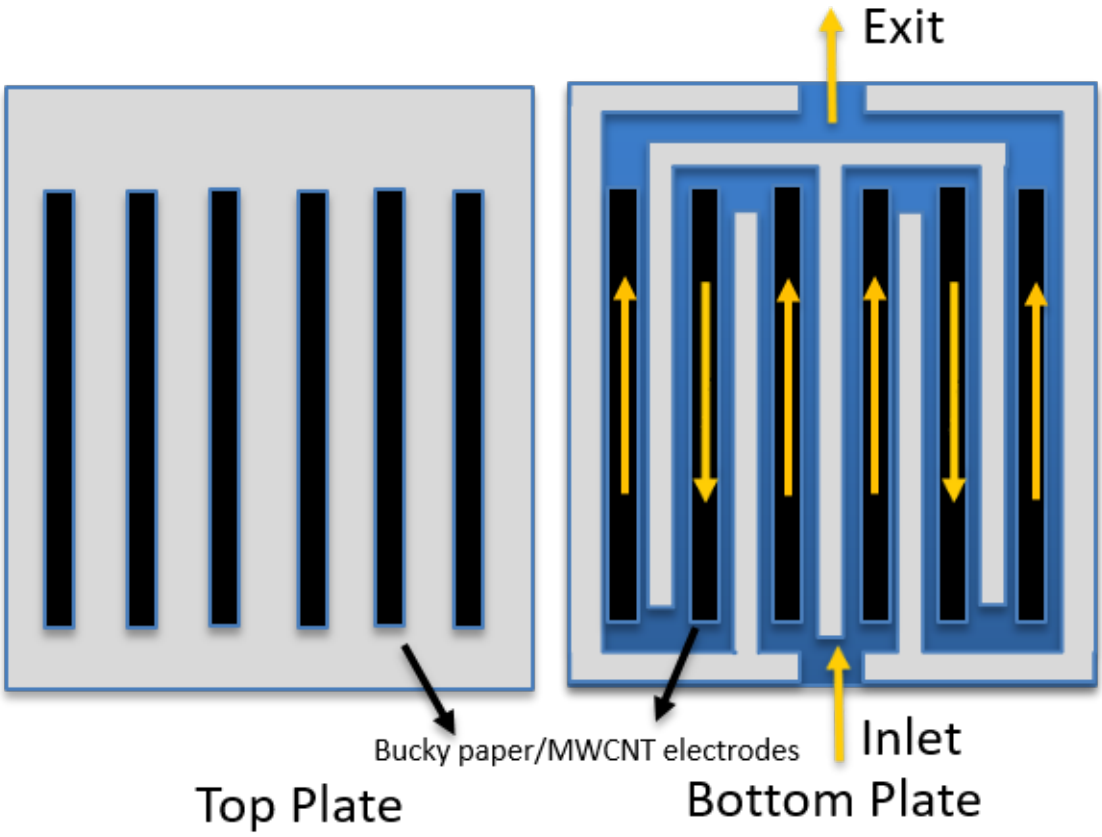

Figure 6.1: Electrode configuration on top and bottom plate.

maximum potential available for energy harvesting. To take advantage of maximum potential electrodes need to be further apart on the top plate, while this would ensure a higher temperature available (more voltage) but will also increase the ohmic drop (less current). Looking at Figure 6.2, it is clear that the maximum potential is temperature available is between the top and bottom plate (T_h-T_c) and is also fairly constant, as opposed to electrodes at the top plate ($T_{m,e}$-T_m).

To take advantage maximum temperature available (T_h-T_c), COMSOL simulation was carried out with electrode on the top and bottom of the flow channel, on the plane perpendicular to the direction of heat flux shown in Figure 6.1. Having electrodes located on top and bottom plates will increase the maximum power output due to availability of higher temperature difference. The COMSOL simulation showed that the power output would

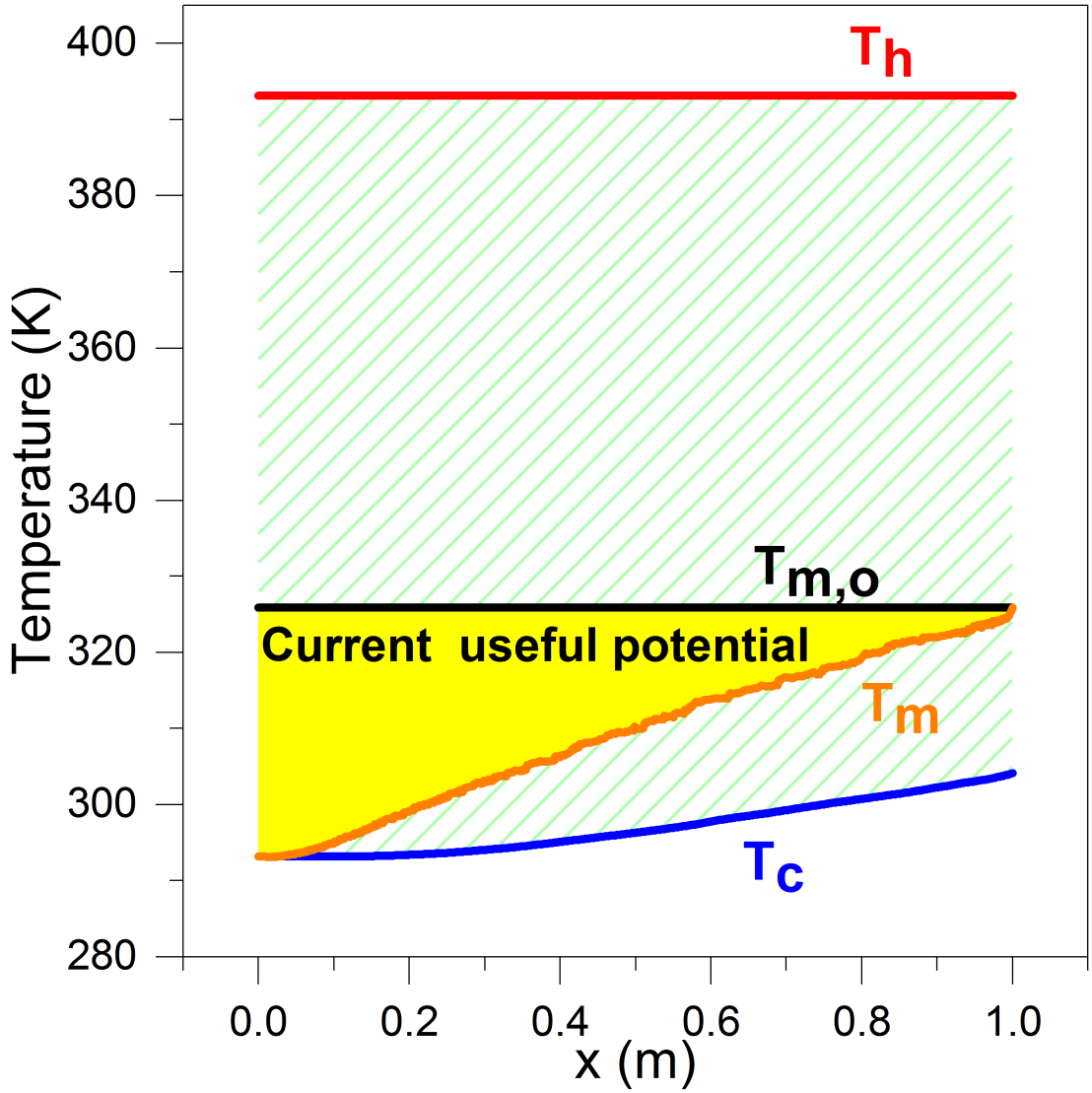

Figure 6.2: Temperature profile inside the cold plate as a function of length (x). T_h is the temperature of the bottom plate where the heat flux is provided by heater, $T_{m,o}$ is the mean exit temperature at the outlet, T_m is the mean temperature of the fluid as it flows through the channel and T_c is the temperature of top plate exposed to ambient. Temperature potential with electrodes inserted on the top plate is $T_{m,e}$-T_m, represensted by the yellow shaded region. Tempererature with electrodes located on the top and bottom electrode is T_h-T_c represented by the green pattern pattern in addition to yellow shaded region.

increase by 7-fold, as shown in Figure 6.3.

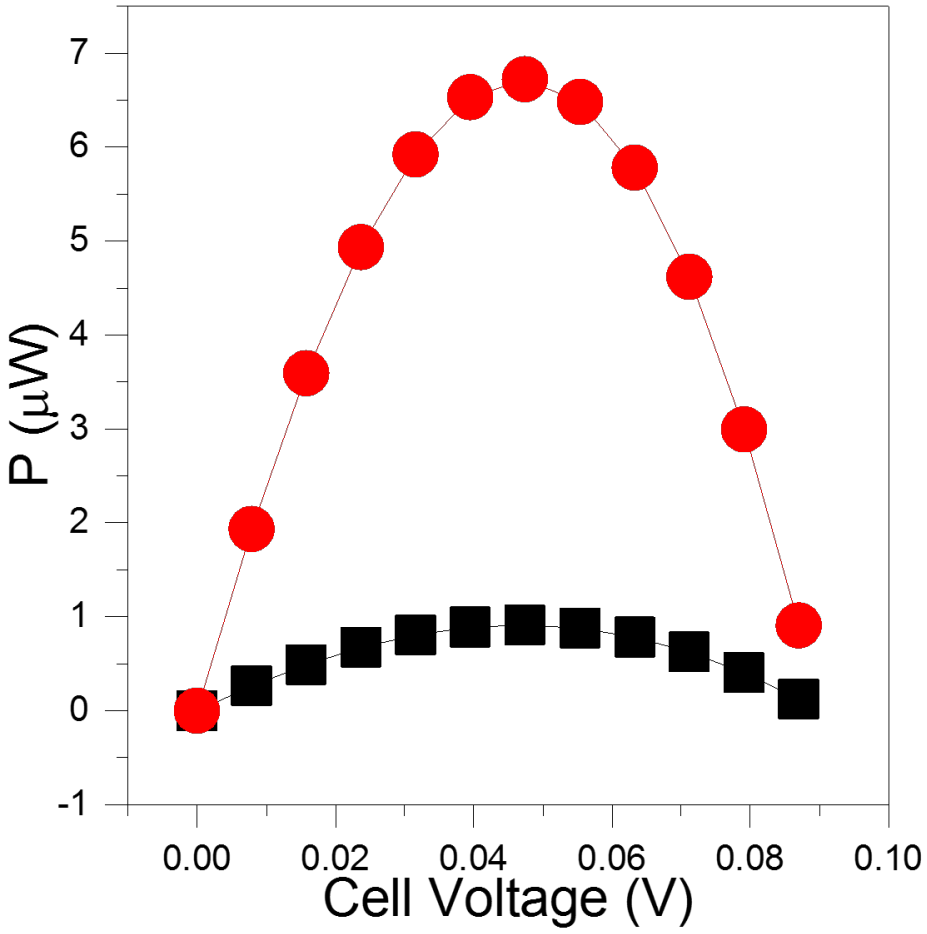

Figure 6.3: COMSOL simulation, power comparison between electrode on just the top plate (black square) vs those on both the top and bottom plate(red circle).

6.3 MWNT buckypaper electrodes

MWNT electrodes were used to improve power performance of fTEC. CNTs of the form buckypaper were used. The use of CNTs would provide faster charge transfer kinetics and increase in electrochemically active surface area for electrode/electrolyte interaction. This is evident from the cyclic voltammetry (CV) scan of the graphite electrodes and MWNT buckypaper electrodes (Figure 6.4). The CV scan shows that the peak current increase by about 30 %, this shows that MWNT buckypaper provides more electrochemically active surface area. The peak separation decreases from 0.15 V to 0.095V for MWNT buckypaper, indicating that the reaction is comparatively more reversible. The ratio of peak current for

MWNT is 0.92 and for graphite is 0.82. The ratio of peak current for MWNT is closer to 1, suggests that reaction at the MWNT buckypaper electrodes is comparatively more self-regenerative.

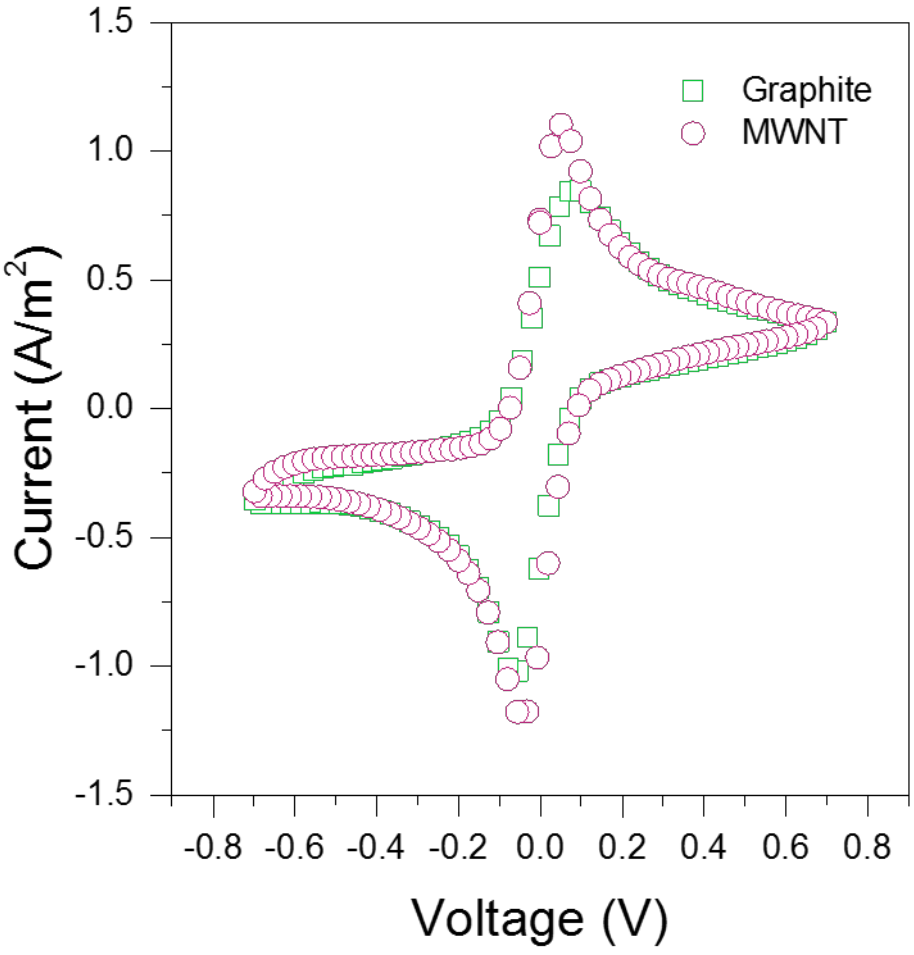

Figure 6.4: Electrode configuration on top and bottom plate.

To investigate the increase in current observed in the CV scan, scanning electron microscopy was carried out to observe the surface of the graphite and MWNT buckypaper. The surface of the graphite is fairly smooth, shown by Figure 6.5c having length scale of 2 μm, compared to nanostructured MWNT buckypaper (Figure 6.6a). The nanostructuring of MWNT provide the higher electrochemically active surface area.

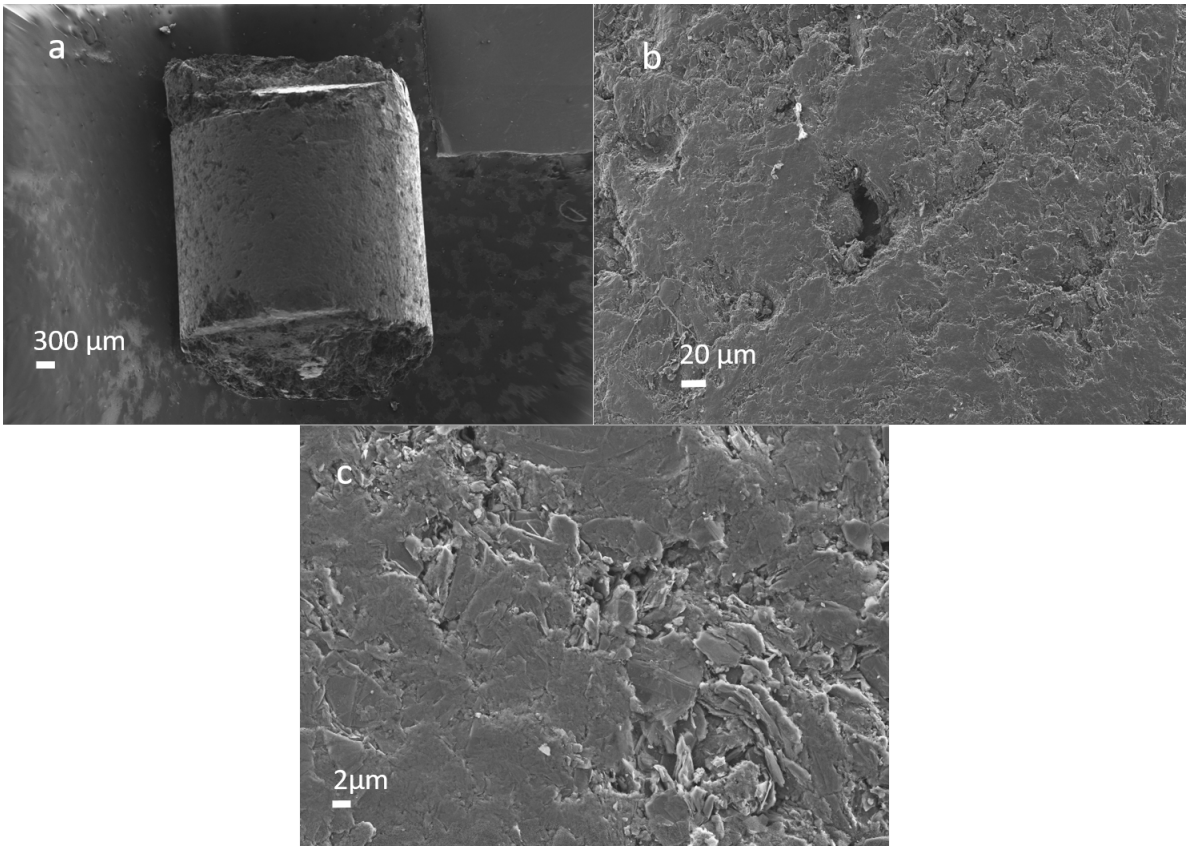

Figure 6.5: SEM images of graphite electrodes (a) scale bars correspond to 300 μm (b) scale bars correspond to 20 μm (c) scale bars correspond to 2 μm.

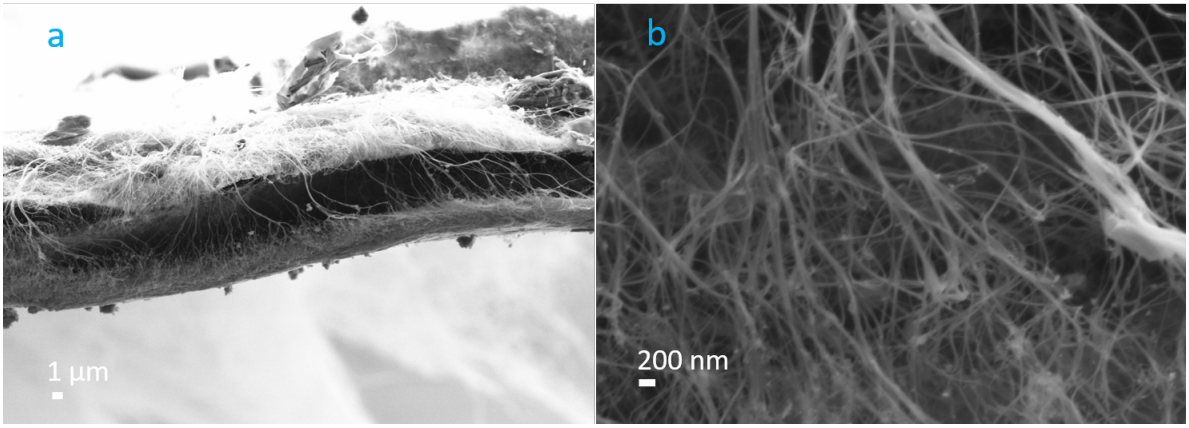

Figure 6.6: SEM images of MWNT buckypaper electrodes (a) cross-sectional view with scale bar correspond to 1 μm (b) cross-sectional view with scale bar correspond t 200 nm

6.4 Experimental

MWNT buckypaper was purchase from Nanocomp Technologies, Inc having product number XAA-0075-01 (Figure 6.6). The MWNT buckypaper is of lengths of approximately 100 μm, thickness 35 μm and diameter of 10 nm. The MWNT buckypaper is prepared by first dispersing MWNNTs in surfactants and aqueous solution. The mixture is then filtered and compressed to form a uniform sheet. The MWNT buckypaper was attached with copper wire with the help electrically conductive silver expoxy. Silver epoxy was purchases from Epoxy Technology Inc. having a product number EJ2189-LV. The MWNT buckypaper were attached to top and bottom with help of electrically insulating two sided tape. The electrically insulating tape is necessary to prevent short circuit between electrodes.

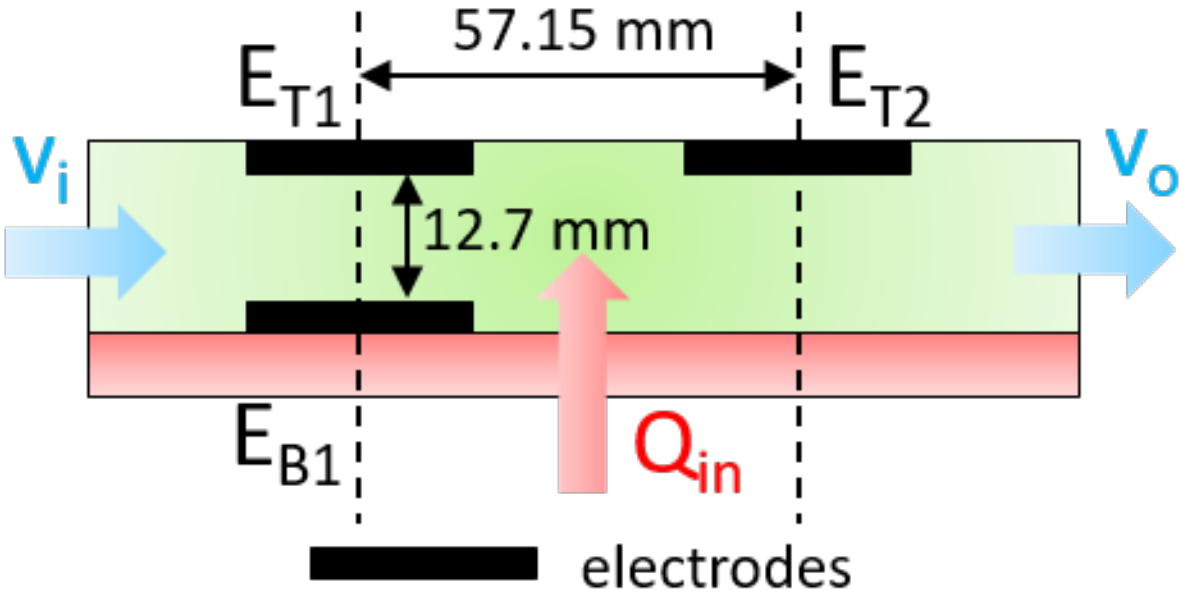

Figure 6.7: The schematic shows the positioning of the electrodes E_{T1}, E_{B1} and E_{T2}, where T stands for electrodes on top plate and B stands for electrodes on the bottom plate. The heat is supplied (Q_{in}) at the bottom of cold plate. The electrolyte flows from left to right.

6.5 Power performance of MWNT buckypaper electrode

The MWNT buckypaper electrodes were tested in the configuration shown in Figure 6.7. This configuration helps to compare electrodes parallel and perpendicular to heat flux.

The V_{oc} is shown in Figure 6.8. The open circuit voltage for the electrodes facing each other is comparable to electrodes in-line. The flow is simultaneously developing flow with respect to both velocity and thermal boundary layer. Therefore, the temperature gain at the adjacent electrodes is comparable to electrodes facing each other. This is represented by the comparable open circuit voltage.

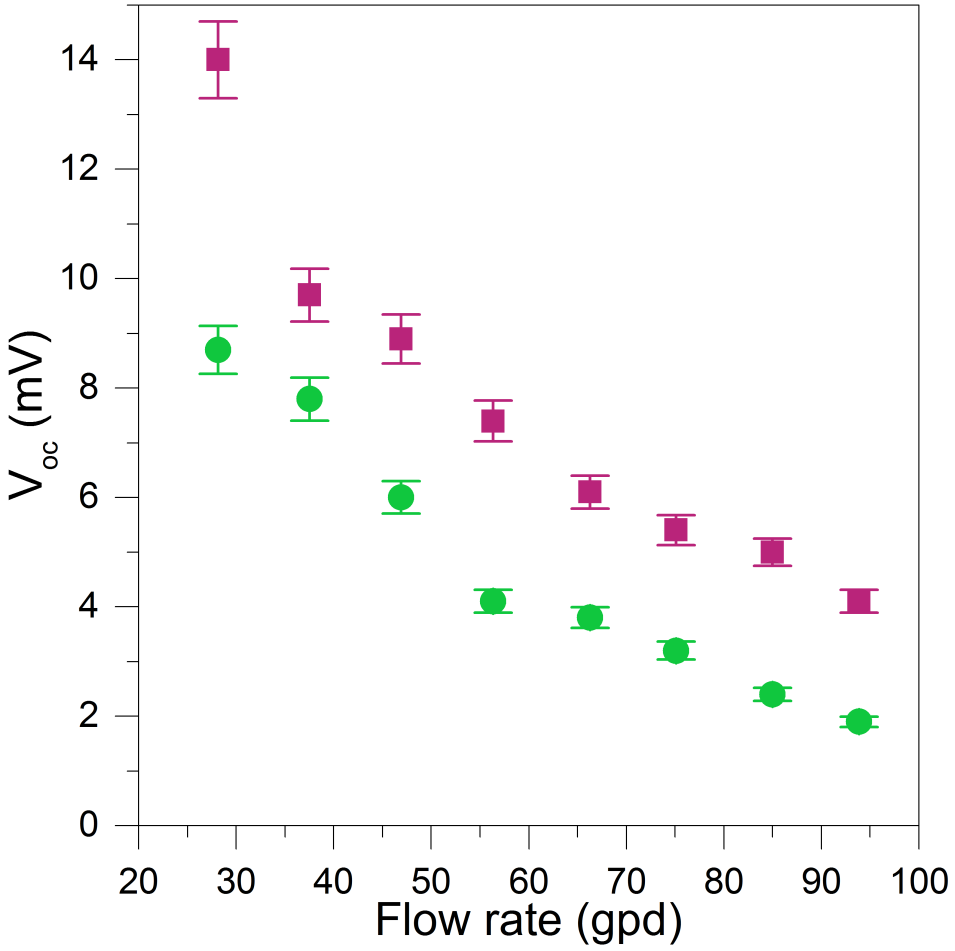

Figure 6.8: Open circuit voltage measured as a function of flow rate on the top plates only (green circle), top and bottom plates (pink square).

Unlike the open circuit voltage, the short circuit current Figure 6.9 is considerably

higher for electrodes facing each other. In addition to the high temperature difference available in the direction parallel to heat flux, the high current is attributed to short distance between the electrodes E_{T1} and E_{T2}. The distance of electrodes facing each other is 4.5 times smaller than the adjacent electrodes. The shorter distance between the two electrodes, means larger the short circuit current due to lower ohmic drop.

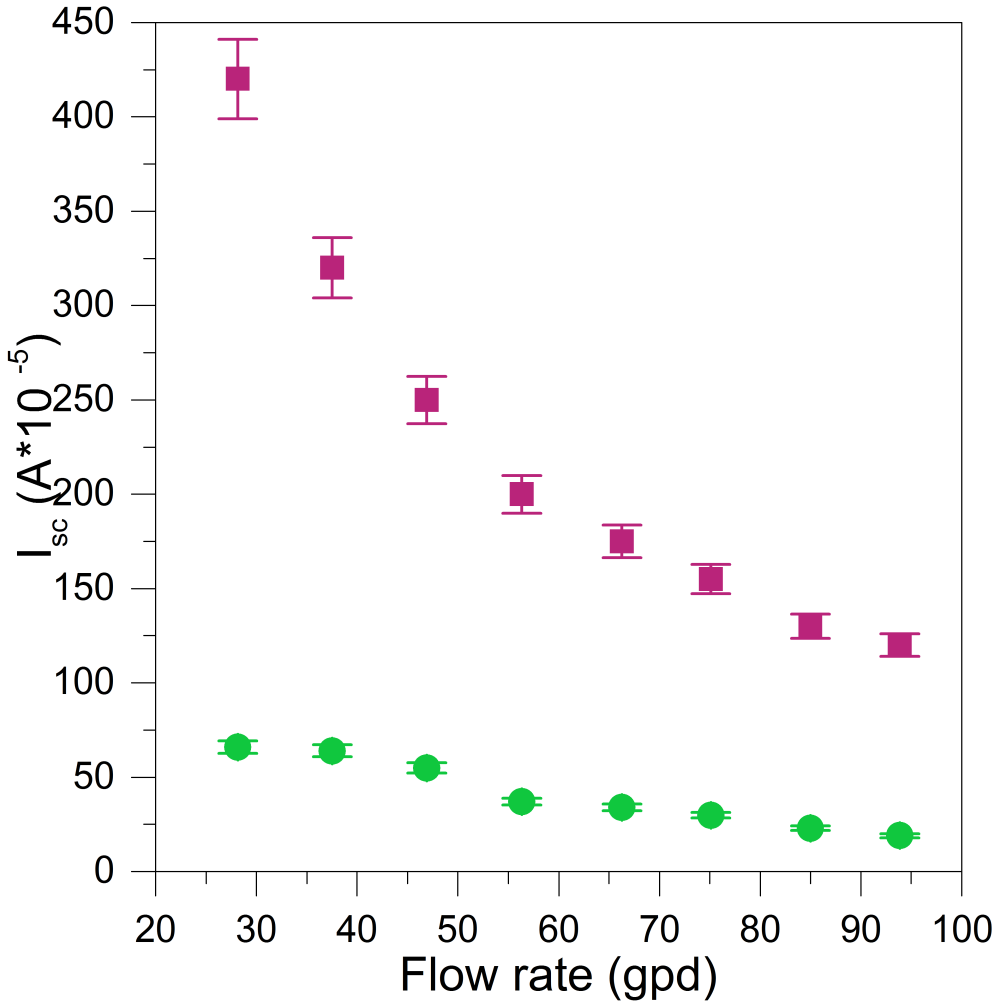

Figure 6.9: Short circuit current measured as a function of flow rate on the top plates only (green circle), top and bottom plates (pink square).

The maximum power is shows in Figure 6.10. This is calculated by $P_{max} = 0.25 * V_{oc} * I_{sc}$. The higher open circuit voltage and shorted circuit measured manifests in higher power measured. The geometry of the electrodes is 12.7 mm by 3.175 mm. Normalizing the maximum power by the cross-sectional area, a maximum power density of 0.36 W/m^2

is measured which is 7.3 times the power density measured in the last chapter. The present flow thermo-electrochemical generator has a temperature of bottom plate maintained at 150 ^{o}C to maximize the heat input and a flow rate is maintained such that to prevent boiling (100 ^{o}C) of the electrolyte as that leads to unstable and low power output. At flow rate below 28.16 gpd unstable power is recorded due to boiling of the electrolyte.

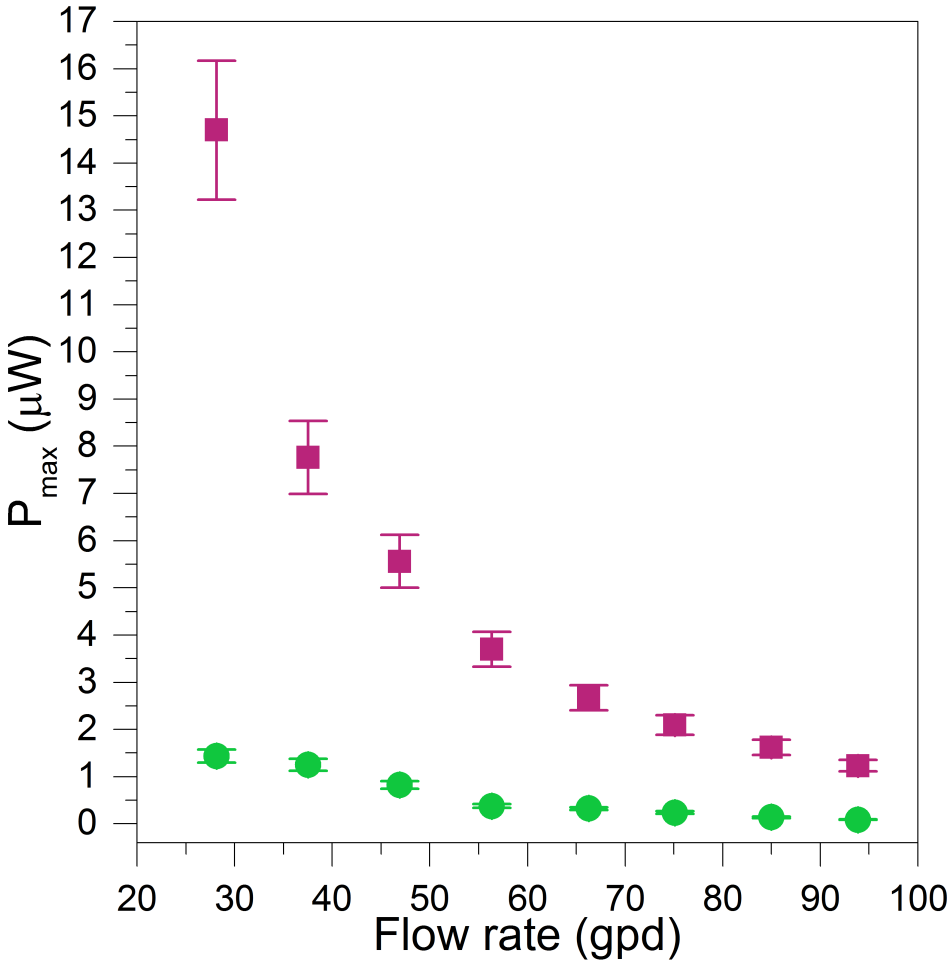

Figure 6.10: Maximum power measured as a function of flow rate for electrodes on the top plates only (green circle), top and bottom plates (pink square).

Figure 6.11 shows the possible uses of fTEC, it can provide cooling while simultaneously generating power, monitoring temperature and powering a wireless sensor enabling thermocouple-less battery less thermal management system.

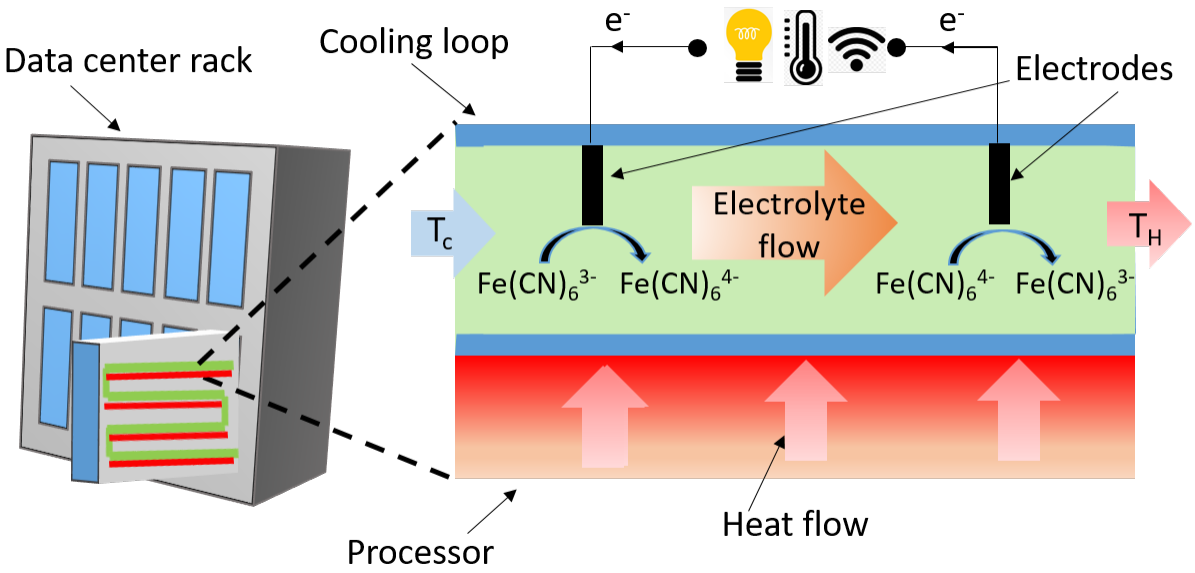

Figure 6.11: Schematic of flow thermo-electrochemical cell *fTEC* showing how electrolyte is providing cooling to data center rack, while simultaneously using the extracted heat to develop power and record temperature. The harvested energy can be useful to power wireless router to communicate with the central temperature monitoring system. T_c and T_H is cold and hot temperature of the electrolyte at inlet and exit respectively.

6.6 Conclusion

The performance of fTEC has been improved by better electrode material and geometry. Employing MWNT electrodes has provided larger surface area and faster kinetics for the redox couple. Also, the more favorable electrode configuration takes advantage of maximum temperature and shorter distance between the electrodes. As a consequence the power density of fTEC has improved by about 7.3 times.

CHAPTER 7
CONCLUSIONS AND RECOMMENDATIONS

7.1 Conclusions

Thermocells are an inexpensive method to convert thermal to electrical energy. In this dissertation electrochemical properties of the standard electrolyte were studied, thermocells was applied in flowing electrolyte configuration and the design was optimized to enhance power output.

In **chapter 3**, a composite of poly (3,4- ethylenedioxythiophene) poly (styrenesulfonate) and carbon nanotube was dispersed in potassium ferri/ferro cyanide. The new composite was studied using electrochemical impedance spectroscopy. Analysis of spectra revealed that the conductivity increase by about 10 % and the interfacial charge transfer reduced by 5-fold. The power output increase by about 30 % in the new electrolyte.

In **Chapter 4**, the work from the previous chapter was extended by measuring the thermal conductivity of the composite electrolyte. It was found the addition of the poly (3,4- ethylenedioxythiophene) poly (styrenesulfonate) and carbon nanotube produces an inverse relationship between the electrical and thermal conductivity, producing an increase in ZT by about 15 %.

In **Chapter 5**, flow thermo-electrochemical cell (fTEC) was identified, fabricated and implemented. The fTEC provides cooling and harvest waste heat. In the initial design graphite electrodes were placed in the path flowing electrolyte. As the electrolyte gained temperature, the ions interacted with electrodes at higher temperature to generate electron that flows through an external circuit and in eventually consumed at the cold electrode. Interestingly, it was seen that seperating electrode spacing did not reduce power output, as the gain in temperature is more than the increase in the ohmic drop.

In **Chapter 6**, the fTEC was optimized for electrode configuration and electrode material. By placing electrodes at the cold and hot plate, the system takes advantage of the maximum temperature difference that is present. The use of MWNT buckypaper provided the faster charge transfer kinetics and increase surface. The improved design increased the power output from 0.05 W/m^2 to 0.36 W/m^2.

7.2 Recommendations

7.2.1 Development of ionic liquids

The use of ionic liquids in thermocells have help address one of its major limitation of i.e. operating above 100 ^{o}C. Also, Seebeck coefficient as high as 7 mV/K have been realized [31]. However, the major bottleneck for the use of ionic liquid is to have ohmic conductivity comparable to aqueous based electrolytes. The three key parameters for thermocell are Seebeck coefficient, ohmic and thermal conductivity. While the first variable is an interface phenomenon taking place at the electrodes, the later two are happening in the bulk solution.

For further development of ionic liquids understanding the complex phenomenon associated with Seebeck coefficient and the use computational aids such as Molecular Dynamic Simulation are pivotal to help aid the process. For example dissolving transition metal redox couples in organic liquids, the reorganization takes place at the inner shell i.e. between the metal and surrounding ligands and also at the outer shell i.e. between the ligands and the solvent. Both structural reorganization affects Seebeck coefficient and each depending on the nature transition metal, surrounding ligand and solvent, making it computationally intensive. However, given the robust nature of computational tools, they can help in further development and deepen understanding of phenomenon associated with ionic liquids.

In this dissertation, Molecular Dynamic Simulation was developed to simulate the electrical conductivity. In future work thermal conductivity computational model will be developed. Combining various properties would help in further development of thermocell.

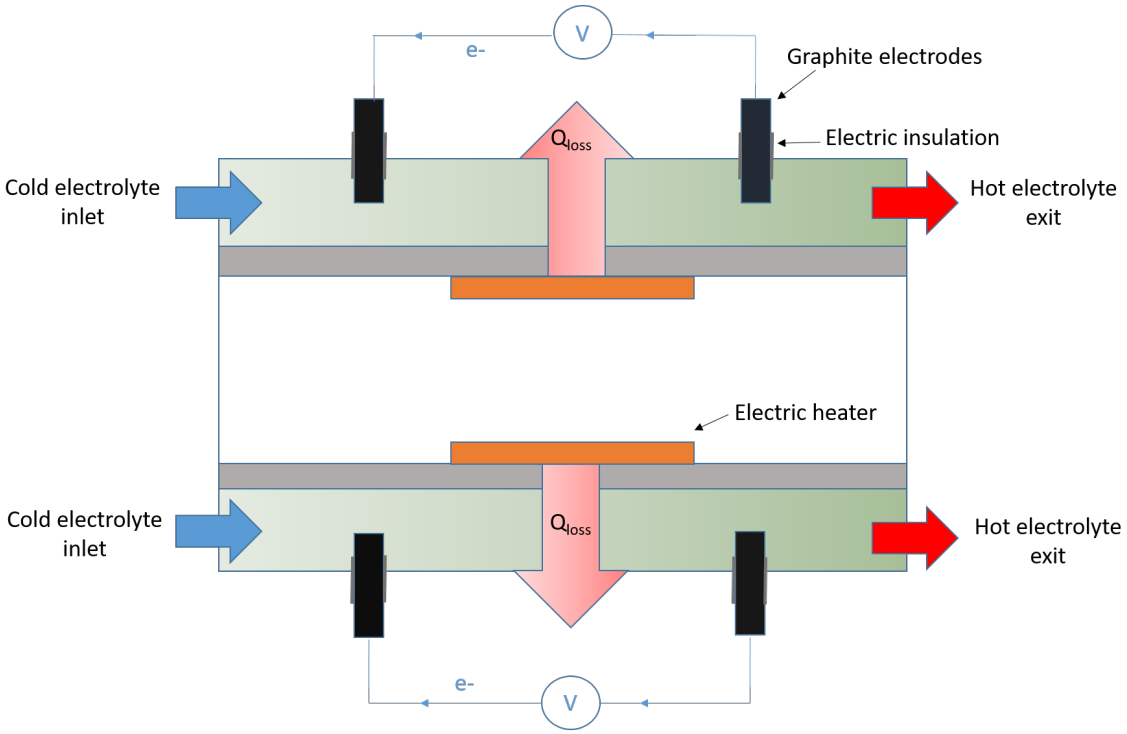

Figure 7.1: Flow thermo-electrochemical energy generator around a heat pipe.

7.2.2 Thermo-electrochemical Generator around a heat pipe

In this dissertation thesis, fTEC has been invented which can provide cooling and harvest waste heat from electronic applications in particular data centers. An extension of this work is proposed to design a fTEC around a heat pipe. Pipe are the most common piece equipment used for transporting fluid between different mechanical components and distant locations. While temperature difference between mechanical components can be quiet large, the temperature difference for transporting liquid can be small. This temperature difference can be useful for monitoring temperature and powering wireless sensors. To this end, a flow thermo-electrochemical generator is recommended (Figure 7.1). The flow thermo-electrochemical generator in addition to power harvesting can also provide cooling.

The Figure 7.1 shows the thermocell around a heat pipe. For initial design standard stainless steel piping can be used. On the interior of piping flexible heaters can be used to simulate a warm fluid. On the exterior of pipe another pipe can be used for electrolyte

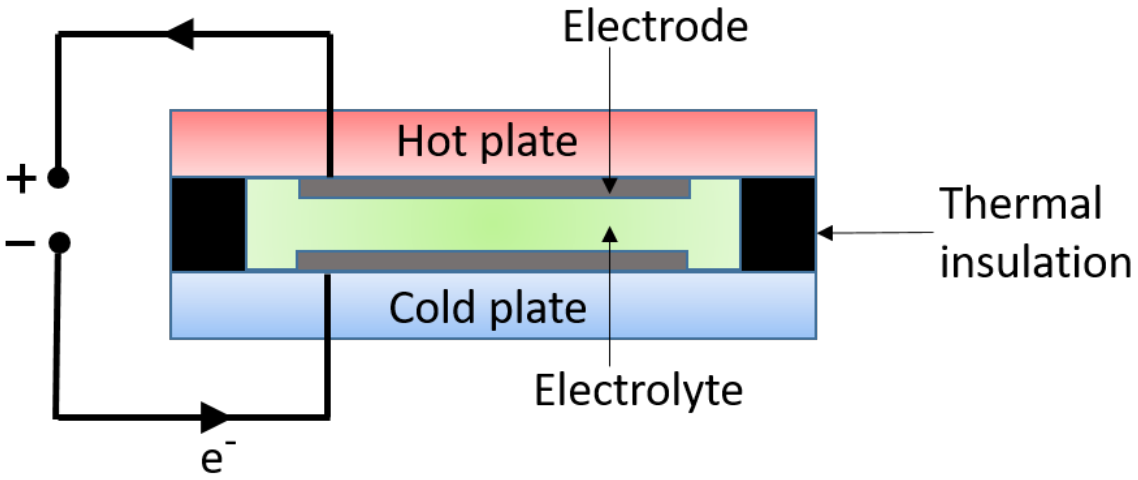

Figure 7.2: Thermo-electrochemical cooler and heater.

flow. For the initial design graphite can be used as electrodes. Electrical insulation is most important to prevent electric short circuit and to ensure that a potential difference is generated with fluid at different temperatures.

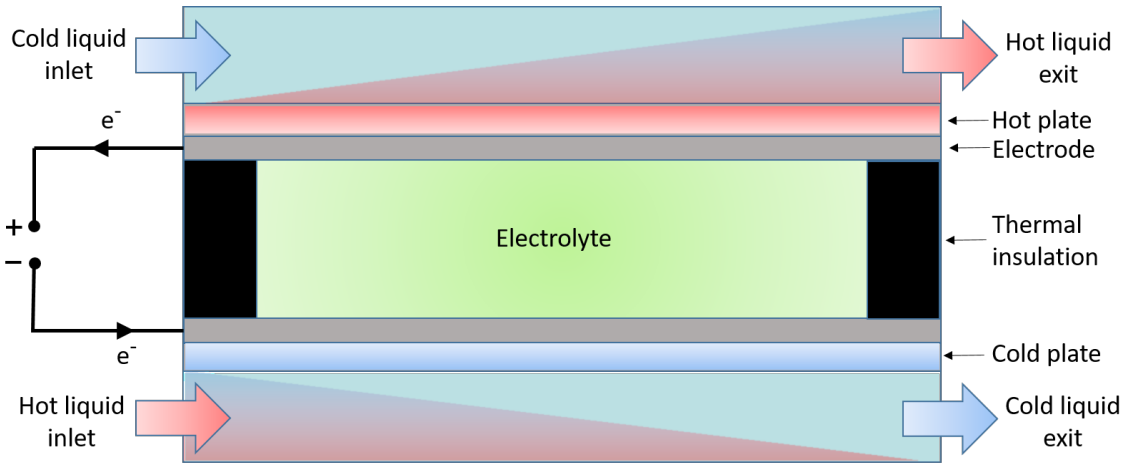

Figure 7.3: Liquid Thermo-electrochemical cooler and heater.

7.2.3 Reverse thermo-electrochemical generator or Thermo-electrochemical cooler and heater

Thermo-electrochemical cells have low efficiencies of converting heat to electricity. However, its reverse cycle is proposed i.e. to converts electricity input to generate temperature

difference. The reversal of cycle will increase temperature of one of the electrodes, the plate attached to it will serve as a heater while the other electrode temperature will reduce and the plate attached to it will serve as a cooler. Both the hot and the cold plate needs to be thermally insulated by a material having low thermal conductivity.

Figure 7.2 provides a schematic that would provide heating and cooling to adjoining surface or air. Reverse thermo-electrochemical generator can also heat and cool liquid flowing over the plates as shown in Figure 7.3. The higher heat capacity of the liquid as compared to gas would help transfer more heat away from the Reverse thermo-electrochemical generator.

Appendices

APPENDIX A

ELECTRONIC SUPPLEMENTARY INFORMATION FOR CHAPTER 4

A.1 Electrochemical impedance spectroscopy fitting parameters

Table A.1: Fitting parameters for electrochemical impedance spectra for increased wt% of PEDOT:PSS in distilled water. The fitting was done using Randles equivalent circuit. R_s is the ohmic resistance; R_{ct} is the interfacial charge transfer resistance; W is the Warburg impedance; C is the double layer capacitance; and σ is the ohmic conductivity of the solution. Distilled water conductivity was measured with Fisher scientific traceable expanded range conductivity meter.

PEDOT:PSS wt%	$R_s(\Omega)$	$R_{ct}(\Omega)$	$W(\Omega s^{-0.5})$	$C(\Omega^{-1}s)$	$\sigma(Sm^{-1})$
0	N/A	N/A	N/A	N/A	1.30E-04
0.025	2.01E+04	1.00E-03	2.42E-06	8.96E-07	1.65E-02
0.05	1.80E+04	1.00E-03	2.47E-06	6.13E-07	2.67E-02
0.075	1.32E+04	1.00E-03	2.52E-06	4.96E-07	3.65E-02
0.1	1.05E+04	1.00E-03	2.50E-06	3.96E-07	4.60E-02
0.125	8.63E+03	1.00E-03	2.52E-06	3.44E-07	5.57E-02
0.15	7.42E+03	1.00E-03	2.53E-06	3.14E-07	6.49E-02

Table A.2: Fitting parameters for electrochemical impedance spectra for increased wt% of PEDOT:PSS, CNT composite. The composition of MWNT:(PEDOT:PSS) 1:4 was added to 0.2 M $Fe(CN)_6^{3-}$/ $Fe(CN)_6^{4-}$. The fitting was done using Randles equivalent circuit. R_s is the ohmic resistance; R_{ct} is the interfacial charge transfer resistance; W is the Warburg impedance; C is the double layer capacitance; and σ is the ohmic conductivity of the solution.

PEDOT:PSS wt%	MWNT wt%	$R_s(\Omega)$	$R_{ct}(\Omega)$	$W(\Omega s^{-0.5})$	$C(\Omega^{-1}s)$	$\sigma(Sm^{-1})$
0	0	47.68	14.75	0.0134	2.03E-06	10.09
0.0025	0.000625	46.57	7.658	0.0135	1.80E-06	10.33
0.0075	0.0001875	46.46	7.718	0.0135	1.81E-06	10.36
0.015	0.00375	46.91	7.68	0.0134	1.77E-06	10.26
0.02	0.005	47.28	7.816	0.0133	1.79E-06	10.18
0.03	0.0075	48.2	4.596	0.0133	1.53E-06	9.98
0.06	0.015	48.24	4.8	0.0131	1.46E-06	9.97

Table A.3: Fitting parameters for electrochemical impedance spectra for increased wt% of PEDOT:PSS, CNT composite. The composition of MWNT:(PEDOT:PSS) 3:1 was added to 0.2 M $Fe(CN)_6^{3-}$/ $Fe(CN)_6^{4-}$. The fitting was done using Randles equivalent circuit. R_s is the ohmic resistance; R_{ct} is the interfacial charge transfer resistance; W is the Warburg impedance; C is the double layer capacitance; and σ is the ohmic conductivity of the solution.

PEDOT:PSS wt%	MWNT wt%	$R_s(\Omega)$	$R_{ct}(\Omega)$	$W(\Omega s^{-0.5})$	$C(\Omega^{-1}s)$	$\sigma(Sm^{-1})$
0	0	47.68	14.75	0.0134	2.03E-06	10.09
0.0025	0.0075	46.64	13.32	0.0137	1.19E-06	10.32
0.0075	0.0225	46.59	10.23	0.0137	1.45E-06	10.33
0.015	0.045	46.33	10.47	0.0136	1.42E-06	10.39
0.02	0.06	46.12	10.67	0.0136	1.14E-06	10.43
0.03	0.09	46.24	10.86	0.0135	1.40E-06	10.41
0.06	0.18	46.86	11.75	0.0132	1.34E-06	10.27

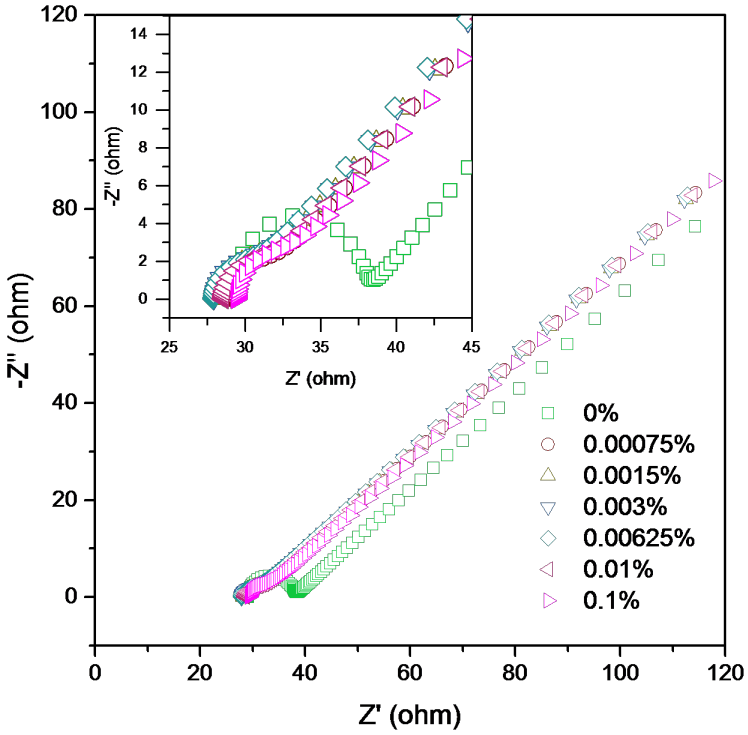

Figure A.1: Electrochemical impedance spectra of increasing PEDOT:PSS (wt%) in 0.4 M $Fe(CN)_6^{3-}$/ $Fe(CN)_6^{4-}$. Inset shows an enlarge scale.

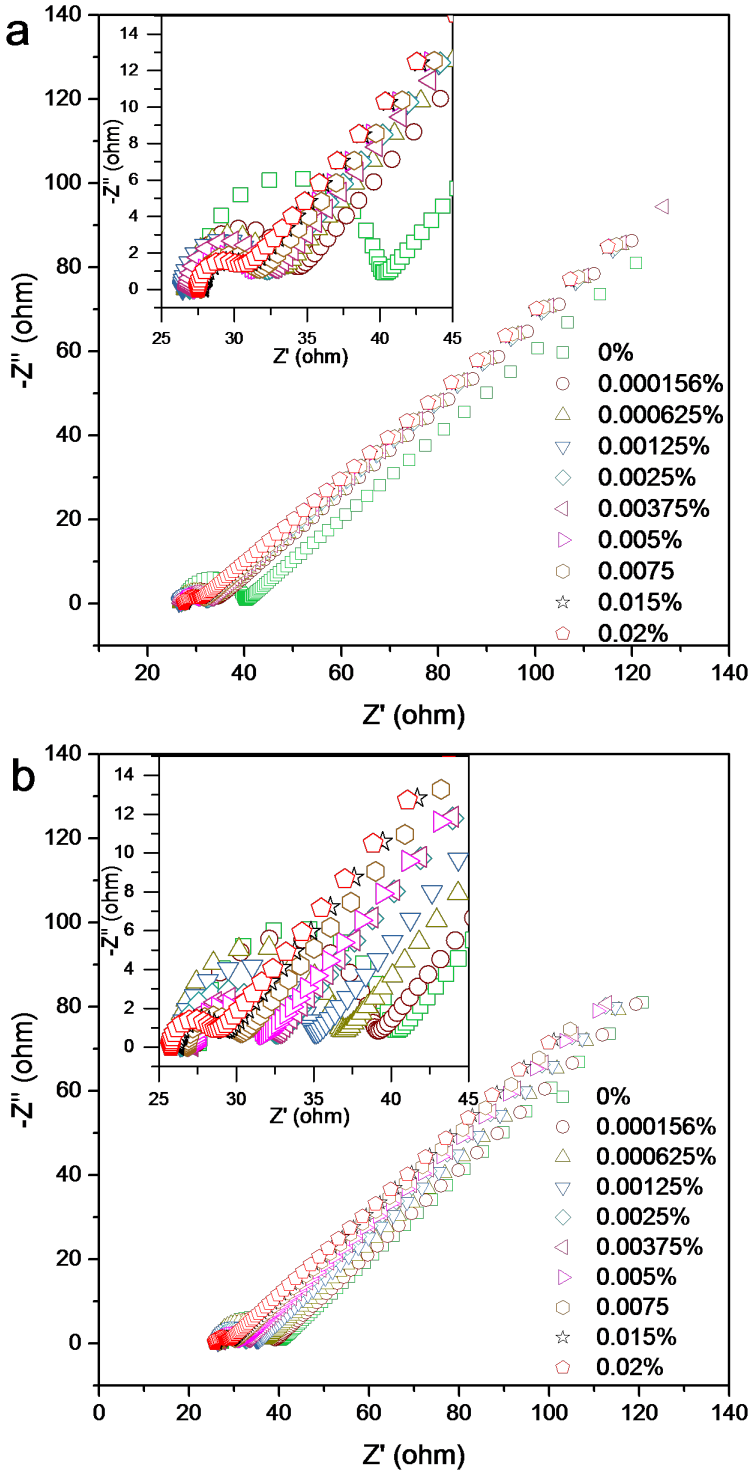

Figure A.2: Electrochemical impedance spectra of increasing MWNT (wt%) on 0.4 M $Fe(CN)_6^{3-}$/ $Fe(CN)_6^{4-}$ using MWNT:(PEDOT:PSS) 1:4 composite(a) , MWNT: (PEDOT:PSS) 3:1 (b). Insets show an enlarge scale

A.2 Cyclic Voltammetry

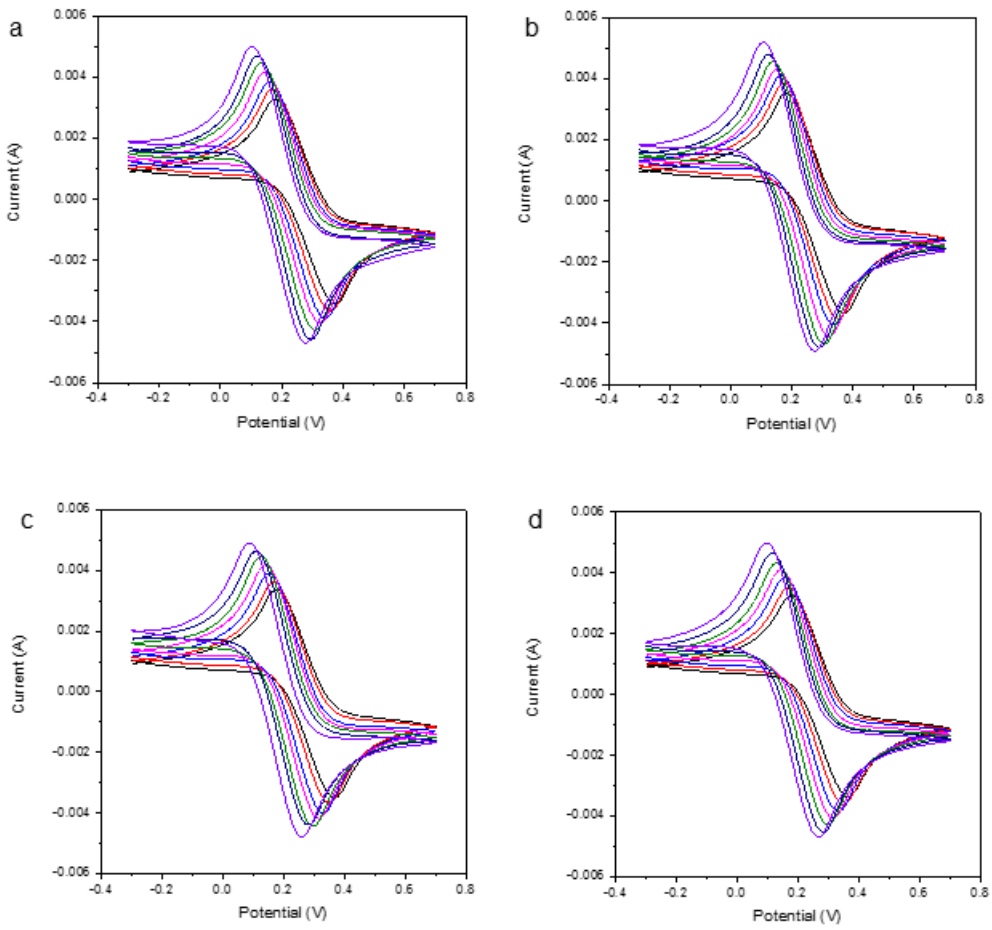

Figure A.3: Cyclic Voltammetry of 0.4 M $Fe(CN)_6^{3-}$/ $Fe(CN)_6^{4-}$ (a), 0.4 M $Fe(CN)_6^{3-}$/ $Fe(CN)_6^{4-}$ + 0.00625 wt% PEDOT:PSS (b), 0.4 M $Fe(CN)_6^{3-}$/ $Fe(CN)_6^{4-}$ + 0.06 wt% PEDOT:PSS + 0.015 wt% MWNT (c), 0.4 M $Fe(CN)_6^{3-}$/ $Fe(CN)_6^{4-}$ + 0.005 wt% PEDOT:PSS + 0.015 wt% MWNT (d) as function isothermal cell temperature 20 ^{o}C (black), 30 ^{o}C (red), 40 ^{o}C (blue), 50 ^{o}C (magenta), 60 ^{o}C (olive), 70 ^{o}C (navy), 80 ^{o}C (violet). As temperature is increased peaks shift to the left and current increases. The half-wave potential also shifts to left (decreases) for (b), (c), (d) compare to (a) as shown in Figure 3.4 of Chapter 4.

APPENDIX B

PROPOSED DESIGN FOR HARVESTING ENERGY FROM WASTE-HEAT IN AN ELECTRIC VEHICLE BATTERY PACK

Effective thermal management of batteries is integral for battery safety. By implementing the technology studied in this paper, in the following manner, we can read out a comprehensive temperature distribution of the coolant simply based off of the voltage and power output at different electrode surface pairs as shown in Figure B.1. This would complement existing safety features found in these battery packs.

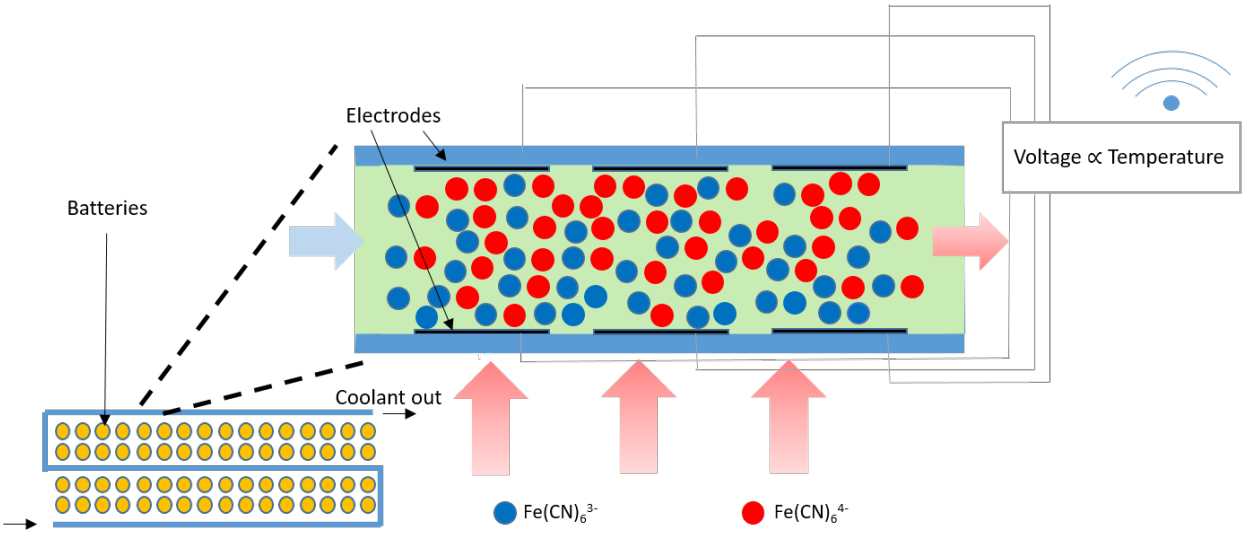

Figure B.1: Bottom left is a typical configuration in battery pack used in electric vehicles. Cell are shown surrounded by pipes carrying coolant. The zoomed in portion of the pipe shows a proposed configuration to harvest energy from waste-heat emitted. In doing so we can sense temperature and communicate the information via a wireless signal.

APPENDIX C

ESTIMATE OF ENERGY HARVESTED IN DATA CENTERS

The amount of energy harvested is estimated by using specification of sever rack used in a typical data center. Each server rack has typically 8-16 cores having CPU of dimension of 54 * 45 mm. For a conservative estimate 8 cores were used for calculation. There are 30 servers present per rack and rack has physical footprint of 11 ft^2. Following table shows the estimate for the amount of energy harvested using thermocells.

	Thermocell Wattage per square meter (A)	Area of CPU in square meter (B)	Wattage per CPU (A*B)	No. of cores Core (C)	Wattage per server (A*B*C)	No. of servers (D)	Wattage per rack (A*B*C*D)	Rack area in square feet (E)	Wattage per square feet(A*B*C*D/E)	Facility size in sqaure feet (F)	Energy harvested in Watts (A*B*C*D*F/E)
Current production	0.049600099	0.00234	0.000116064	8	0.000929	30	0.027855416	11	0.002532311	100000	253.2310519
Best possible	12	0.00234	0.02808	8	0.22464	30	6.7392	11	0.612654545	100000	61265.45455

Figure C.1: Estimate of amount of energy harvested from 100,000 square feet facility.

REFERENCES

[1] I. Statistics, Key world energy statistics, 2016.

[2] B. Petroleum, Bp statistical review of world energy, 2016.

[3] L. Bernstein, P. Bosch, O. Canziani, Z. Chen, R. Christ, and O. Davidson, "Climate change 2007: Synthesis report. summary for policymakers," in Climate change 2007: Synthesis report. Summary for policymakers, IPCC, 2007.

[4] N. R.C.U. C. on America's Climate Choices, Advancing the science of climate change: America's climate choices. National Academies Press, 2010.

[5] D. Joseph and D. Pamela, "Climate change: What it means for us, our children and our grandchildren," MIT Press, 2014.

[6] J. Cook, N. Oreskes, P. T. Doran, W. R. Anderegg, B. Verheggen, E. W. Maibach, J. S. Carlton, S. Lewandowsky, A. G. Skuce, S. A. Green, et al., "Consensus on consensus: A synthesis of consensus estimates on human-caused global warming," Environmental Research Letters, vol. 11, no. 4, p. 048 002, 2016.

[7] K. R. C. Buis Alan; Ramsayer, "A breathing planet, off balance," NASA, Tech. Rep., 2015.

[8] NASA, Giss surface temperature analysis (gistemp), 2017.

[9] J. Hansen, R. Ruedy, M. Sato, and K. Lo, "Global surface temperature change," Reviews of Geophysics, vol. 48, no. 4, 2010.

[10] G. Team et al., Giss surface temperature analysis (gistemp), 2015.

[11] Paris agreement, fccc/cp/2015/l.9/rev.1, 2015.

[12] G. P. Peters, R. M. Andrew, T. Boden, J. G. Canadell, P. Ciais, C. Le Quéré, G. Marland, M. R. Raupach, and C. Wilson, "The challenge to keep global warming below 2 c," Nature Climate Change, vol. 3, no. 1, pp. 4–6, 2013.

[13] P. Friedlingstein, S. Solomon, G. Plattner, R. Knutti, P. Ciais, and M. Raupach, "Long-term climate implications of twenty-first century options for carbon dioxide emission mitigation," Nature Climate Change, vol. 1, no. 9, pp. 457–461, 2011.

[14] M. Jakob, G. Luderer, J. Steckel, M. Tavoni, and S. Monjon, "Time to act now? assessing the costs of delaying climate measures and benefits of early action," Climatic Change, vol. 114, no. 1, pp. 79–99, 2012.

[15] L. Clarke, J. Edmonds, V. Krey, R. Richels, S. Rose, and M. Tavoni, "International climate policy architectures: Overview of the emf 22 international scenarios," Energy Economics, vol. 31, S64–S81, 2009.

[16] J. van Vliet, M. van den Berg, M. Schaeffer, D. P. van Vuuren, M. Den Elzen, A. F. Hof, A. M. Beltran, and M. Meinshausen, "Copenhagen accord pledges imply higher costs for staying below 2 c warming," Climatic Change, vol. 113, no. 2, pp. 551–561, 2012.

[17] J. Rogelj, W. Hare, J. Lowe, D. P. Van Vuuren, K. Riahi, B. Matthews, T. Hanaoka, K. Jiang, and M. Meinshausen, "Emission pathways consistent with a 2 [thinsp][deg] c global temperature limit," Nature Climate Change, vol. 1, no. 8, pp. 413–418, 2011.

[18] C. Wilson, A. Grubler, K. S. Gallagher, and G. F. Nemet, "Marginalization of end-use technologies in energy innovation for climate protection," Nature Climate Change, vol. 2, no. 11, pp. 780–788, 2012.

[19] G. B. Forbes, Human body composition: Growth, aging, nutrition, and activity. Springer Science & Business Media, 2012.

[20] R. J. Goldstick and A. Thumann, "Principles of waste heat recovery," 1985.

[21] W. C. Turner and S. Doty, Energy management handbook. The Fairmont Press, Inc., 2012.

[22] P. F. Baldasaro, E. J. Brown, D. M. Depoy, B. C. Campbell, and J. R. Parrington, "Experimental assessment of low temperature voltaic energy conversion," in The first NREL conference on thermophotovoltaic generation of electricity, AIP Publishing, vol. 321, 1995, pp. 29–43.

[23] G. Hatsopoulos and E. Gyftopoulos, "Thermionic energy conversion. volume ii. theory, technology, and application," MIT Press, Cambridge, MA, Tech. Rep., 1979.

[24] A Datas and A Martí, "Thermophotovoltaic energy in space applications: Review and future potential," Solar Energy Materials and Solar Cells, vol. 161, pp. 285–296, 2017.

[25] R. Venkatasubramanian, E. Siivola, T. Colpitts, and B. O'quinn, "Thin-film thermoelectric devices with high room-temperature figures of merit," Nature, vol. 413, no. 6856, pp. 597–602, 2001.

[26] G. J. Snyder and E. S. Toberer, "Complex thermoelectric materials.," Nature materials, vol. 7, no. 2, pp. 105–114, 2008.

[27] G. L. Bennett, J. J. Lombardo, and B. J. Rock, "U.s. radioisotope thermoelectric generator space operating experience (june 1961-december 1982)," in 18th Intersociety Energy Conversion Engineering Conference Proceedings, Florida, 1983.

[28] G. L. Bennett and E. Skrabek, "Power performance of us space radioisotope thermoelectric generators," in Thermoelectrics, 1996., Fifteenth International Conference on, IEEE, 1996, pp. 357–372.

[29] G. Mahan, B. Sales, and J. Sharp, "Thermoelectric materials: New approaches to an old problem," Physics Today, vol. 50, no. 3, 1997.

[30] G Chen, M. Dresselhaus, G Dresselhaus, J.-P. Fleurial, and T Caillat, "Recent developments in thermoelectric materials," International Materials Reviews, 2013.

[31] M. Bonetti, S. Nakamae, M. Roger, and P. Guenoun, "Huge Seebeck coefficients in nonaqueous electrolytes," Journal of Chemical Physics, vol. 134, no. 11, pp. 1–9, 2011. arXiv: 1102.2425.

[32] Y. Mua and Quickenden, "Power Conversion Efficiency, Electrode Separation, and Overpotential in the Ferricyanide/Ferrocyanide Thermogalvanic Cell," Journal of The Electrochemical Society, vol. 143, no. 8, p. 2558, 1996.

[33] T. J. Abraham, D. R. MacFarlane, R. H. Baughman, N. Li, Y. Chen, and J. M. Pringle, "Protic ionic liquid-based thermoelectrochemical cells for the harvesting of waste heat.," in MRS Proceedings, Cambridge Univ Press, vol. 1575, 2013, mrss13–1575.

[34] T. Quickenden and C. Vernon, "Thermogalvanic conversion of heat to electricity," Solar Energy, vol. 36, no. 1, pp. 63–72, 1986.

[35] A. J. Debethune, T. S. Licht, and N Swendeman, "The temperature coefficients of electrode potentials - the isothermal and thermal coefficients - the standard ionic entropy of electrochemical transport of the hydrogen ion," Journal of the Electrochemical Society, vol. 106, no. 7, pp. 616–625, 1959.

[36] E. L. Yee, R. J. Cave, K. L. Guyer, P. D. Tyma, and M. J. Weaver, "A survey of ligand effects upon the reaction entropies of some transition metal redox couples," Journal of the American Chemical Society, vol. 101, no. 5, pp. 1131–1137, 1979.

[37] J. T. Hupp and M. J. Weaver, "Solvent, Ligand, and Ionic Charge Effects on Reaction Entropies for Simple Transition-Metal Redox Couples," Inorganic Chemistry, no. 23, pp. 3639–3644, 1984.

[38] M. Armand, F. Endres, D. R. MacFarlane, H. Ohno, and B. Scrosati, "Ionic-liquid materials for the electrochemical challenges of the future," Nature materials, vol. 8, no. 8, pp. 621–629, 2009.

[39] D. R. MacFarlane, M. Forsyth, P. C. Howlett, M. Kar, S. Passerini, J. M. Pringle, H. Ohno, M. Watanabe, F. Yan, W. Zheng, et al., "Ionic liquids and their solid-state analogues as materials for energy generation and storage," Nature Reviews Materials, vol. 1, p. 15 005, 2016.

[40] T. Kim, J. S. Lee, G. Lee, H. Yoon, J. Yoon, T. J. Kang, and Y. H. Kim, "High thermopower of ferri/ferrocyanide redox couple in organic-water solutions," Nano Energy, vol. 31, pp. 160–167, 2017.

[41] H. Zhou, T. Yamada, and N. Kimizuka, "Supramolecular thermo-electrochemical cells: Enhanced thermoelectric performance by host–guest complexation and salt-induced crystallization," Journal of the American Chemical Society, vol. 138, no. 33, pp. 10 502–10 507, 2016.

[42] T. J. Abraham, D. R. MacFarlane, and J. M. Pringle, "Seebeck coefficients in ionic liquids–prospects for thermo-electrochemical cells," Chemical communications, vol. 47, no. 22, pp. 6260–6262, 2011.

[43] P. F. Salazar, S. T. Stephens, A. H. Kazim, J. Pringle, and B. a. Cola, "Enhanced thermo-electrochemical power using carbon nanotube additives in ionic liquid redox electrolytes," J. Mater. Chem. A, vol. 00, pp. 1–7, 2014.

[44] P. F. Salazar, K. J. Chan, S. T. Stephens, and B. A. Cola, "Enhanced electrical conductivity of imidazolium-based ionic liquids mixed with carbon nanotubes: A spectroscopic study," Journal of The Electrochemical Society, vol. 161, no. 9, H481–H486, 2014.

[45] J. J. Black, T. Murphy, R. Atkin, A. Dolan, and L. Aldous, "The thermoelectrochemistry of lithium–glyme solvate ionic liquids: Towards waste heat harvesting," Physical Chemistry Chemical Physics, vol. 18, no. 30, pp. 20 768–20 777, 2016.

[46] V. Zinovyeva, S. Nakamae, M. Bonetti, and M. Roger, "Enhanced thermoelectric power in ionic liquids," ChemElectroChem, vol. 1, no. 2, pp. 426–430, 2014.

[47] R. Hu, B. A. Cola, N. Haram, J. N. Barisci, S. Lee, S. Stoughton, G. Wallace, C. Too, M. Thomas, A. Gestos, M. E. Dela Cruz, J. P. Ferraris, A. A. Zakhidov, and R. H. Baughman, "Harvesting waste thermal energy using a carbon-nanotube-based thermo-electrochemical cell," Nano Letters, vol. 10, no. 3, pp. 838–846, 2010.

[48] M. S. Romano, S. Gambhir, J. M. Razal, A. Gestos, G. G. Wallace, and J. Chen, "Novel carbon materials for thermal energy harvesting," Journal of Thermal Analysis and Calorimetry, vol. 109, no. 3, pp. 1229–1235, 2012.

[49] H. Im, T. Kim, H. Song, J. Choi, J. S. Park, R. Ovalle-Robles, H. D. Yang, K. D. Kihm, R. H. Baughman, H. H. Lee, T. J. Kang, and Y. H. Kim, "High-efficiency electrochemical thermal energy harvester using carbon nanotube aerogel sheet electrodes," Nature Communications, vol. 7, p. 10 600, 2016.

[50] M. S. Romano, N. Li, D. Antiohos, J. M. Razal, A. Nattestad, S. Beirne, S. Fang, Y. Chen, R. Jalili, G. G. Wallace, et al., "Carbon nanotube–reduced graphene oxide composites for thermal energy harvesting applications," Advanced Materials, vol. 25, no. 45, pp. 6602–6606, 2013.

[51] T. J. Kang, S. Fang, M. E. Kozlov, C. S. Haines, N. Li, Y. H. Kim, Y. Chen, and R. H. Baughman, "Electrical Power From Nanotube and Graphene Electrochemical Thermal Energy Harvesters," Advanced Functional Materials, vol. 22, no. 3, pp. 477–489, 2012.

[52] H. Im, T. J. Kang, D. W. Kim, and Y. H. Kim, "Development of thin-film thermo-electrochemical cell for harvesting waste thermal energy," Journal of the Korean Society for Aeronautical & Space Sciences, vol. 40, no. 11, pp. 1010–1015, 2012.

[53] A. Gunawan, H. Li, C.-H. Lin, D. a. Buttry, V. Mujica, R. a. Taylor, R. S. Prasher, and P. E. Phelan, "The amplifying effect of natural convection on power generation of thermogalvanic cells," International Journal of Heat and Mass Transfer, vol. 78, pp. 423–434, 2014.

[54] A. Gunawan, N. W. Fette, and P. E. Phelan, "Thermogalvanic waste heat recovery system in automobiles," in ASME 2015 Power Conference, collocated with the ASME 2015 9th International Conference on Energy Sustainability, the ASME 2015 13th International Conference on Fuel Cell Science, Engineering and Technology, and the ASME 2015 Nuclear Forum, American Society of Mechanical Engineers, 2015, V001T11A002–V001T11A002.

[55] S. Uhl, E. Laux, T. Journot, L. Jeandupeux, J. Charmet, and H. Keppner, "Development of Flexible Micro-Thermo-electrochemical Generators Based on Ionic Liquids," Journal of Electronic Materials, vol. 43, no. 10, pp. 3758–3764, 2014.

[56] H. Im, H. G. Moon, J. S. Lee, I. Y. Chung, T. J. Kang, and Y. H. Kim, "Flexible thermocells for utilization of body heat," Nano Research, vol. 7, no. 4, pp. 1–10, 2014.

[57] A. R. Boccaccini, J. Cho, J. A. Roether, B. J. Thomas, E. J. Minay, and M. S. Shaffer, "Electrophoretic deposition of carbon nanotubes," Carbon, vol. 44, no. 15, pp. 3149–3160, 2006.

[58] W. Qian, M. Cao, F. Xie, and C. Dong, "Thermo-Electrochemical Cells Based on Carbon Nanotube Electrodes by Electrophoretic Deposition," Nano-Micro Letters, 2016.

[59] A. A. Talin, K. A. Dean, S. M. O'rourke, B. F. Coll, M. Stainer, and R. Subrahmanyan, Fed cathode structure using electrophoretic deposition and method of fabrication, US Patent 6,902,658, 2005.

[60] S. Oh, J Zhang, Y Cheng, H Shimoda, and O Zhou, "Liquid-phase fabrication of patterned carbon nanotube field emission cathodes," Applied Physics Letters, vol. 84, no. 19, pp. 3738–3740, 2004.

[61] H. Zhao, H. Song, Z. Li, G. Yuan, and Y. Jin, "Electrophoretic deposition and field emission properties of patterned carbon nanotubes," Applied surface science, vol. 251, no. 1, pp. 242–244, 2005.

[62] L. Chen, H. Xie, and W. Yu, "Multi-walled carbon nanotube/silver nanoparticles used for thermal transportation," Journal of Materials Science, vol. 47, no. 14, pp. 5590–5595, 2012.

[63] R.-X. Dong, C.-T. Liu, K.-C. Huang, W.-Y. Chiu, K.-C. Ho, and J.-J. Lin, "Controlling formation of silver/carbon nanotube networks for highly conductive film surface," ACS applied materials & interfaces, vol. 4, no. 3, pp. 1449–1455, 2012.

[64] W. Qian, M. Li, L. Chen, J. Zhang, and C. Dong, "Improving thermo-electrochemical cell performances by constructing Ag-MgO-CNTs nanocomposite electrodes," RSC Adv., 2015.

[65] K. M. Bae, H. D. Yang, L. T. Tufa, and T. J. Kang, "Thermobattery based on cnt coated carbon textile and thermoelectric electrolyte," International Journal of Precision Engineering and Manufacturing, vol. 16, no. 7, pp. 1245–1250, 2015.

[66] H. D. Yang, L. T. Tufa, K. M. Bae, and T. J. Kang, "A tubing shaped, flexible thermal energy harvester based on a carbon nanotube sheet electrode," Carbon, vol. 86, pp. 118–123, 2015.

[67] P. F. Salazar, S. Kumar, and B. a. Cola, "Nitrogen- and Boron-Doped Carbon Nanotube Electrodes in a Thermo-Electrochemical Cell," Journal of The Electrochemical Society, vol. 159, no. 5, B483, 2012.

[68] T. J. Abraham, N. Tachikawa, D. R. MacFarlane, and J. M. Pringle, "Investigation of the kinetic and mass transport limitations in thermoelectrochemical cells with different electrode materials.," Physical chemistry chemical physics : PCCP, vol. 16, no. 6, pp. 2527–32, 2014.

[69] A. J. Bard, L. R. Faulkner, J. Leddy, and C. G. Zoski, Electrochemical methods: Fundamentals and applications. Wiley New York, 1980, vol. 2.

[70] A. H. Kazim and B. A. Cola, "Electrochemical Characterization of Carbon Nanotube and Poly (3,4-ethylenedioxythiophene)Poly(styrenesulfonate) Composite Aqueous Electrolyte for Thermo-Electrochemical Cells," Journal of The Electrochemical Society, vol. 163, no. 8, F867–F871, 2016.

[71] C. Liu, H. Lee, Y.-H. Chang, and S.-P. Feng, "The Study of Electrical Conductivity and Diffusion Behavior of Water-Based and Ferro/Ferricyanide-Electrolyte-Based Alumina Nanofluids," Journal of Colloid and Interface Science, 2016.

[72] P. F. Salazar, "Modeling and Experiments To Develop Thermo- Development of Thermo-Electrochemical Cells," no. August, 2014.

[73] W. Kobayashi, A. Kinoshita, and Y. Moritomo, "Seebeck effect in a battery-type thermocell," Applied Physics Letters, vol. 107, no. 7, 2015.

[74] M. Bonetti, S. Nakamae, B. T. Huang, T. J. Salez, C. Wiertel-Gasquet, and M. Roger, "Thermoelectric energy recovery at ionic-liquid/electrode interface," The Journal of chemical physics, vol. 142, no. 24, p. 244 708, 2015.

[75] S. W. Lee, Y. Yang, H.-W. Lee, H. Ghasemi, D. Kraemer, G. Chen, and Y. Cui, "An electrochemical system for efficiently harvesting low-grade heat energy," Nature communications, vol. 5, 2014.

[76] T. Hirai, K. Shindo, and T. Ogata, "Charge and discharge characteristics of thermochargeable galvanic cells with an [fe (cn) 6] 4-/[fe (cn) 6] 3- redox couple," Journal of the Electrochemical Society, vol. 143, no. 4, pp. 1305–1313, 1996.

[77] T. Ikeshoji, S. Kimura, F. N. B. de Nahui, and M. Yoneya, "Computer analysis of natural convection in thin-layer thermocells with a soluble redox couple: Part 1. method and the unsteady problem," Journal of electroanalytical chemistry and interfacial electrochemistry, vol. 307, no. 1-2, pp. 29–45, 1991.

[78] T. Ikeshoji, F. N. B. de Nahui, S. Kimura, and M. Yoneya, "Computer analysis on natural convection in thin-layer thermocells with a soluble redox couple: Part 2. ei relation, electric power, heat flux and electrochemical heat pump," Journal of electroanalytical chemistry and interfacial electrochemistry, vol. 312, no. 1-2, pp. 43–56, 1991.

[79] A. V. Sokirko, "Theoretical study of thermogalvanic cells in steady state," Electrochimica acta, vol. 39, no. 4, pp. 597–609, 1994.

[80] E. D. Eastman, "Thermodynamics of non-isothermal systems," Journal of the American Chemical Society, vol. 48, pp. 1482–1493, 1926.

[81] G. R. Salvi and A. J. DeBethune, "The Temperature Coefficients of Electrode Potentials," Journal of The Electrochemical Society, vol. 108, p. 672, 1961.

[82] B. Burrows, "Discharge behavior of redox thermogalvanic cells," Journal of The Electrochemical Society, vol. 123, no. 2, pp. 154–159, 1976.

[83] T. I. Quickenden, "A Review of Power Generation in Aqueous Thermogalvanic Cells," Journal of The Electrochemical Society, vol. 142, no. November, p. 3985, 1995.

[84] P Blanc and C Madic, "Thermoelectric properties of m 4+/m 3+ and mo 2 2t/mo 2+ redox couples of neptunium and plutonium in aqueous hclo 4 and hno 3 media," Inorganica chimica acta, vol. 95, no. 3, pp. 141–145, 1984.

[85] T. Hirai, K. Shindo, and T. Ogata, "Charge and discharge characteristics of thermochargeable galvanic cells with an [fe (cn) 6] 4-/[fe (cn) 6] 3- redox couple," Journal of the Electrochemical Society, vol. 143, no. 4, pp. 1305–1313, 1996.

[86] Y. V. Kuz'minskii and A. Andriiko, "Thermal analysis of electrochemical reactions: Part ii. the non-stationary temperature wave methoda method for the determination of peltier heats at the electrode/molten electrolyte interface," Journal of electroanalytical chemistry and interfacial electrochemistry, vol. 252, no. 1, pp. 39–52, 1988.

[87] Y. Kuzminskii, V. Zasukha, and G. Kuzminskaya, "Thermoelectric effects in electrochemical systems. nonconventional thermogalvanic cells," Journal of power sources, vol. 52, no. 2, pp. 231–242, 1994.

[88] E. Helfand and J. G. Kirkwood, "Theory of the heat of transport of electrolytic solutions," The Journal of Chemical Physics, vol. 32, no. 3, pp. 857–866, 1960.

[89] D. R. MacFarlane, N. Tachikawa, M. Forsyth, J. M. Pringle, P. C. Howlett, G. D. Elliott, J. H. Davis, M. Watanabe, P. Simon, and C. A. Angell, "Energy applications of ionic liquids," Energy & Environmental Science, vol. 7, no. 1, p. 232, 2014.

[90] H. Chum and R. Osteryoung, "Review of Thermally Regenerative Electrochemical Systems," Report SERI/TR-332-416, vol. 2, 1981.

[91] T. M. Tritt, H. Böttner, and L. Chen, "Thermoelectrics: Direct solar thermal energy conversion," MRS bulletin, vol. 33, no. 04, pp. 366–368, 2008.

[92] "Combined heat and power, waste heat, and district energy," U.S. Department of Energy, Tech. Rep., 2011.

[93] C. B. Vining, "An inconvenient truth about thermoelectrics.," Nature materials, vol. 8, no. 2, pp. 83–5, 2009.

[94] a Gunawan, C. H. Lin, D. a. Buttry, V Mujica, R. a. Taylor, R. S. Prasher, and P. E. Phelan, "Liquid Thermoelectrics: Review of Recent And Limited New Data of Thermogalvanic Cell Experiments," Nanoscale and Microscale Thermophysical Engineering, vol. 17, no. 4, pp. 304–323, 2013.

[95] D. Rooney, J. Jacquemin, and R. Gardas, "Thermophysical properties of ionic liquids," in Ionic liquids, Springer, 2009, pp. 185–212.

[96] M. Galinski, A. Lewandowski, and I. Stkepniak, "Ionic liquids as electrolytes," Electrochimica Acta, vol. 51, no. 26, pp. 5567–5580, 2006.

[97] T. Katakabe, R. Kawano, and M. Watanabe, "Acceleration of Redox Diffusion and Charge-Transfer Rates in an Ionic Liquid with Nanoparticle Addition," Electrochemical and Solid-State Letters, vol. 10, no. 6, F23, 2007.

[98] H. F. Lee, J. L. Wu, P. Y. Hsu, Y. L. Tung, F. Y. Ouyang, and J. J. Kai, "Enhanced photovoltaic performance and long-term stability of dye-sensitized solar cells by incorporating SiO2 nanoparticles in binary ionic liquid electrolytes," Thin Solid Films, vol. 529, pp. 2–6, 2013.

[99] C. P. Lee, K. M. Lee, P. Y. Chen, and K. C. Ho, "On the addition of conducting ceramic nanoparticles in solvent-free ionic liquid electrolyte for dye-sensitized solar cells," Solar Energy Materials and Solar Cells, vol. 93, no. 8, pp. 1411–1416, 2009.

[100] T. Kato, T. Kado, S. Tanaka, A. Okazaki, and S. Hayase, "Quasi-Solid Dye-Sensitized Solar Cells Containing Nanoparticles Modified with Ionic Liquid-Type Molecules," Journal of The Electrochemical Society, vol. 153, no. 3, A626, 2006.

[101] Y. Dror, W. Pyckhout-Hintzen, and Y. Cohen, "Conformation of Polymers Dispersing Single-Walled Carbon Nanotubes in Water: A Small-Angle Neutron Scattering Study," Macromolecules, vol. 38, pp. 7828–7836, 2005.

[102] J. C. Grunlan, L. Liu, and O. Regev, "Weak polyelectrolyte control of carbon nanotube dispersion in water.," Journal of colloid and interface science, vol. 317, pp. 346–9, 2008.

[103] J. Ouyang, Q. Xu, C.-W. Chu, Y. Yang, G. Li, and J. Shinar, "On the mechanism of conductivity enhancement in poly (3, 4-ethylenedioxythiophene): Poly (styrene sulfonate) film through solvent treatment," Polymer, vol. 45, no. 25, pp. 8443–8450, 2004.

[104] O. Matarredona, H. Rhoads, Z. Li, J. H. Harwell, L. Balzano, and D. E. Resasco, "Dispersion of single-walled carbon nanotubes in aqueous solutions of the anionic surfactant naddbs," The Journal of Physical Chemistry B, vol. 107, no. 48, pp. 13 357–13 367, 2003.

[105] V. C. Moore, M. S. Strano, E. H. Haroz, R. H. Hauge, R. E. Smalley, J. Schmidt, and Y. Talmon, "Individually suspended single-walled carbon nanotubes in various surfactants," Nano letters, vol. 3, no. 10, pp. 1379–1382, 2003.

[106] J. N. Coleman, U. Khan, W. J. Blau, and Y. K. Gunko, "Small but strong: A review of the mechanical properties of carbon nanotube–polymer composites," Carbon, vol. 44, no. 9, pp. 1624–1652, 2006.

[107] B. McCarthy, J. N. Coleman, R. Czerw, a. B. Dalton, M. in het Panhuis, a. Maiti, a. Drury, P. Bernier, J. B. Nagy, B. Lahr, H. J. Byrne, D. L. Carroll, and W. J. Blau, "A Microscopic and Spectroscopic Study of Interactions between Carbon Nanotubes and a Conjugated Polymer," The Journal of Physical Chemistry B, vol. 106, no. 9, pp. 2210–2216, 2002.

[108] C. Yu, K. Choi, L. Yin, and J. C. Grunlan, "Light-weight flexible carbon nanotube based organic composites with large thermoelectric power factors," ACS Nano, vol. 5, no. 10, pp. 7885–7892, 2011.

[109] W. Hong, Y. Xu, G. Lu, C. Li, and G. Shi, "Transparent graphene/PEDOTPSS composite films as counter electrodes of dye-sensitized solar cells," Electrochemistry Communications, vol. 10, no. 10, pp. 1555–1558, 2008.

[110] M. Bhagavathi Achari, V. Elumalai, N. Vlachopoulos, M. Safdari, J. Gao, J. M. Gardner, and L. Kloo, "A quasi-liquid polymer-based cobalt redox mediator electrolyte for dye-sensitized solar cells.," Physical chemistry chemical physics : PCCP, vol. 15, no. 40, pp. 17 419–25, 2013.

[111] D. J. Yun, K. Hong, S. H. Kim, W. M. Yun, J. Y. Jang, W. S. Kwon, C. E. Park, and S. W. Rhee, "Multiwall carbon nanotube and poly(3,4-ethylenedioxythiophene): Polystyrene sulfonate (PEDOT:PSS) composite films for transistor and inverter devices," ACS Applied Materials and Interfaces, vol. 3, no. 1, pp. 43–49, 2011.

[112] J. Park, A. Lee, Y. Yim, and E. Han, "Electrical and thermal properties of PEDOT:PSS films doped with carbon nanotubes," Synthetic Metals, vol. 161, no. 5-6, pp. 523–527, 2011.

[113] N. G. Tsierkezos, "Cyclic voltammetric studies of ferrocene in nonaqueous solvents in the temperature range from 248.15 to 298.15 K," Journal of Solution Chemistry, vol. 36, no. 3, pp. 289–302, 2007.

[114] M. J. O'Connell, P. Boul, L. M. Ericson, C. Huffman, Y. Wang, E. Haroz, C. Kuper, J. Tour, K. D. Ausman, and R. E. Smalley, "Reversible water-solubilization of single-walled carbon nanotubes by polymer wrapping," Chemical Physics Letters, vol. 342, no. 3-4, pp. 265–271, 2001.

[115] M. Yang, V. Koutsos, and M. Zaiser, "Interactions between polymers and carbon nanotubes: A molecular dynamics study," Journal of Physical Chemistry B, vol. 109, no. 20, pp. 10 009–10 014, 2005.

[116] M. Wong, M. Paramsothy, X. Xu, Y. Ren, S. Li, and K. Liao, "Physical interactions at carbon nanotube-polymer interface," Polymer, vol. 44, pp. 7757–7764, 2003.

[117] K. Liao and S. Li, "Interfacial characteristics of a carbon nanotubepolystyrene composite system," Applied Physics Letters, vol. 79, no. 25, p. 4225, 2001.

[118] N. G. Tsierkezos and U. Ritter, "Electrochemical and thermodynamic properties of hexacyanoferrate(II)/(III) redox system on multi-walled carbon nanotubes," Journal of Chemical Thermodynamics, vol. 54, pp. 35–40, 2012.

[119] T. Starner, "Human-powered wearable computing," IBM systems Journal, vol. 35, no. 3.4, pp. 618–629, 1996.

[120] "U.S. energy flow trends 2013," Lawrence Livermore National Laboratory, Tech. Rep., 2013.

[121] S. Chu and A. Majumdar, "Opportunities and challenges for a sustainable energy future," Nature, vol. 488, no. 7411, pp. 294–303, 2012.

[122] S. K. Ratkje, T. Ikeshoji, and K. Syverud, "Heat and internal energy changes at electrodes and junctions in thermocells," Journal of The Electrochemical Society, vol. 137, no. 7, pp. 2088–2095, 1990.

[123] J. Agar, "Thermogalvanic cells in advances in electrochemistry and electrochemical engineering, vol.," P. Delahay, Interscience Publ., New York, 1963.

[124] T. J. Abraham, D. R. MacFarlane, and J. M. Pringle, "High Seebeck coefficient redox ionic liquid electrolytes for thermal energy harvesting," Energy & Environmental Science, vol. 6, no. 9, p. 2639, 2013.

[125] A. I. Jewett, Z. Zhuang, and J.-E. Shea, "Moltemplate a coarse-grained model assembly tool," Biophysical Journal, vol. 104, no. 2, 169a, 2013.

[126] H. Berendsen, J. Grigera, and T. Straatsma, "The missing term in effective pair potentials," Journal of Physical Chemistry, vol. 91, no. 24, pp. 6269–6271, 1987.

[127] G. Prampolini, P. Yu, S. Pizzanelli, I. Cacelli, F. Yang, J. Zhao, and J. Wang, "Structure and dynamics of ferrocyanide and ferricyanide anions in water and heavy water: An insight by MD simulations and 2D IR spectroscopy," The Journal of Physical Chemistry B, vol. 118, no. 51, pp. 14 899–14 912, 2014.

[128] W. Humphrey, A. Dalke, and K. Schulten, "Vmd: Visual molecular dynamics," Journal of molecular graphics, vol. 14, no. 1, pp. 33–38, 1996.

[129] K. Ando, "Solvent nuclear quantum effects in electron transfer reactions. III. Metal ions in water. Solute size and ligand effects," The Journal of Chemical Physics, vol. 114, no. 21, pp. 9470–9477, 2001.

[130] H. F. Martiniano and B. J. C. Cabral, "Structure and electronic properties of a strong dipolar liquid: Born–Oppenheimer molecular dynamics of liquid hydrogen cyanide," Chemical Physics Letters, vol. 555, pp. 119–124, 2013.

[131] S. H. Lee and J. C. Rasaiah, "Molecular dynamics simulation of ionic mobility. 1. Alkali metal cations in water at 25○ C," The Journal of chemical physics, vol. 101, no. 8, pp. 6964–6974, 1994.

[132] S. Plimpton, "Fast parallel algorithms for short-range molecular dynamics," Journal of Computational Physics, vol. 117, no. 1, pp. 1–19, 1995.

[133] R. W. Hockney and J. W. Eastwood, Computer simulation using particles. CRC Press, 1988.

[134] J.-P. Ryckaert, G. Ciccotti, and H. J. Berendsen, "Numerical integration of the cartesian equations of motion of a system with constraints: Molecular dynamics of n-alkanes," Journal of Computational Physics, vol. 23, no. 3, pp. 327–341, 1977.

[135] M. Levesque, V. Sarou-Kanian, M. Salanne, M. Gobet, H. Groult, C. Bessada, P. A. Madden, and A.-L. Rollet, "Structure and dynamics in yttrium-based molten

rare earth alkali fluorides," The Journal of chemical physics, vol. 138, no. 18, p. 184 503, 2013.

[136] L. Zhang, T. Kim, N. Li, T. J. Kang, J. Chen, J. M. Pringle, M. Zhang, A. H. Kazim, S. Fang, C. Haines, et al., "High power density electrochemical thermocells for inexpensively harvesting low-grade thermal energy," Advanced Materials, 2017.

[137] S. K. Sanyal, "Future of geothermal energy," in Proceedings, thirty-fifth workshop on geothermal reservoir engineering, SGP-TR-188, 2010, pp. 1–3.

[138] "Ocean thermal energy conversion: An overview," NREL, Tech. Rep., 1989.

[139] "Americas data centers are wasting huge amounts of energy," Natural Resources Defense Council, Tech. Rep., 2014.

[140] G. I. Meijer, "Cooling energy-hungry data centers," Science, vol. 328, pp. 318–319, 2010.

[141] H. Zhang, S. Shao, H. Xu, H. Zou, and C. Tian, "Free cooling of data centers: A review," Renewable and Sustainable Energy Reviews, vol. 35, pp. 171–182, 2014.

[142] S. Alkharabsheh, J. Fernandes, B. Gebrehiwot, D. Agonafer, K. Ghose, A. Ortega, Y. Joshi, and B. Sammakia, "A Brief Overview of Recent Developments in Thermal Management in Data Centers," Journal of Electronic Packaging, vol. 137, no. 4, p. 040 801, 2015.

[143] I. Stark, "Invited talk: Thermal energy harvesting with thermo life," in International Workshop on Wearable and Implantable Body Sensor Networks (BSN), IEEE, 2006, pp. 19–22.

[144] E. Barbier, "Geothermal energy technology and current status: An overview," Renewable and Sustainable Energy Reviews, vol. 6, no. 1, pp. 3–65, 2002.

[145] J.-S. Rhyee, K. H. Lee, S. M. Lee, E. Cho, S. I. Kim, E. Lee, Y. S. Kwon, J. H. Shim, and G. Kotliar, "Peierls distortion as a route to high thermoelectric performance in In(4)Se(3-delta) crystals.," Nature, vol. 459, no. 7249, pp. 965–968, 2009.

[146] H. Ohta, S. Kim, Y. Mune, T. Mizoguchi, K. Nomura, S. Ohta, T. Nomura, Y. Nakanishi, Y. Ikuhara, M. Hirano, et al., "Giant thermoelectric seebeck coefficient of a two-dimensional electron gas in srtio3," Nature materials, vol. 6, no. 2, pp. 129–134, 2007.

[147] A. I. Boukai, Y. Bunimovich, J. Tahir-Kheli, J.-K. Yu, W. a. Goddard, and J. R. Heath, "Silicon nanowires as efficient thermoelectric materials.," Nature, vol. 451, no. 7175, pp. 168–171, 2008.

[148] T. J. Seebeck, "Ueber die magnetische polarisation der metalle und erze durch temperaturdifferenz," Annalen der Physik, vol. 82, no. 3, pp. 253–286, 1826.

[149] B. Poudel, Q. Hao, Y. Ma, Y. Lan, A. Minnich, B. Yu, X. Yan, D. Wang, A. Muto, D. Vashaee, et al., "High-thermoelectric performance of nanostructured bismuth antimony telluride bulk alloys," Science, vol. 320, no. 5876, pp. 634–638, 2008.

[150] K. B. Koller and F. M. Hawkridge, "Temperature and electrolyte effects on the electron-transfer reactions of cytochrome c," Journal of the American Chemical Society, vol. 107, no. 25, pp. 7412–7417, 1985.

[151] P. F. Salazar, S. Kumar, and B. a. Cola, "Design and optimization of thermo-electrochemical cells," Journal of Applied Electrochemistry, vol. 44, no. 2, pp. 325–336, 2013.

[152] T. L. Bergman and F. P. Incropera, Introduction to heat transfer. John Wiley & Sons, 2011.

[153] D. B. Tuckerman and R. Pease, "High-performance heat sinking for vlsi," IEEE Electron device letters, vol. 2, no. 5, pp. 126–129, 1981.

[154] F. Zhou, E. M. Dede, and S. N. Joshi, "A novel design of hybrid slot jet and mini-channel cold plate for electronics cooling," in Thermal Measurement, Modeling & Management Symposium (SEMI-THERM), IEEE, 2015, pp. 60–67.

[155] M. V.D.V.J.D.K. S. Garimella William J. Dowling, "The effect of simultaneously developing flow on heat transfer in rectangular tubes," Heat Transfer Engineering, vol. 22, no. 6, pp. 12–25, 2001.

[156] E. N. Sieder and G. E. Tate, "Heat transfer and pressure drop of liquids in tubes," Industrial & Engineering Chemistry, vol. 28, no. 12, pp. 1429–1435, 1936.

[157] B. Weiss, H. L. Truong, W. Schott, T. Scherer, C. Lombriser, and P. Chevillat, "Wireless sensor network for continuously monitoring temperatures in data centers," IBM RZ, vol. 3807, 2011.

[158] J. Polastre, R. Szewczyk, and D. Culler, "Telos: Enabling ultra-low power wireless research,"

4th International Symposium on Information Processing in Sensor Networks (ISPN), vol. 2005, pp. 364–369, 2005.

[159] G. Berdichevsky, K. Kelty, J. Straubel, and E. Toomre, "The Tesla Roadster Battery System," Tesla Motors Inc, pp. 1–5, 2007.

[160] T. Kimura, S. Hamada, Y. Ogata, T. Yamauchi, and T. Sekimori, Battery pack, US Patent 6,569,561, 2003.

[161] M. F. De Volder, S. H. Tawfick, R. H. Baughman, and A. J. Hart, "Carbon nanotubes: Present and future commercial applications," Science, vol. 339, no. 6119, pp. 535–539, 2013.

[162] S. Iijima, "Helical microtubules of graphitic carbon," Nature, vol. 354, no. 6348, p. 56, 1991.